Institut für Geowissenschaften

Development of waveform-based, automatic analysis tools for the spatio-temporal characterization of massive earthquake clusters and swarms

Kumulative Dissertation zur Erlangung des akademischen Grades
"doctor rerum naturalium"
(Dr. rer. nat.)
in der Wissenschaftsdisziplin "Geophysik" der
Mathematisch-Naturwissenschaftlichen Fakultät

von
Marius Kriegerowski

Tag der Disputation: 19.12.2019

Betreut durch: apl. Prof. Dr. Frank Krüger und Dr. Simone Cesca
Gutachter: apl. Prof. Dr. Frank Krüger, Prof. Dr. Torsten Dahm und Prof. Dr. Daniel Stich

Published online at the
Institutional Repository of the University of Potsdam:
https://doi.org/10.25932/publishup-44404
https://nbn-resolving.org/urn:nbn:de:kobv:517-opus4-444040

Statement of Originality

I hereby declare that this thesis is the product of my own work. All the assistance received in preparing this thesis and the sources used have been acknowledged. The work contained in this thesis has not been previously submitted for a PhD degree at any other higher education institution.

Marius Kriegerowski
18 June 2019

Abstract

Earthquake swarms are characterized by large numbers of events occurring in a short period of time within a confined source volume and without significant main shock aftershock pattern as opposed to tectonic sequences. Intraplate swarms in the absence of active volcanism usually occur in continental rifts as for example in the Eger Rift zone in North West Bohemia, Czech Republic. A common hypothesis links event triggering to pressurized fluids. However, the exact causal chain is often poorly understood since the underlying geotectonic processes are slow compared to tectonic sequences. The high event rate during active periods challenges standard seismological routines as these are often designed for single events and therefore costly in terms of human resources when working with phase picks or computationally costly when exploiting full waveforms.

This methodological thesis develops new approaches to analyze earthquake swarm seismicity as well as the underlying seismogenic volume. It focuses on the region of North West (NW) Bohemia, a well studied, well monitored earthquake swarm region.

In this work I develop and test an innovative approach to detect and locate earthquakes using deep convolutional neural networks. This technology offers great potential as it allows to efficiently process large amounts of data which becomes increasingly important given that seismological data storage grows at increasing pace. The proposed deep neural network trained on NW Bohemian earthquake swarm records is able to locate 1000 events in less than 1 second using full waveforms while approaching precision of double difference relocated catalogs. A further technological novelty is that the trained filters of the deep neural network's first layer can be repurposed to function as a pattern matching event detector without additional training on noise datasets.

For further methodological development and benchmarking, I present a new toolbox to generate realistic earthquake cluster catalogs as well as synthetic full waveforms of those clusters in an automated fashion. The input is parameterized using constraints on source volume geometry, nucleation and frequency-magnitude relations. It harnesses recorded noise to produce highly realistic synthetic data for benchmarking and development. This tool is used to study and assess detection performance in terms of magnitude of completeness M_c of a full waveform detector applied to synthetic data of a hydrofracturing experiment at the Wysin site, Poland.

Finally, I present and demonstrate a novel approach to overcome the masking effects of wave propagation between earthquake and stations and to deter-

mine source volume attenuation directly in the source volume where clustered earthquakes occur. The new event couple spectral ratio approach exploits high frequency spectral slopes of two events sharing the greater part of their rays. Synthetic tests based on the toolbox mentioned before show that this method is able to infer seismic wave attenuation within the source volume at high spatial resolution. Furthermore, it is independent from the distance towards a station as well as the complexity of the attenuation and velocity structure outside of the source volume of swarms. The application to recordings of the NW Bohemian earthquake swarm shows increased P phase attenuation within the source volume ($Q_P < 100$) based on results at a station located close to the village Luby (LBC). The recordings of a station located in epicentral proximity, close to Nový Kostel (NKC), show a relatively high complexity indicating that waves arriving at that station experience more scattering than signals recorded at other stations. The high level of complexity destabilizes the inversion. Therefore, the Q estimate at NKC is not reliable and an independent proof of the high attenuation finding given the geometrical and frequency constraints is still to be done. However, a high attenuation in the source volume of NW Bohemian swarms has been postulated before in relation to an expected, highly damaged zone bearing CO_2 at high pressure.

The methods developed in the course of this thesis yield the potential to improve our understanding regarding the role of fluids and gases in intraplate event clustering.

Zusammenfassung

Erdbebenschwärme zeichnen sich durch eine große Anzahl an Ereignissen in einem relativ kleinen Zeitraum und Volumen aus. Im Gegensatz zu tektonischen Sequenzen ist in der Regel keine signifikantes Muster von Vor- und Nachbeben erkennbar. In Abwesenheit aktiven Vulkanismusses, kommen Erdbebenschwärme innerhalb kontinentaler Platten häufig an kontinentalen Verwerfungen vor, wie Beispielsweise im Bereich des Egergrabens im nordböhmischen Becken (Tschechien). Eine übliche Hypothese verbindet den Erdbebenentstehungsprozess mit Hochdruckfluiden. Der exakte kausale Zusammenhang ist jedoch häufig enigmatisch, da die zugrundeliegenden geotektonischen Prozesse im Vergleich zu tektonischen Sequenzen relativ langsam sind. Die hohe Erdbebenrate während aktiver Phasen stellt hohe Anforderungen an etablierte seismologische Routinen da diese häufig für Einzelereignisse konzipiert sind. So können sie einen hohen Aufwand bei manueller Selektion seismischer Phasen (*picking*) bedeuten oder rechenerisch aufwändig sein wenn volle Wellenformen verarbeitet werden sollen.
Im Rahmen dieser methodologischen Thesis werden neue Ansätze zur Analyse seismischer Schwärme, sowie des zugrundeliegenden seismogenen Volumens entwickelt. Der Fokus liegt hierbei auf der gut untersuchten und überwachten nordböhmischen Schwarmregion.
Ich entwickle und teste in dieser Arbeit einen innovativen Ansatz zur Detektion und Lokalisation von Erdbeben basierend auf einem tiefen konvolvierenden neuronalen Netzwerk. Diese Technologie bietet großes Potential da sie es erlaubt große Datenmengen effizient zu verarbeiten was durch die zunehmenden Datenmengen seismologischer Datenzentren immer weiter an Bedeutung gewinnt. Das entwickelte tiefe neuronale Netzwerk, trainiert auf Aufnahmen nordböhmischer Erdbebenschwärme, ist in der Lage 1000 Eregnisse in weniger als 1 Sekunde bei Verwendung voller Wellenformen zu lokalisieren und erreicht eine Präzision die vergleichbar ist mit der Genauigkeit eines Katalogs, der mittels Doppelte Differenzen Methode relokalisiert wurde. Eine weitere technologische Neuheit ist, dass die trainierten Filter der ersten Schicht des tiefen neuronalen Netzwerkes als Mustererkennungsfilter umfunktioniert werden und damit als Ereignisdetektor dienen können, ohne, dass zuvor explizit auf Rauschdaten trainiert werden muss.
Für die weitere technologische Entwicklung stelle ich ein neues, automatisiertes Werkzeug für die synthetisierung realistischer Erdbebenschwarmkataloge, sowie hierauf basierender synthetischer voller Wollenform vor. Die Eingabeparameter

werden durch die Geometrie des Quellvolumens, der Nukleationscharakteristik und Magnitude-Häufigkeitsverteilung definiert. Weiter können Rauschsignale realer Daten verwendet werden um äußerst realistische synthetische Daten zu generieren. Dieses Werkzeug wird verwendet um die Vollständigkeitmagnitude eines Detektors für volle Wellenformen anhand synthetischer Daten zu evaluieren. Die synthetisierten Daten sind Motiviert durch ein Hydrofrackingexperiment in Wysin (Polen).
Des Weiteren stelle ich einen neuen Ansatz vor, der die Effekte der Wellenausbreitung zwischen Erdbeben und Stationen ausblendet und die Bestimmung der Dämpfung unmittelbar im Quellvolumen von Schwarmerdbeben erlaubt. Diese neue Methode benutzt das hochfrequente spektrale Verhältnis von Ereignispaaren mit gemeinsamen Strahlenwegen. Synthetische Tests zeigen, dass die Methode in der Lage ist die Dämpfung innerhalb des Quellvolumens mit hoher räumlicher Genauigkeit zu bestimmen. Weiter ist sie im Einzelnen unabhängig von der Entfernung zwischen Ereignis und Station als auch von der Komplexität der Dämpfungs- und Geschwindigkeitsstruktur außerhalb des Quellvolumens. Die Anwendung auf Daten des nordböhmischen Erdbebenschwarms zeigt eine erhöhte P Phasen Dämpfung im Quellvolumen ($Q_p < 100$) basierend auf Daten einer Station in der Nähe des Dorfes Luby (LBC). Die Wellenformen einer Station in unmittelbarer epizentraler Nähe, bei Nový Kostel (NKC), weisen eine relativ hohe Komplexität auf, was darauf hindeutet, dass seismische Wellen, die diese Station erreichen relativ stark gestreut werden im Vergleich zu anderen Stationen. Das hohe Maß an Komplexität destabilisiert die Methode und führt zu ungenauen Schätzungen an der Station NKC. Daher bedarf es einer weiteren unabhängigen Validierung der hohen Dämpfung bei gegebenen geometrischen und spektralen Voraussetzungen. Nichtsdestoweniger wurde bereits eine hohe Dämpfung im Quellvolumen der nordböhmischen Schwärme postuliert und erwartet, insbesondere im Zusammenhang mit einer Zone hoher Brüchigkeit die CO_2 bei hohen Drücken beinhaltet.
Die Methoden die im Rahmen dieser Thesis entwickelt werden haben das Potential unser Verständnis bezüglich der Rolle von Fluiden und Gasen bei Erdbebenschärmen innerhalb kontinentaler Platten zu verbessern.

Contents

List of Figures

Chapter 1

Introduction

The term earthquake swarm describes a phenomenon of large numbers of earthquakes occurring in confined source regions usually within a finite period of time which may last from days to several months often without a distinct significant main shock (Jakoubková et al., 2018). For example, approximately 25000 events with magnitudes between -0.5 and 3.5 were registered within four weeks during the earthquake swarm which occurred in October 2008 in North West (NW) Bohemia (Vavryčuk et al., 2013). The high event density allows to develop and apply dedicated techniques to improve results in several disciplines from earthquake detection, localization to attenuation analysis. These three aspects constitute the focus of the following sections. On the downside increasing amounts of data and high event density challenge established processing routines and/or operators that work in a manual fashion and underline a demand for higher levels of automation and more efficient routines.
Regions, where swarms occur repeatedly over decades are often well monitored as is the case in NW Bohemia (Hiemer et al., 2012) which will therefore serve as a case study data set. Also, the study area in NW Bohemia is of high scientific interest, as the origin of the regular, midcrustal earthquake swarms is still enigmatic.

1.1 Earthquake swarm analysis

Earthquake detection and localization is a common first step of earthquake swarm analysis and seismology in general. In the early days earthquake detection was manually carried out by observatories' operators. Localizations of detected earthquakes were calculated based on manually picked arrival times of compressional (P), shear (S) and other phases. The most widely used method dates back to a work by Geiger (1910) who developed an iterative least squares minimization of the residuals between observed and calculated theoretical travel times of seismic phases. However, the quality of picks of body wave first arrivals (phases) and consequently the quality of location is dependent on the level of experience of the operator (Velasco and Zeiler, 2009) and the approach can be considered highly

time consuming and labor intensive. The latter renders this technique impractical for earthquake swarms. A simple yet powerful alternative to measure phase arrivals and to detect earthquakes on full waveforms is to calculate the short term average (STA) and normalize it by the long term average (LTA) of the energy of a seismic trace. This provides a robust method to detect relative changes in energy as caused by seismic waves passing the receiver but is prone to produce false detections, especially in noisy conditions (Sharma et al., 2010).
There are dedicated techniques for event detection and location that are specifically designed for event clusters and can harness the high event density to achieve significantly higher accuracies than e.g. standard STA/LTA detectors or absolute location methods (Slunga et al., 1995). Some of these methods exploit the fact that event clusters are often characterized by high waveform similarity. A more sophisticated alternative to STA/LTA ratios for the detection of clustered events is to use pattern matching. Waveforms of characteristic events serve as stencils and are compared against full waveforms by cross correlation. This technique allows to efficiently detect smallest events that are mostly hidden in noise (Gibbons and Ringdal, 2006). However, this method requires templates as reference events which may not be known *a priori*. In this case auto-correlation constitutes an alternative but is computationally demanding. More recent approaches overcome this weakness by compressing or encoding signals as "fingerprints". Similar signals producing similar fingerprints can than be analyzed using standard clustering algorithms (Yoon et al., 2015). The high waveform similarity found in event clusters also allows to precisely calculate relative travel times of seismic phases by waveform cross-correlation or cross-spectral analysis of event pairs (Ito, 1985). Precise phase onset differences can then be used to locate clustered earthquakes relative to a master event (Ito, 1985) or by solving a system of linear equations that relate all event pairs' differential travel times (Got et al., 1994). The double difference relocation algorithm implemented by Waldhauser and Ellsworth (2000), *HypoDD*, iteratively minimizes residuals of theoretical and observed travel times of event pairs. This approach, as well as master-event relocation methods are routinely applied to relocate earthquake clusters in NW Bohemia (e.g. Vavryčuk et al., 2013; Fischer et al., 2010).
With increasing computational capacities full waveform migration methods for localization gained popularity, such as wavefield backpropagation using time-reversed seismograms - a computationally demanding technique(McMechan, 1982; Gajewski and Tessmer, 2005). A different approach is based on delay and sum of characteristic functions deduced from full waveforms. These techniques allow to detect and locate events even if their signals interfere. Furthermore, they do not require picking phases and these methods can be applied fully automated (Grigoli et al., 2018; Cesca and Grigoli, 2015). Therefore, the cost in terms of human resources is usually lower compared to pick based methods. The downside is the significant computational cost (Grigoli et al., 2016) which render these techniques almost prohibitive for large event catalogs such as in NW Bohemia even when using vast parallelization across multiple central processing units (CPU).
The recent surge of deep learning has outperformed established methods in many

scientific fields (Minar and Naher, 2018). These methods are still in its' infancy in the field of seismology but first feasibility studies show promising results. A general advantage is the high efficiency owed to the efficient implementation and computation on graphical processing units (GPU). Convolutional neural networks (CNN) are well suited for waveform analysis and phase picking implementations have produced results of very high precision (Zhu and Beroza, 2018). In Chapter 2 I present and evaluate a deep CNN trained on earthquake swarm data. The approach is partly comparable to the work of Zhang et al. (2018) but predicts locations using deep regression (Lathuilière et al., 2018) in the top layer instead of sampling the source volume in discrete voxels and assigning each voxel a hypocenter probability.

The development and benchmarking of such new methodologies dedicated to earthquake cluster analysis requires realistic synthetic catalogs as well as full waveform datasets that resemble characteristics of the true earthquake swarm data under investigation. Different tools have been designed to generate event cluster catalogs (e.g Console et al., 2015; Davis and Frohlich, 2007; Daub et al., 2015) as well as realistic full waveforms which can be modelled for 1D models with good accuracy and performance (Wang, 1999; Nissen-Meyer et al., 2014) based on these catalogs in a second step. To facilitate the procedure and to generate bulk swarm data I designed a new toolbox that combines both processing steps. It allows to generate realistic earthquake cluster catalogs and synthetic realistic full waveforms affected by real noise. This tool is presented in Chapter 3 where it provides the basis for synthetic tests and detection performance analysis.

Besides event detection and localization, dedicated cluster techniques can be beneficial also to estimate physical properties, such as attenuation. Shear and compressional wave attenuation, often parameterized as the dimensionless quality factor Q, constitute a crucial parameters that allow to assess rock properties such as porosity, gas or fluid content of the source volume. These properties map into the velocity of shear and compressional waves (v_p, v_s) but also into the attenuation of both wave types (Q_p, Q_s).
The source array technique (Spudich and Bostwick, 1987) exploits highly correlated waveforms. It allows to apply receiver array methods to groups of correlated events (source arrays) based on the Green's function reciprocity (Aki and Richards, 2002). This approach can then be used to locate earthquakes and also to study e.g. the coda attenuation Q_c (Scherbaum et al., 1997). Regional attenuation tomography is often carried out using the amplitude spectral ratio method applied to station couples (Aki, 1980). Gaebler et al. (2015) applied this method to NW Bohemia. Regional attenuation tomography can benefit from event clusters when inverting the ray path attenuation for sub-cluster as this reduces the number of degrees of freedom in the inversion (Ko et al., 2012). Wcisło et al. (2018) applied the peak frequency method (Eisner et al., 2013) to NW Bohemia and exploited the high event density using a relative attenuation inversion ap-

proach. Another method that exploits event clusters is proposed in the work of Matsumoto et al. (2009) and uses spectral ratios of direct phases normalized by their coda.
In Chapter 4 I develop and demonstrate a modified amplitude spectral ratio method for event clusters that uses the high frequency slope of event pairs. I further test its applicability to event couples of the NW Bohemian dataset. The developed method is motivated by double difference relocation approaches which benefit from high event densities. The selection of data windows is based on hand picked phase catalogs. Therefore, it can be considered semi-automated as it does not require manual measurement e.g. of onset pulse widths to deduce the attenuation. However, the high efficiency of deep learning based algorithms for detection and location of clustered earthquakes, presented in Chapter 2, constitutes a potential replacement for the highly labor intensive hand picking and locating procedure. This can also be a way to exploit data for attenuation in a more exhaustive fashion.
The tool to generate realistic synthetic catalogs and waveforms (Chapter 3) constitutes a feasible way to benchmark and assess the source volume attenuation method. It provides controllable data sets that enable development under realistic conditions.

1.2 Event clusters in NW Bohemia

NW Bohemia located in the Cheb Basin (Czech Republic) is a region of repeated intra-continental mid-crustal earthquake swarm activity. Significant scientific effort focused on NW Bohemia lead to the general understanding that the geodynamic activity of the entire region forms the origin of the intraplate seismicity. During active periods up to several hundreds of events are registered each day located in confined source regions as the double difference (Waldhauser and Ellsworth, 2000) relocated event catalog shows (Fischer et al., 2010). The events cluster in depths between 6 and 12 km depth on a North-South striking, sub-vertically dipping fault plane (Fischer et al., 2014). The origin of seismicity in this region remains under debate. It is accompanied by CO_2 degassing in different locations in this area (Bräuer et al., 2004, 2009, 2011). Studies on $^3He/^4He$ ratios in free gases indicate magmatic activity pointing towards uprising magmatic fluid injections from the lithospheric mantle (Bräuer et al., 2009). Three-dimensional velocity tomography results show an increased V_p / V_s ratio in the source region beneath a region of low values which can be explained by changes in fluid concentrations (Alexandrakis et al., 2014). Dahm and Fischer (2013) explained temporal changes in V_p / V_s ratios during seismically active phases by overpressurized gas which enriches the source volume during seismically active periods.
Besides the already mentioned ones, the entire region has been the focus of further numerous scientific studies from different disciplines (Fischer et al., 2014) such as hypocenter and focal mechanisms analysis (Vavryčuk et al., 2013) and

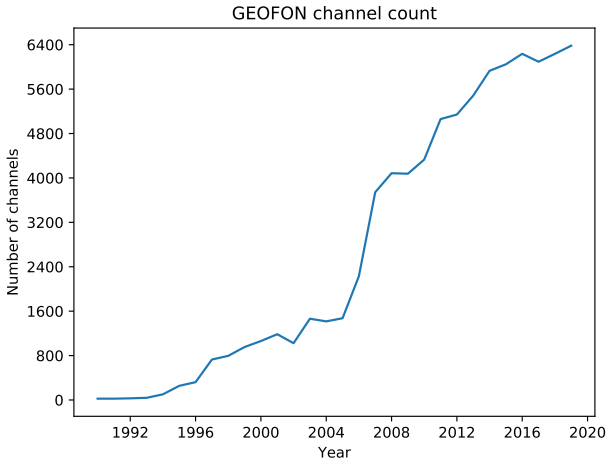

Figure 1.1: Number of channels publicly available from the *GEOFON* database between 1990 and 2019.

attenuation tomography (e.g. Wcisło et al., 2018). Therefore, many aspects of this region have already been illuminated which makes this a favorable natural laboratory for methodological development (Fischer et al., 2014).
I was provided with full waveform records of the West Bohemian seismological network *WEBNET* operated by the Institute of Geophysics of the Czech Academy of Sciences *IG CAS*. This dataset constitutes the basis for Chapters 2 and 4. The *WEBNET* consists of 23 stations most of which are streaming data in real time today. However, during the recording period of the provided data in 2008 most of the stations opperated in triggering mode. The data is therefore incomplete. In addition to waveforms I received catalogs of hand picked onsets and double difference relocated event hypocenters which I used to develop the methodologies outlined in this thesis.
The large number of events requires sophisticated methodologies to analyze large amounts of data: Hand picked phase catalogs of the 2008 NW Bohemia earthquake swarm are comprised of 14500 onsets registered between October 6 and October 13, only. Full waveform records of the local network for the same period reach a total volume of approximately 400 MB per day. New installations are planned by the international continental scientific drilling project *ICDP* with increased sampling rates. The current large and projected increasing full waveform database are exemplary for challenges that modern digital seismology faces. Figure 1.1 shows the publicly available number of channels in the *GEOFON* database between 1990 and 2019. A constant increase becomes evident lasting throughout the entire displayed period. It can be speculated that this trend will persist in the future. This is a great tendency for the seismological community as it will foster increasingly holistic seismological research. The downside of this trend is increasing demands regarding data warehousing and data processing. These aspects demand semi- or fully automated technologies that allow efficient analysis and processing to enable a full exploitation of seismological data avail-

able today and in the future.

This thesis describes new methodologies to efficiently process seismological records of earthquake clusters. The presented techniques are designed, developed and tested with full waveform records of seismic clusters.

The key questions of this thesis are: How can the task of event detection and localization be automated and improved so that performance scales with growing databases of full waveforms, not only found in earthquake swarms but in a global perspective? Is it possible to increase the spatio-temporal resolution of seismic attenuation imaging of the earthquake cluster source region using a semi-automated attenuation inversion approach based on event couple spectral ratios? What can we infer from the results regarding triggering mechanisms such as gases and/or fluids of the swarm events?

1.3 Publications Relevant to this Thesis

Publication 1 (Chapter 2): Kriegerowski, M., Petersen, G. M., Vasyura-Bathke, H., and Ohrnberger, M. (2018). A Deep Convolutional Neural Network for Localization of Clustered Earthquakes Based on Multistation Full Waveforms. *Seismological Research Letters*, 90(2A):510–516.

The first publication of this thesis presents a novel approach for deep learning based event detection and location on full waveforms. The major strength of this technique is its efficiency and high precision. It approaches the accuracy of the reference double difference relocated event catalog. It can be considered a future drop-in replacement for event relocalizations that require labor intensive hand picking of arrivals. Hence, it constitutes a key aspect and the basis for scalable efficient mapping of rock properties described in Chapter 4.

Publication 2 (Chapter 3): López-Comino J. A., Cesca S., **Kriegerowski, M.**, Heimann, S., Dahm, T., Mirek, J. and Lasocki, S. (2017). Monitoring performance using synthetic data for induced microseismicity by hydrofracking at the Wysin site (Poland). *Geophysical Journal International*, 2017, 210: 42-55.

I developed a toolbox named *swarming* that allows easy and fast generation of large earthquake cluster catalogs and waveforms (codes are available at `https://github.com/HerrMuellerluedenscheid/swarming`). *swarming* is used in the work presented in the second publication of this thesis. It is designed to generate realistic earthquake swarm catalogs and waveforms for a defined region and given station setup. The parameterized source volume or plane is filled with random hypocenter locations. A systematic rupture onset distribution can be applied to all sources to mimic migration of sources. Focal mechanisms can be derived from a reference mechanism with varying levels of randomization. Figure 1.2, top panel, shows a simulated rectangular fault filled with 1000 uniformly distributed events. Relative nucleation time is indicated by color, starting in the

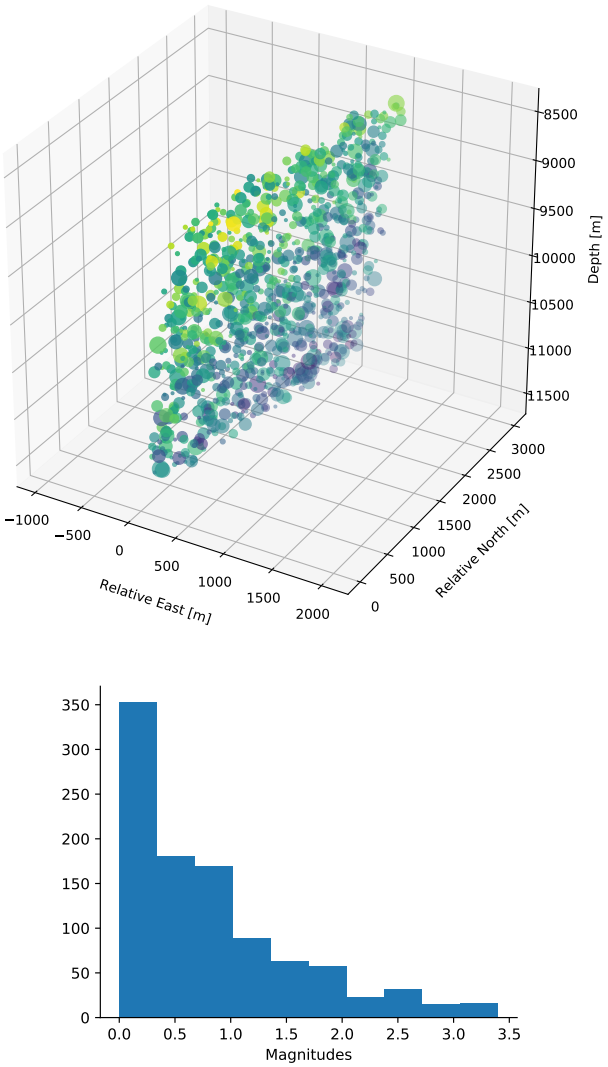

Figure 1.2: Top: Synthetic sources generated using the tool *swarming*. Sources are aligned along a sub-vertical slab as seen from South-West in a depth between 8.5 and 11.5 km. Colors and sizes represent nucleation time and magnitude, respectively. Bottom: Magnitudes follow a Gutenberg-Richter distribution. The geometry and magnitude distribution resemble those of the 2008 earthquake swarm in NW Bohemia as used in Chapters 2 and 4.

deeper northern corner (blue) and migrating to the shallower southern corner (yellow) of the fault. Moment magnitudes are drawn from a Gutenberg-Richter distribution defined by a b-value and minimum magnitude (Figure 1.2, bottom panel). Magnitudes are converted to realistic source durations during the waveform generation process.
After generating a realistic event catalog, synthetic waveforms are automatically synthesized using `pyrocko.gf` (see Section 1.4) (Heimann et al., 2019). The resulting traces are first convolved with half-sine shaped source time functions with the deduced rupture duration and thereafter with the transfer function of the actual recording stations to simulate the spectral characteristics of the underlying recording device. In a post processing step, traces are merged with randomly extracted records of real noise which are drawn from a noise database. The toolbox developed in the scope of this work provides the basis for realistic synthetic tests presented in the third publication (Chapter 4).

Publication 3 (Chapter 4): Kriegerowski, M., Cesca, S., Ohrnberger, M., Dahm, T., and Krüger, F. (2019). Event couple spectral ratio Q method for earthquake clusters: application to northwest Bohemia. *Solid Earth*, 10(1):317–328.

In the third publication, a new technique to deduce source volume attenuation is presented. For synthetic testing it employs the tools presented in Publication 2 (Chapter 3). While the used event locations were the provided pick based double difference relocated events, the technique described in the first publication (Chapter 2) will allow a significantly faster assessment in the future as it will replace labor intensive hand picking and manual localization.

1.4 Further relevant contributions

Sebastian Heimann, **Marius Kriegerowski**, Marius Isken, Simone Cesca, Simon Daout, Francesco Grigoli, Carina Juretzek, Tobias Megies, Nima Nooshiri, Andreas Steinberg, Henriette Sudhaus, Hannes Vasyura-Bathke, Timothy Willey, and Torsten Dahm. (2017) Pyrocko - An open-source seismology toolbox and library. *GFZ Data Services*. http://doi.org/10.5880/GFZ.2.1.2017.001

Sebastian Heimann, Hannes Vasyura-Bathke, Henriette Sudhaus, Marius Paul Isken, **Marius Kriegerowski**, Andreas Steinberg, and Torsten Dahm. A Python framework for efficient use of pre-computed Green's functions in seismological and other physical forward and inverse source problems. Solid Earth Discussions, pages 1–22, may 2019

A significant share of my work that is directly related to this thesis was dedicated to the co-development of the seismological toolbox *pyrocko* (Heimann et al., 2017). In this context I also contributed to the development of the `pyrocko.gf` module (`gf` stands for Green's function) as well as parts of the

forward modelling and storage tool *fomosto* (Heimann et al., 2019). The latter wraps numerical forward modelling codes and stores raw Green's functions in databases. Precalculated Green's functions then allow rapid generation of synthetic full waveform records (For the core concept the interested reader may consult the work of Heimann (2011)). Both, `pyrocko.gf` as well as *fomosto* have been used in the presented work. My exact contributions can be reviewed on the pyrocko project page on github: `https://github.com/pyrocko/pyrocko/graphs/contributors` (pseudonym: *HerrMuellerluedenscheid*).

Chapter 2

A deep convolutional neural network for localization of clustered earthquakes based on multi-station full waveforms

Authors:
Marius Kriegerowski (1) (kriegero@uni-potsdam.de), Gesa M. Petersen (1,2), Hannes Vasyura-Bathke (1), Matthias Ohrnberger (1)

Journal:
Seismological Research Letters; 90 (2A): 510–516.
doi: https://doi.org/10.1785/0220180320

Status: Published

Affiliations:
(1) University of Potsdam, Germany
(2) Helmholtz Centre Potsdam GFZ German Research Centre for Geosciences, Germany

2.1 Abstract

Earthquake localization is both a necessity within the field of seismology, and a prerequisite for further analysis like source studies and hazard assessment. Traditional localization methods often rely on manually picked phases. We present an alternative approach using deep learning, that, once trained can predict hypocenter locations efficiently. In seismology, neural networks have typically been trained with either single station records or based on features, that have been extracted previously from the waveforms. We use three-component full waveform records of multiple stations directly, this means no information is lost during preprocessing and preparation of the data does not require expert knowledge. The first convolutional layer of our deep convolutional neural network (CNN) becomes sensitive to features that characterize the waveforms it is trained on. We show that this layer can therefore additionally be used as an event detector.

As a test case, we trained our CNN using more than 2000 earthquake swarm events from West Bohemia, recorded by nine local three-component stations. The CNN successfully located 908 validation events with standard deviations of 56.4 m in East-West-, 123.8 m in North-South- and 136.3 m in vertical direction compared to a double difference relocated reference catalog. The detector is sensitive to events with magnitudes down to $Ml = -0.8$ with 3.5% false positive detections.

2.2 Introduction

Earthquake localization routines typically use onset times of seismic phases recorded at different stations and minimize a loss function with respect to synthetic arrivals (Havskov et al. (2012)). This method is computationally efficient but requires phase onsets picked or manually revised by (preferably) experienced seismological analysts. In contrast, attempts to exploit full waveforms for localization achieve good accuracy and require little manual preprocessing, but are computationally expensive (e.g. Grigoli et al. (2013)) and, therefore, intractable when working with large amounts of data. Nevertheless, robust automated processing techniques become increasingly important for analysis of the rapidly growing global seismological datasets.
Neural networks can help to handle largest amounts of data and provide ways to rapidly detect, localize and interpret seismic events with little human interaction. In this study we present a convolutional neural network (CNN) as a flexible tool for earthquake localization and demonstrate its application to full-waveform data of clustered events of an earthquake swarm occurring in 2008 in Western Bohemia, Czech Republic. Through this approach we avoid phase picking and teach a CNN to obtain localizations based on gathers of seismic traces.

Deep convolutional neural networks are artificial neural networks, which comprise one or several convolutional layer(s). Each convolutional layer is comprised

of a number of filter kernels that are generally much smaller than the input layer. Such kernels are moved across the layer's input, at each stride the cross-correlation value is computed representing the activation of the neurons of the convolutional layer. The different filter kernels of each layer are initialized randomly. During the training loop these filters are updated repeatedly through backpropagation to minimize a loss function for the given task (e.g. LeCun et al. (2015), Goodfellow et al. (2016)).

Compared to other scientific fields like image-, video-, text- and speech-processing, the application of deep neural networks to seismological questions is still in its infancy. In most case studies published to date, moderately complex yet powerful network architectures have been used.

First attempts to use multilayer perceptrons (MLP) with one hidden layer for event detections and phase picking date back to the 1990's (Wang and Teng (1995), Wang and Teng (1997), Tiira (1999), Zhao and Takano (1999)).

A study of Musil and Plešinger (1996) exploited MLP to discriminate micro-earthquakes and quarry or mining blasts in the Western Bohemia earthquake region based on 7 amplitude and 7 spectral features, which have been previously extracted from broadband waveform records.

In 2003, Del Pezzo et al. published a study on discrimination of earthquakes and underwater explosions, again using a 3-layer MLP based on 7 parameters that were extracted from waveforms in a preprocessing step. Böse et al. (2008) extracted differential P-phase arrival times and cumulative absolute velocities of simulated data for a number of sensors in an array. From these they estimated hypocentral location, magnitude and rupture direction of finite fault earthquakes for early warning by using three fully-connected feed-forward neural networks with one hidden layer.

Köhler et al. (2010) used unsupervised pattern recognition for the discovery, imaging and interpretation of temporal patterns in seismic array recordings. Before training, the raw data was parameterized in feature vectors. Self-organizing maps were used for feature selection, visualization and clustering. Recently, Zhu and Beroza (2018) introduced the *PhaseNet*, a U-shaped deep convolutional neural network for arrival time picking of P- and S- phases. *PhaseNet* uses three component data and yields probability distributions of P- and S-phase onsets over time. The network was trained on over 7 million manually labeled seismic records.

Ross et al. (2018a) used a CNN with three convolutional layers for P-wave arrival picking and first-motion polarity discrimination and Ross et al. (2018b) showed that a convolutional neural network trained on a large dataset is very sensitive in detecting seismic phases, even under high-noise conditions.

Likewise in 2018, Perol et al. introduced the *ConvQuakeNet*, a CNN for earthquake detection and localization based on single waveforms, performing comparatively well and very efficient compared to established methods on event detection. Rough localizations were achieved by classifying events as belonging to one of 6 regions.

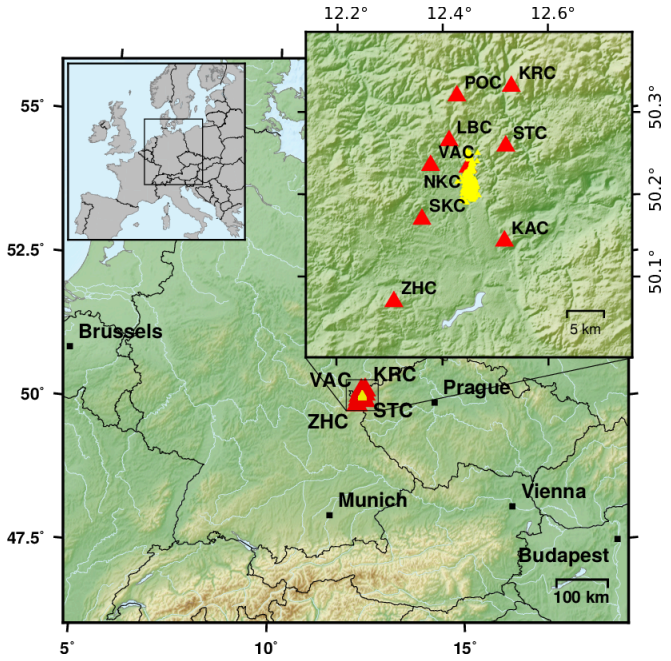

Figure 2.1: Location of the seismic stations and West Bohemia earthquake swarm region. Left inset: Europe, the black rectangle marks the extent of the main map; Right inset: Location of the used seismic stations (triangles) and the relocated events (dots) of the 2008 earthquake swarm.

In our study, we use multiple three component seismic traces simultaneously, to obtain hypocenter locations of earthquake clusters occurring in a confined source region. We employ a deep convolutional neural network for regression analysis based on full waveform multichannel seismic recordings targeting precise event localizations.

The West Bohemia Earthquake Swarm Region

Western Bohemia, located at the border region between the Czech Republic and Germany (Fig. 2.1), is tectonically active with Holocene volcanism, present day gas and fluid emissions as well as reoccurring earthquake swarms (Fischer et al. (2014)). Large earthquake swarms, each with several hundreds to thousands of events were recorded close to the city of Nový Kostel for example in 1985/1986, 1997, 2000, 2008/2009 and 2011 (Fischer et al. (2014)). Magnitudes of the events usually do not exceed ML 4 and focal depths reach from about 6 to 14 km. For this study, we use waveforms of more than 3000 events of the 2008 earthquake swarm recorded by nine WEBNET stations (Institute of Geophysics, Academy of Sciences of the Czech Republic (1991)) (Fig. 2.1). Locations and origin times were taken from a double difference relocated event catalog (Fischer et al. (2010)). The sources align along a north-south striking fault plane with a horizontal and vertical extent of approximately 3000 and 2000 meters.

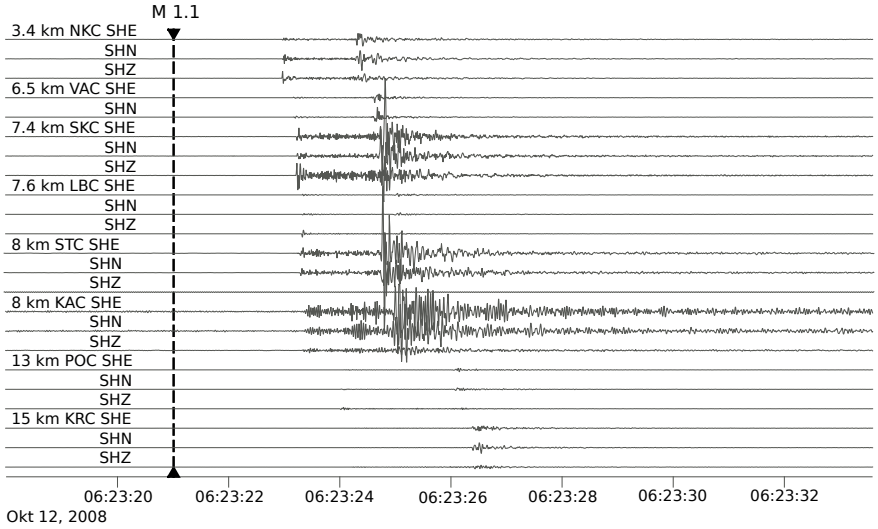

Figure 2.2: Example waveforms of a Ml 1.1 event on October 12, 2008, recorded on 8 stations (bandpass filter 0.8 - 50 Hz).

2.3 Methodology: A deep CNN for earthquake localization

We employ a convolutional neural network trained on event locations (labels) and full waveform records (features) of the WEBNET stations. The input is provided as 2 dimensional arrays with size defined by the number of traces and number of samples within the chosen time window. The order of traces is maintained across examples.

Data preparation and preprocessing

We use a total of 2118 events for training and 908 events for validation (70 % split rate). The training and the validation datasets are prepared in the same way.

Event information (origin time and hypocentral location) are taken from a double-difference relocated event catalog (Fischer et al. (2010)) of the earthquake swarm in Nový Kostel in 2008. An event example is shown in Figure 2.2. The catalog locations are first transformed to Cartesian coordinates (east, north, depth) relative to station *NKC*. Afterwards, we normalize labels by subtracting the median from each domain and divide through the mean of standard deviations of all three domains. While label normalization is not strictly required in each situation, in our case it has proven to reduce the number of exploding losses throughout training. We assume that this is related to exploding gradients when working within the original domain (meters) (e.g. Bengio et al. (1994), Pascanu et al. (2012)).
Time windows of 6.2 seconds lengths are cut starting 0.2 seconds before the P-phase onset at station *NKC*.

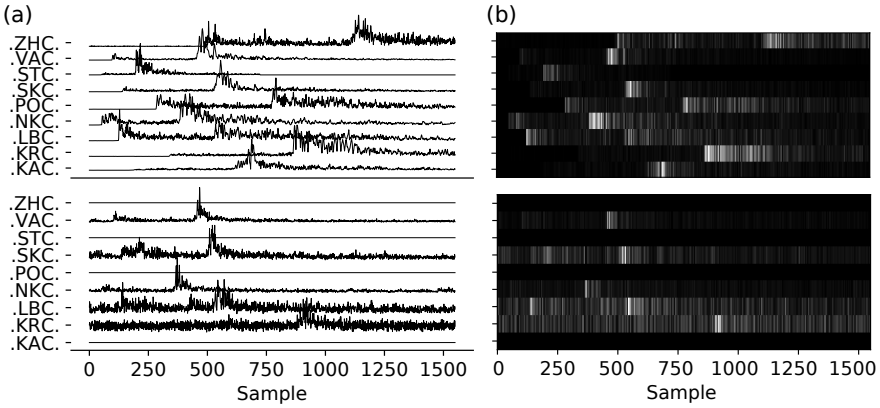

Figure 2.3: Preprocessing: (a) Two stacked, normalized and highpass filtered feature examples. (b) Greyscale image of normalized amplitudes as shown in (a).

We highpass filter all data at 0.8 Hz, which removes the static DC offset. We stack absolute amplitudes of the three components of each station and normalize each waveform stack by division through the maximum (Fig. 2.3, (a)). This actually increases relative noise levels for lower magnitude events. However, we expect the network's filters to be insensitive to uncorrelated noise. We also experimented with normalization using the maximum amplitude of each example, division through each example's standard deviation, as well as logarithmic normalization of absolute amplitudes. The latter has the advantage, that some degree of relative amplitudes, and therefore information on relative magnitudes, is preserved. However, normalization by channel maximum amplitude turned out to outperform the other attempts. Gaps in the data were filled with zeros. Examples were shuffled in each iteration during training.

Each data patch consists of the stacked channels of each station. The stations can be in any order as long as the order is maintained at all times. We used an alphabetic order (Fig. 2.3, (a)). The data of each event spans a 2D regular raster, in which the rows correspond to the stacked traces of each station and the columns to the time samples. The amplitude value of each sample is the pixel's greyscale value (Fig. 2.3, (b)).

Network architecture

The implemented convolutional neural network used in this study employs the *tensorflow* machine learning framework (see Sec. Data and Resources). The entire code for this project is available on github (`https://github.com/HerrMuellerluedenscheid/pinky.git`). It is a command line tool that can easily be adapted to other training data.

The network architecture used here is comprised of three convolutional layers with varying kernel sizes, followed by a fully-connected dense layer with 512 neurons and an output layer providing the 3 outputs, depth, East- and North-shift (Fig. 2.4). The three convolutional layers have 32, 64 and 128 filters with ker-

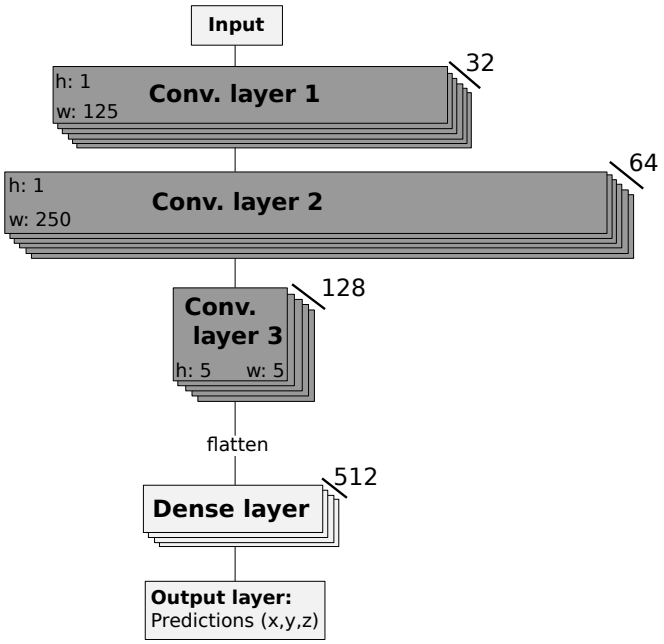

Figure 2.4: Schematic architecture of the convolutional neural network used for earthquake localization. h and w are the height and width of the filter kernels and the number at the top right of each layer indicates the number of kernels in that layer.

nel dimensions of width=125/height=1, 250/1 and 5/5. The motivation behind the first two convolutional layers comprised of one dimensional filters is the assumption that these learn temporal patterns. The third convolutional layer is comprised of two dimensional filters. These filters are designed such that they gather cross-station information.

We used a batch size of 32 as this turned out to be a compromise between efficiency and generalization. Larger batch sizes showed poorer generalization performance (cf. Keskar et al. (2016)). We apply batch normalization to each CNN layer output. We did not find a significant improvement when using max pooling over convolution with strides, and therefore, decided for the final architecture to use the latter (cf. also Springenberg et al. (2014)).

Dropout is applied in all layers, which reduces the risk of overfitting and ensures a better generalization (e.g. Srivastava et al. (2014)). For the presented dataset we found that a dropout rate of 37 % produced lowest errors (Figure 2.5 (b)). We use the *ADAM* optimizer with a learning rate of 0.0003 (Kingma and Ba (2014)). Training takes approximately 1 hour on a *Nvidia GeForce GTX 1080Ti* for 600 epochs with batch sizes of 32 examples. We randomly removed stations with a rate of 5% in each example as this improves generalization. We refer to this approach as station dropout.

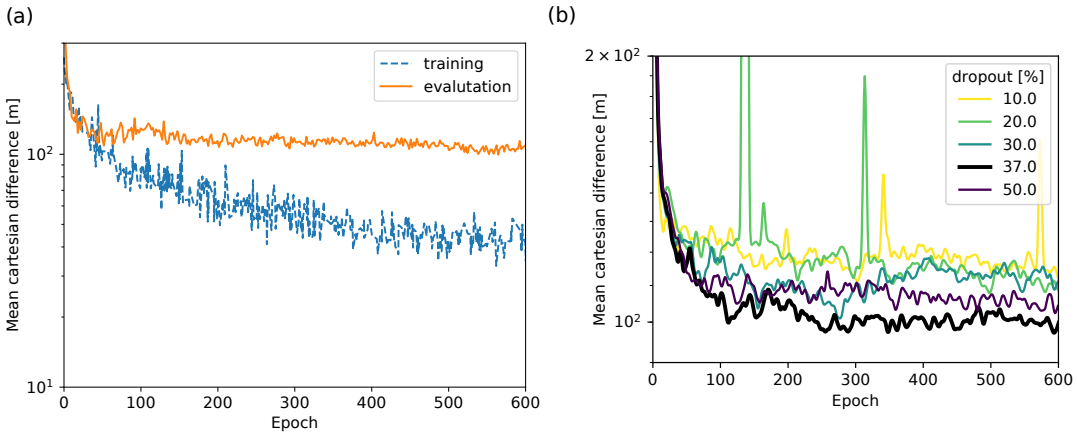

Figure 2.5: Evolution of loss function: (a) Mean Cartesian misfit between the reference catalog and the prediction by the CNN for the training dataset (dashed line) and the evaluation dataset (solid line). (b) Mean Cartesian misfit between the reference catalog and the prediction by the CNN for the evaluation dataset after training with different dropout rates.

2.4 Application of the CNN to the West Bohemia 2008 earthquake swarm

The distributions of location differences between double-difference relocated events and predicted locations of the evaluation dataset in direction of the three Cartesian coordinate system axes are centered close to zero (Figure 2.6). Hence, there is no systematic trend in predicted localizations. The lowest standard deviation error is found in East-West direction (56.4 m) as a result of the source volume shape and the North-South striking orientation. In North-South and vertical direction, the standard deviations are 123.8 m and 136.3 m, respectively.

Figure 2.7 shows the event locations of a randomly chosen subset of evaluation events obtained with our CNN and the reference locations of the double difference relocated reference catalog as crosses and points, respectively. The lines connect solutions for each event and hence indicate location differences. While in most cases the difference is small, some outliers become evident. These can mostly be explained by data quality such as interfering events.

Evaluating the mean Cartesian misfit between the reference catalog and the predictions by the CNN versus running time indicates that after approximately 500 epochs, the evaluation dataset accuracy does not improve further (Figure 2.5 (a)).

Once the network is trained, predictions are obtained rapidly: 908 events were located within 1.1 seconds.

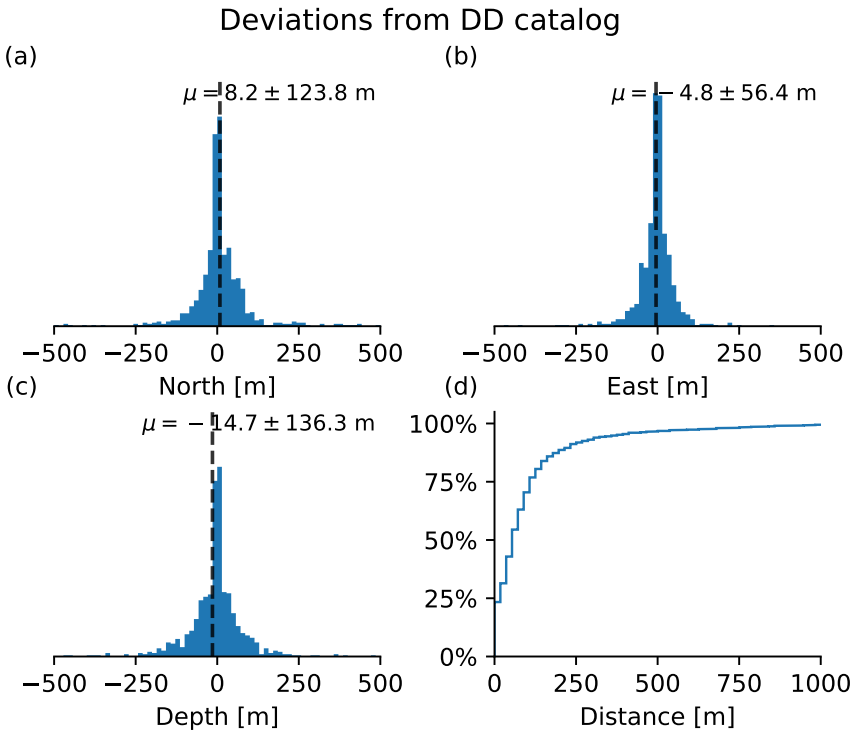

Figure 2.6: Location differences between double difference relocated events and the predicted locations (a) in North-South, (b) East-West and (c) vertical direction. Mean values (μ) are stated with standard deviations of the underlying distributions. d) Normalized, cumulative distance deviations.

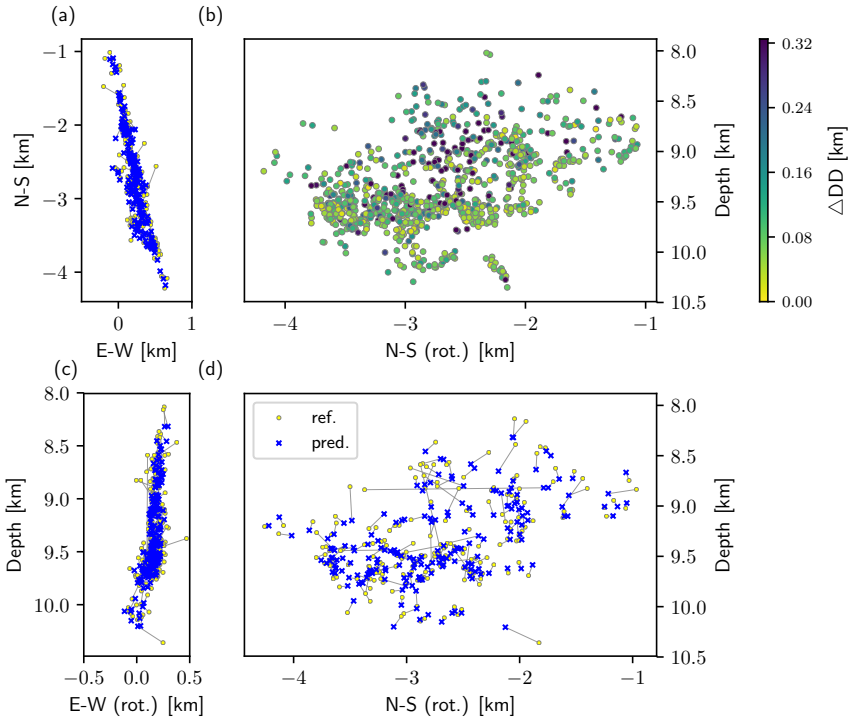

Figure 2.7: Top-view (a) and cross-sections (c) and (d) showing a subset of 200 locations as obtained by the CNN (*pred.*, crosses) and reference locations from the double-difference reference catalog (*ref.*, dots). Lines connect both locations of the same event. (b): Same cross-section as (d) but showing all 908 CNN predicted locations with color coded differences to catalog location in km. (b) to (d) are rotated by 10 degrees clockwise around the z-axis for perpendicular and parallel projections with respect to the fault.

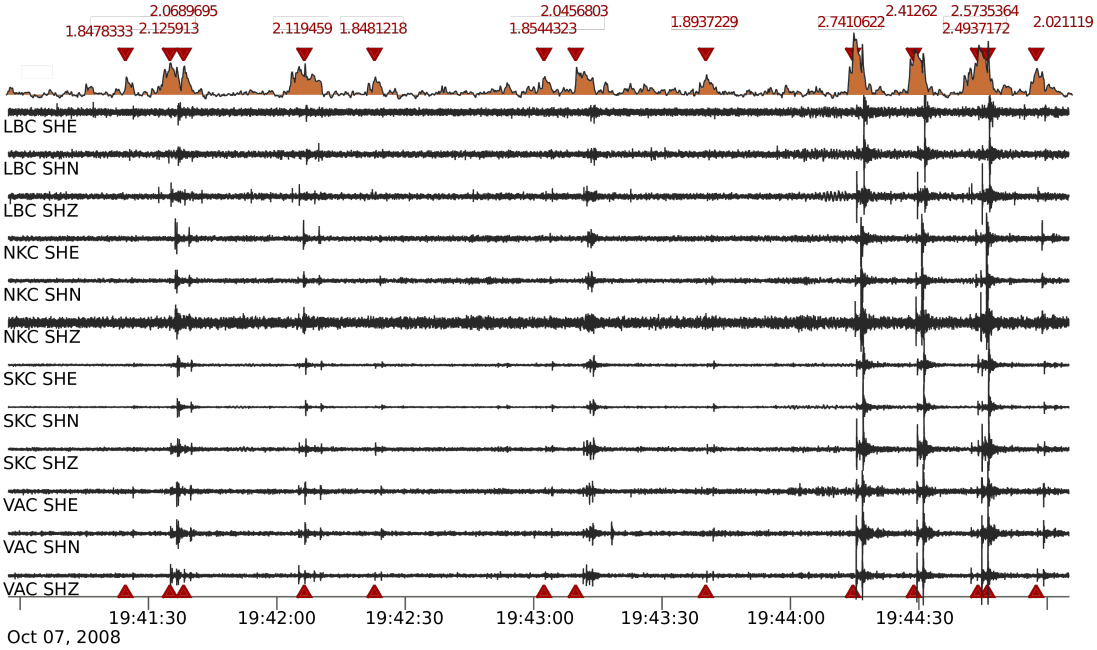

Figure 2.8: The first layer of the CNN learns characteristic features of the event waveforms and can therefore be exploited as an event detector (uppermost trace). Numbers above the uppermost trace indicate the detection level as defined in Equation (1).

2.5 Detections based on first layer activations

During the learning process filters of the first layer become sensitive to waveform characteristics of the training data. Therefore, when applied to an unseen data segment, the activation maps yield an indirect measure of the correlation with respect to the training data. This information can be harnessed as an event detector (Fig. 2.8). We define a detection level l as the activation energy contained in the first layer normalized by the energy of the input data:

$$l = \frac{\sqrt{\sum A^2}}{\sqrt{\sum I^2}} \tag{2.1}$$

where A is the activation matrix and I is the input feature matrix. We process the entire dataset in intervals of 0.2 seconds using a detection level of 1.8. We find a total of approximately 6000 detections. We manually revised a subset of 400 detections. 14 events (3.5 %) turned out to be false detections (or events too small to be visually perceptible). Another four detections were triggered by local maxima of the detection level due to S phase coda. During some swarm phases, earthquakes can occur at high rates. Our detection approach cannot safely distinguish multiple events separated by less than 3 seconds.

2.6 Discussion

In the current implementation our approach relies on manually picked P- phase onsets at a reference station for predicting locations and precisely located events for training. Hence, a significant amount of preparatory work is required.
When we apply the presented method to the North Bohemian swarm data, the average deviation between the CNN predictions and double difference located catalog is higher than the uncertainties estimated for the reference catalog itself of less than 100 meters (T. Fischer, 08/2017, personal communication). However, 88% of locations deviate by less than 200 meters from the reference catalog and 69% by less than 100 meters, which approaches double difference precision (Figure 2.6). There is no obvious trend in either Cartesian direction. However, there may be a trend to form artificial clusters. Figures 2.7(a) and (c) indicate few events present in the reference catalog, which have been located offset by about 100 meters from the well confined cluster of events which we assume is the main rupturing fault. Our predictions move those events closer to that fault. Another clustering effect is visible on the northern rim of the seismic zone where 6 events move closer together and form a smaller subcluster (laterally). However, results are biased by the error inherent to the reference catalog. To which extent those errors promote the observed trend for events to cluster is difficult to estimate and would have to be investigated with synthetic tests.
The developed method takes relatively long to train (1 hour for 600 epochs) but rapidly predicts locations (1.1 s for 908 events). In the current implementation any preprocessing is done on the CPU before examples are fed to GPU memory. Implementing the preprocessing to be performed on the GPU would certainly reduce the required training time significantly.

We limited our analysis to stacked absolute waveforms at each station. This approach was chosen, because it saves two thirds of memory as compared to treating channels separately and performed similarly good on the localization task. Nevertheless, the relative energy levels of each station contain information on source origins. Currently no expert knowledge is used because full waveforms records contain all the useful information themselves and we do not want to loose any of that information. However, including more automatic preprocessing like downsampling, filtering in different frequency bands or switching from time to spectral domain could be tested in combination with the full waveform approach.

Pretraining of the network with synthetic data could be used in order to overcome data shortages whenever not enough training examples are available and possibly remove the dependence on hand labeled training data.

Finally, we demonstrated that the activations of the first convolutional layer of our CNN can be used as an event detector. This detector is obtained as a byproduct of the localization CNN and can be used without training on noise examples which reduces training effort compared to approaches that require labeled noise. In future work, we plan to combine the two approaches to perform both event detection and localization with one single network on continuous data.

2.7 Conclusions

Deep learning techniques such as the deep CNN developed here are key technologies that allow handling of rapidly growing seismological datasets. Applying a deep CNN to full waveform data for swarm event localization shows promising results towards the step of automatic localization as it balances precision and efficiency. The presented use case demonstrates that locating densely clustered earthquakes can be done using CNNs trained on a smaller subset of localized earthquakes from the same region. Furthermore, repurposing first layer activations provides robust detection performance. Both methods can be adopted e.g. for induced seismicity or hydrofracturing applications, where working with full waveforms can be too computationally expensive and picking waveforms is not feasible due to the large number of expected events.

2.8 Data and Resources

The double difference relocated catalog and waveforms were provided by T. Fischer, Institute of Geophysics, Czech Academy of Sciences (Fischer et al., 2010) . Data was preprocessed and some plots were generated using the python based seismology environment `pyrocko` (Heimann et al. (2017)). The software package is available at `https://pyrocko.org`.
The neural network was set-up using the machine learning environment `Tensorflow` (Abadi et al. (2016), `https://www.tensorflow.org/`). Some plots were made using the `Generic Mapping Tools` (version 5.2.1) (`http://www.soest.hawaii.edu/gmt/`, Wessel et al. (2013)).
The topography shown in Fig. 2.1 is SRTM-3 data (Farr et al. (2007)).
The entire code for the CNN that is presented in this study is open to public and can be accessed at `https://github.com/HerrMuellerluedenscheid/pinky.git` .

2.9 Acknowledgments

We thank Sebastian Stober for his valuable tips and support. This work is part of the HISS project which is funded by the DFG ICDP. Project no.: CE 223/2-1. H.V-B was financially supported by Geo.X, the Research Network for Geosciences in Berlin and Potsdam under the projectnumber SO_087_GeoX. We would like to thank two anonymous reviewers and the editors for their constructive criticism and helpful comments.

Chapter 3

Monitoring performance using synthetic data for induced microseismicity by hydrofracking at the Wysin site (Poland)

Authors:
J. A. López-Comino (1), S. Cesca (1), M. Kriegerowski (1,2), S. Heimann (1), T. Dahm (1), J. Mirek (3) and S. Lasocki

Journal:
Geophysical Journal International, 2017, 210: 42-55
doi: 0.1093/gji/ggx148

Status: Published

Affiliations:
(1) Helmholtz Centre Potsdam GFZ German Research Centre for Geosciences, Germany
(2) University of Potsdam, Germany
(3) Institute of Geophysics, Polish Academy of Sciences, Krakow, Poland

3.0 Abstract

Ideally, the performance of a dedicated seismic monitoring installation should be assessed prior to the observation of target seismicity. This work is focused on a hydrofracking experiment monitored at Wysin, NE Poland. A microseismic synthetic catalogue is generated to assess the monitoring performance during the pre-operational phase, where seismic information only concerns the noise conditions and the potential background seismicity. Full waveform, accounting for the expected spatial, magnitude and focal mechanism distributions and a realistic local crustal model, are combined with real noise recording to produce either event based or continuous synthetic waveforms. The network detection performance is assessed in terms of the Magnitude of Completeness (M_c) through two different techniques. First, we use an amplitude threshold, taking into the ratio among the maximal amplitude of synthetic waveforms and station dependent noise levels, for different values of signal-to-noise ratio (SNR). The detection probability at each station is estimated for the whole dataset and extrapolated to a broader range of magnitude and distances. We estimate a M_c of about 0.55, when considering the distributed network, and can further decrease M_c to 0.45 using arrays techniques. The second approach, taking advantage on an automatic, coherence-based detection algorithm, can lower M_c to ~ 0.1, at the cost of an increase of false detections. M_c experiences significant changes during day hours, in consequence of strongly varying noise conditions. Moreover, due to the radiation patterns and network geometry, double-couple like sources are better detected than tensile cracks, which may be induced during fracking.

3.1 Introduction

Induced seismicity related to industrial processes including shale gas and oil exploitation, mining and other energy technologies are current issues that imply enough reasons to be concerned (Nicholson & Wesson 1990, 1992; McGarr et al. 2002; Davies et al. 2013; Ellsworth 2013). The assessment of the potential hazard for these triggered or induced earthquakes has become a relevant and pressing problem, especially because seismicity rates have increased in some locations. In the Western Canada Sedimentary Basin, seismic activity has been conjectured as being induced by hydraulic fracturing (Farahbod et al. 2015; Schultz et al. 2015a), gas extraction (Baranova et al. 1999) or waste water disposal (Horner et al. 1994; Schultz et al. 2014). Fracking operations in the United Kingdom were stopped for several years after the detection of two earthquakes with magnitudes of ML 2.3 and 1.5 in the Blackpool area (Clarke et al. 2014). An interesting case correlated to gas injection operations occurred offshore Spain, in the Gulf of Valencia, recording a maximum moment magnitude M_w 4.3 on 2013 October 1 (Cesca et al. 2014; Gaite et al. 2016). The major cause of injection-induced

earthquakes is associated with the disposal of wastewater into deep strata (Healy et al. 1968) and the largest events in that respect were registered in Oklahoma in 2011 November, reaching a peak magnitude of M_w 5.7 (Keranen et al. 2013). Other instances of induced seismicity, sometimes including events of M > 4, have been observed in recent years (Ellsworth 2013; Holland 2013). This work focuses on recent hydraulic fracturing operations associated to shale gas exploration and exploitation in Poland, due to the increased interest in these techniques in some European countries (SHEER project, www.sheerproject.eu).

Hydraulic fracturing usually induces weak events since the volumes of injected fluids are small (Davies et al. 2013). However, scenarios with larger earthquakes are possible, for example, if the injected fluids alter friction conditions and trigger the failure of neighbouring faults under pre-existing, tectonic stress. For example, at the Horn River Basin, British Columbia, a sequence of earthquakes reaching M_w 3 was caused by fluid injection in proximity of pre-existing faults (British Columbia Oil and Gas Commission 2012). Hydrofracking occurs when the pore pressure exceeds the minimal principal stress and the local strength is overcome. As a result of fracking, microearthquakes and aseismic slip creates the pathways for the gas/oil, enhancing the rock permeability. In general, the crack growth stops when the rupture runs out of energy. However, the progressing crack could find new energy sources, for example, in presence of tectonically loaded faults. Seismic monitoring of fracking operations is essential, so that branching out of seismicity is early detected and correlated with geomechanical operations. The ability of a local network to detect weak microearthquakes as well as larger triggered events depends on the seismic instrumentation, station number, network geometry, seismic noise and installation conditions. Consequently, assessing the performance of the monitoring setup, for example, estimating the expected magnitude of completeness (M_c) or the smallest detectable magnitude, is a fundamental step for a later reliable analysis of the forthcoming seismicity. In this work, we discuss how to address the problem of detection performance before the target hydraulic fracturing operation takes place. With this goal, we make use of the concept of M_c, defined as the lowest magnitude at which 100 per cent of the earthquakes in a space–time volume are reliably detected (e.g. Rydelek & Sacks 1989; Wiemer & Wyss 2000; Woessner & Wiemer 2005).

Multiple techniques have been proposed for the estimation of M_c. Mignan & Woessner (2012) classify them as catalogue-based and network-based methods. The first group of methodologies is mostly based on the assumption of self-similarity of the earthquake process, implying that M_c is the minimum magnitude at which the observed cumulative frequency magnitude distribution departs from the Gutenberg–Richter law (Wiemer & Wyss 2000; Cao & Gao 2002; Marsan 2003; Woessner & Wiemer 2005; Amorese 2007; Mignan et al. 2011). The second category uses the network distribution to estimate M_c: this is either done through the analysis of diurnal variations (Rydelek & Sacks 1989), the comparison of amplitude–distance curves and the signal-to-noise ratio (SNR, Sereno & Bratt 1989), seismic threshold monitoring (Gomberg 1991; Kværna & Ringdahl 1999; Kværna et al. 2002), numerical simulation (D'Alessandro et

al. 2011a,b; D'Alessandro & Stickney 2012), Bayesian statistics (Mignan et al. 2011; Kraft et al. 2013; Mignan & Chouliaras 2014) and detection probability estimates for each seismic station (Schorlemmer & Woessner 2008; Nanjo et al. 2010; Plenkers et al. 2011; Maghsoudi et al.2013, 2015). Furthermore, understanding the microseismic source mechanisms and stress state has gained more interest recently and should be considered in an appropriate estimation of the detection performance (Nolen-Hoeksema & Ruff 2001; Baig & Urbancic 2010).

All the catalogue-based methods described above can only be used in a retroprospective manner, typically after several years of monitoring under the assumption of a steady earthquake generation process. This is not useful for planning the monitoring of fracking operations, which last only few months and are highly transient processes. Therefore, we propose a prospective evaluation method where we apply a combination of the aforementioned methods and synthetic data in order to assess the monitoring performance before the fracking operations start. To achieve this goal, we discuss how to generate a realistic synthetic microseismic catalogue and synthetic waveform data sets, accounting for the main characteristics of the expected source mechanisms for hydraulic fracturing as well as realistic noise conditions. The detection performance is assessed for the synthetic data using two different techniques. In the first case, we use an amplitude threshold, taking into account a station-dependent noise level and different values of SNR. In this case, the detection probability of each station is estimated for each synthetic event, and extrapolated to a broader range of magnitudes and distances from Bayesian statistics. The final map of the M_c is then estimated by combining the detection performance of different stations, considering the network geometry. The second approach follows the application of an automatic detection algorithm to the continuous synthetic data set, comprised of synthetic event waveforms and continuous real noise data. In this study, we apply a recently developed automated full waveform detection algorithm based on the stacking of smooth characteristic function and the identification of high coherence in the signals recorded at different stations (Lassie, https://gitext.gfz-potsdam.de/heimann/lassie, Matos et al. 2016; Heimann et al., in preparation).

3.2 Monitoring Network at the Wysin Site (Poland)

In order to assess the sensitivity of microseismicity to hydraulic fracturing operations, we perform a seismic monitoring at a shale gas exploration/exploitation site in Pomerania (Poland). In this area, close to the village of Wysin, Polish Oil and Gas Company (PGNiG) drilled two horizontal boreholes, named Wysin 2H and Wysin 3H, designed for fracturing under Stara Kiszewa Concession No. 1/2011//p for prospecting and exploration of oil and natural gas. The horizontal boreholes are located at 3955 and 3865 m below the surface and they are oriented WNW-ESE with an approximate horizontal length of 1.7 km each.

The seismic monitoring installation is part of a broader survey concept,

also monitoring groundwater conditions and air pollution, planned and deployed thanks to the EU project SHEER (www.sheerproject.eu). The network is composed of a surface installation and a shallow borehole installation, covering a region of 60 km2 (Fig. 1). The surface network includes six broad-band stations surrounding the drilling site at distances of 2.1–4.3 km, with a good azimuthal coverage (maximal gap 90°). In addition, short-period stations are arranged in three small-scale arrays, with apertures between 450 and 950 m. Broad-band stations are equipped with GÜRALP CMG-3ESP sensors, and record continuously with a sampling rate of 200 Hz. Short-period stations are either equipped with a combination of MARK L-4C-3D sensors or GeoSIG VE-53-BB sensors. The sampling rate of all short-period stations is 500 Hz. The shallow underground installation is composed of three seismometers (Geotech Instruments KS-2000) installed at 50 m depth. The installation was started on summer 2015 and the network is fully operational since 2015 November. However, two borehole stations (GW3S and GW4S) had suffered from technical problems and were replaced by two other stations with sensors Nanometrics Trillium Compact Posthole 120 s at the end of 2016 April. For this reason, we exclusively use seismic data of 2016 May to characterize the noise level at each station. This period precedes the beginning of the hydrofracking operations, which started in 2016 June at a depth of about 4000 m.

3.3 Synthetic Microseismic Catalogue

We adopt a recently developed tool to generate a synthetic catalogue and waveform data sets, which realistically accounts for the expected microseismicity patterns (Kriegerowski et al. 2015). The procedure consists of two steps: (1) the generation of a synthetic seismic catalogue which reflects the characteristics of the expected seismic activity and, (2) based on that the generation of realistic synthetic full waveforms combined with real noise. We consider two types of seismicity in the study region: (i) a background seismicity, taking place independent from the fracking operations, with focal mechanisms controlled by the known orientation of tectonic stress and the unknown orientation of local faults, and (ii) induced seismicity, which is controlled in its growth and moment tensors by the superposition of tectonic and induced stresses. For this second group of potential microseismic events, the regional tectonic in situ stress state controls the direction of hydraulic fracture growth in the unperturbed rock formation (e.g. Nolen-Hoeksema & Ruff 2001; Zang & Stephansson 2010). The knowledge about the orientation of the maximum horizontal compressive stress (SHmax) is thus vital to establish possible candidate geometries for the expected focal mechanisms. The horizontal fracking drillings are expected to be perpendicular to SHmax, as such stress conditions favour the propagation of fractures opening in the direction of the least compressive stress (Sh). It has been shown that the processes involving rapid fluid injection can produce tensile failures with significant non-double-couple (DC) components, opening in the direction of the

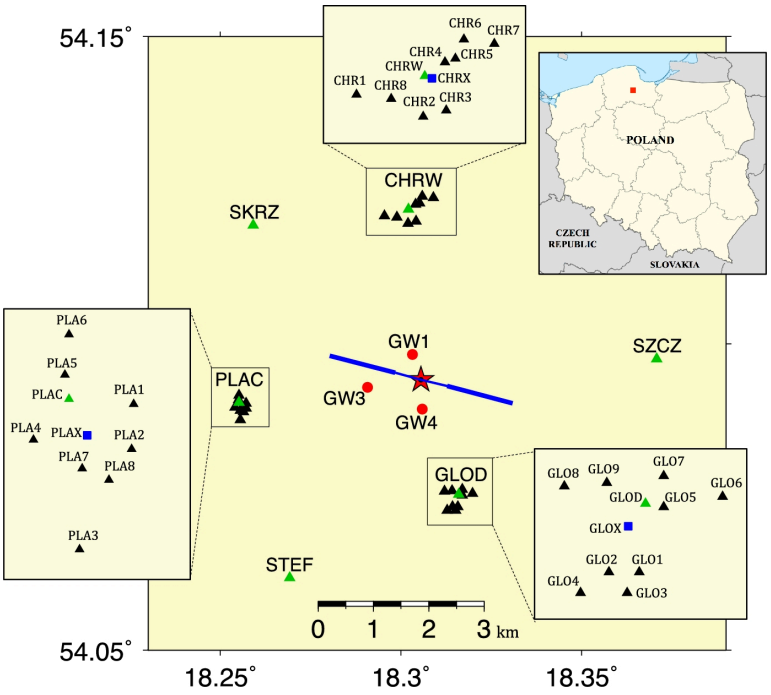

Figure 3.1: Map of seismic monitoring composed of six broad-band stations (green triangles), three small-scale arrays (inset boxes), each one composed of 8–9 short-period stations (black triangles) and three shallow borehole stations (red circles). Blue squares in inset boxes correspond to central locations of each array. Fracking area (red star, vertical borehole) and horizontal boreholes (blue lines) are shown. The inset map shows the fracking area (red square) in Poland.

minimal compressive stress and closing after the injection (e.g. Economides & Nolte 2003 and others). The orientation of microfractures produced by the hydrofracking depends on the superposition of the stress perturbation induced by the hydraulic fracturing process and the background regional stress field.

Our synthetic catalogue should be consistent with the aforementioned conditions. For this purpose, we consider four families of microseismicity, assigning 1000 events to each one (Fig. 2); the subjective choice of the number of events has no major implications, since they are only used to assess the detection performance for different magnitudes and rupture types. We use a Hudson source-type plot (Hudson et al. 1989) to discuss the non-DC components and a graphical representation of tension (T), pressure (P) and null (B) axis to discuss the focal mechanism orientations. The first group of seismic sources (family 1) resembles the background seismicity: these sources are modeled by DC focal mechanisms (this group of synthetic events is hereafter referred as 'DC' family). Since the orientation of small local faults is unknown, we adopt a random distribution of orientations (i.e. random strikes and dips). The rake value, instead, is controlled by the strike and dip of the rupture plane and SHmax of the background stress. In our study area, located within the East European Craton geodynamic domains, the maximum horizontal stress is oriented SHmax $\sim 15^\circ$ (World Stress Map database release 2008; Heidbach et al. 2008), almost perpendicular to the horizontal fracking drillings. The compressive regime implies the occurrence of thrust or strike-slip events, with no normal faulting (see triangular diagram in Fig. 2). To simulate possible minor deviations from a pure DC source due to the fluid injection, we include a random 10 per cent perturbation in the moment tensor entries. According to Baig & Urbancic (2010), induced fractures tend to open in the direction of the minimal compressive stress, closing in the same direction after the injection. We thus model two families of moment tensors, dominated by positive (family 2) and negative (family 3) tensile cracks with dipoles oriented parallel to Sh with a randomized deviations of $\pm 25^\circ$ (according the quality data for this orientation from the World Stress Map); also in this case, moment tensor configurations are finally perturbed, as for the DC family. The last family (family 4), defined as 'random full moment tensor', represents random moment tensor sources and thus account unexpected processes. This family shows a clear dispersion both in the Hudson and focal mechanism orientation plots.

A proper representation of microseismicity should further consider a suitable distribution of magnitudes and hypocentres (Fig. 3). The instrumental sampling of our fracking experiment (500 Hz) and the distance to the horizontal fracking drillings ($\sim$4 km depth) do not favour detections with moment magnitude below -1; on the other hand, the few previous hydraulic fracturing experiments in Europe never reported seismicity of magnitude greater than 3 (Clarke et al. 2014). We then adopt a Gutenberg–Richter distribution with b = 1 and a = 1.84, to distribute magnitudes in between these limits. Moreover, we assume a circular fault model of Madariaga (1976) and an average stress drop of 2.7 MPa for earthquakes within the chosen magnitude range (Kwiatek et al. 2011). Based on this, we can estimate a maximum rupture length of $\sim$350 m for the largest

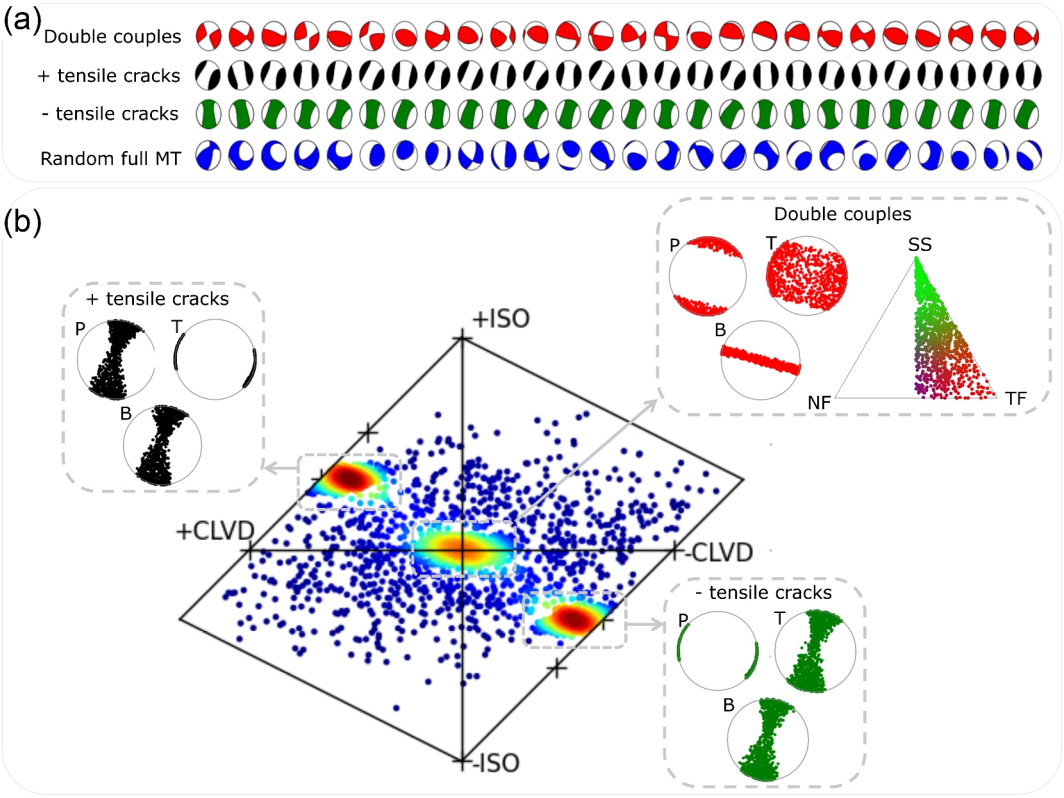

Figure 3.2: (a) Examples of focal mechanisms for different families of expected microseismicity in hydraulic fracturing. (b) Hudson source-type plot showing the Gaussian Kernel density for the complete synthetic microseismic catalogue, where red denotes higher and blue regions of lower event densities, respectively. The boxes with dashed grey frames identify the concentrations of seismic sources and the T, P and B axes plots belonging to the double-couple, positive and negative tensile crack families. The triangle diagram indicates the distributions of double-couple focal mechanism. The blue points dispersion corresponds to the random full moment tensor family. Acronyms in Hudson plot mean isotropic (ISO) and compensated linear vector dipole (CLVD)

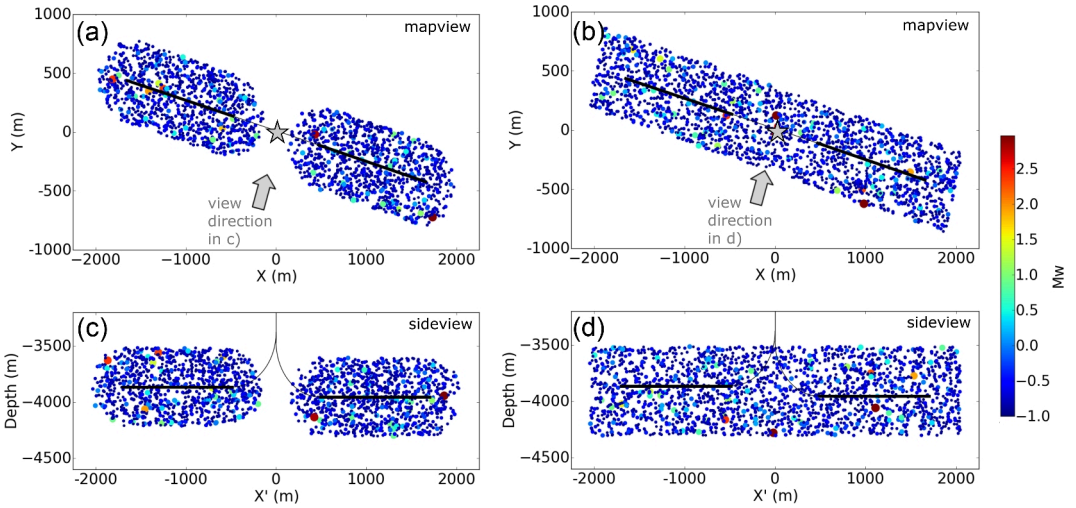

Figure 3.3: Distribution of hypocentres and magnitudes for the synthetic microseismic catalogue in the Wysin fracturing area. (a) Distribution for the random full moment tensor and double-couple families. (b) Distribution for the positive and negative tensile crack families. The size and colour of each point is scaled to the moment magnitude. Grey star indicates the vertical drilling. Black lines show the fracking boreholes and the thicker line identifies the zone allocated for fluid injection. Panels (a) and (b) show the map views, and (c) and (d) the side views.

events. This value can be used to define the spatial distribution of induced seismicity, in coherence with previous results in the United States, where most of the maximum fracture lengths have been less than 100 m, reaching peak values of 600 m (e.g. Davies et al. 2012; Fisher & Warpinski 2012). We consider that the hypocentres of small fractures are constrained within a volume defined by the maximal possible rupture, which extends 350 m around the segments of the horizontal wells where the fracking takes place. This corresponds to a worst case scenario, where the largest fracture nucleates close to the well and propagates unilaterally for the length of 350 m. While the induced seismicity events (families 2 and 3) are constrained within this volume (Fig. 3a), background DC sources (family 1) and random sources (family 4) are randomly distributed in a slightly broader region (Fig. 3b). Origin times are distributed randomly within a time period of one month (which is in the order of the duration of the whole fracking process). As a result of this procedure we obtain a catalogue of 4000 synthetic events, divided in four families. The catalogue includes the following information: origin time, location, moment magnitude, moment tensor and its decomposition into isotropic, DC and compensated linear vector dipole, radius, duration, stress drop and event family.

After generating the synthetic seismic catalogue, we compute the respective seismograms at all the stations of the monitoring network, both at the surface and at the shallow borehole installations. A realistic local crustal model is necessary to properly compute the synthetic waveforms. A 1-D velocity profile could be

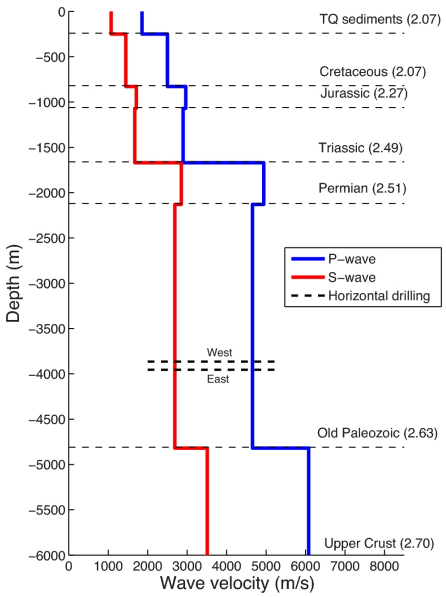

Figure 3.4: Local crustal model for the Wysin site. The P-wave velocity profile is obtained for the coordinates 54.09° N and 18.30° E from Grad et al. (2015). Each layer is identified with the name and the density value in g/cm^{-3}. The thick black dashed lines indicate the depth of the west and east horizontal wells.

modeled from ground samples of the vertical fracking drilling. Since we do not dispose of such information, we relied on previous studies on the broader region of interest. We use a P-wave velocity profile extracted from a high-resolution 3-D seismic model for Poland, at the location of the fracking site (Grad et al. 2015), which is shown in Fig. 4. The S-wave velocity profile was built assuming a typical scaling to the P-wave velocity (vp = 1.73 vs), while densities of each layer were obtained from Grabowska et al. (1998). A constant attenuation factor is used for all layers (Qp = 120 and Qs = 60, Król et al. 2013). The low Q value for S and P waves is representative for the sedimentary basin in Poland and leads to a high attenuation in the frequency range of study. The reflectivity method (Wang 1999) was used to precalculate Green functions up to 500 Hz for the chosen velocity model and a proper range of source depths and epicentral distances. Finally, three-component synthetic full waveforms (Fig. 5a) were generated using the Pyrocko package (http://emolch.github.io/pyrocko/, Heimann et al. 2014), combining the Green's functions and moment tensors of the synthetic catalogue. We convolve synthetic seismograms with the transfer functions of each receiver. Finally, to reproduce true monitoring conditions at the different station locations, we add real noise to synthetic traces (Fig. 5b), using recordings at those stations from 2016 May. Thereby, we can use different synthetic data sets: noise-free synthetic seismograms and noise contaminated continuous seismograms.

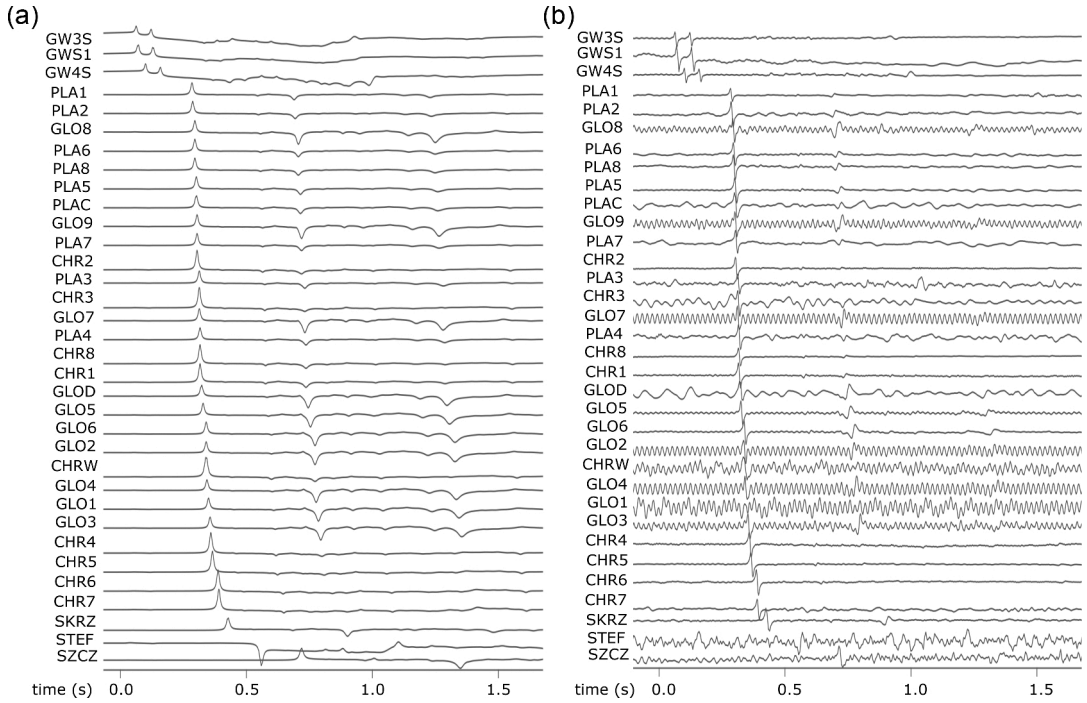

Figure 3.5: (a) Raw synthetic waveforms (displacement) and (b) real noise contaminated continuous seismograms (velocity) for one positive tensile crack event with $M_w = 0.97$. (a) and (b) show the same event for the vertical component in each seismic station. The signal in (b) is bandpass filtered between 2 and 80 Hz and notch filtered at 50 Hz. Zero time corresponds with the origin time.

3.4 Detection Performance using Amplitude Threshold

Any detection algorithm needs to define a threshold or trigger level according to boundary conditions. Records of ambient noise during a time period prior to a seismic experiment are always useful in order to estimate suitable values for such detection level. As a prior approximation to assess the monitoring detection performance, we propose to compare the maximum amplitudes of our synthetic waveforms with an amplitude threshold previously defined according to the real noise records at each station. First, the maximum amplitudes of noise free synthetic full waveforms are analyzed in function of the hypocentral distance (r) and the moment magnitude (Fig. 6). The amplitude increases exponentially with the magnitude, while due to the geometrical spreading amplitudes decay with inverse dependence to the hypocentral distance (1/r). The variability of focal mechanisms and moment tensors in our catalogue is responsible for the amplitude variations with respect to this general patterns (see amplitude profiles in Fig. 6). In fact, we observe in general larger amplitudes associated with DC sources than tensile cracks. Second, a seismic noise analysis is carried out using one-month data (2016 May) before fracking operations to define the amplitude threshold.

The detection performance of each station will additionally depend on the specific noise conditions. Therefore, we consider random noise samplings at each station and used them to estimate an average noise conditions in terms of ground displacement (Fig. 7). Although the detection procedure would be actually performed on raw traces, our approach was chosen to quantify the detection amplitude in terms of maximal displacements. Choosing a physical magnitude such as displacement for the detection threshold is convenient for comparison with future studies, in order to be independent on the sensor instrumentation. Mean and standard deviation values are obtained from the noise sampling at different hours in order to observe daily variations. Larger noise levels during day hours (6:00 - 18:00 h) are found as a general pattern. However, different patterns of smoother variations are also found for some stations (e.g. a noise level increase between 15:00 and 24:00 h at CHR3 and GW4S, see Fig. 7a). We choose the amplitude threshold for each station according to the averaged values during the day and night hours (Fig. 7). In this way, we can clearly identify the most noisy stations between 2 and 80 Hz (e.g. PLA4, PLA7 and PLA8) and most quiet ones (e.g. GLO5 and GLO7). The borehole stations, which are located at shallow depth (around 50 m below surface) show similar noise levels between 2 and 80 Hz as some surface stations. The detector level is then defined according these amplitude thresholds and a fixed SNR.

We can now compare the maximal amplitude of noise-free synthetic waveforms at each station and the corresponding station noise level (either for day or night hour, depending on the event origin time). Imposing different SNR requirements, we can estimate detected and undetected events at each station. Thereby, the M_c can be calculated straight by the lowest magnitude above which

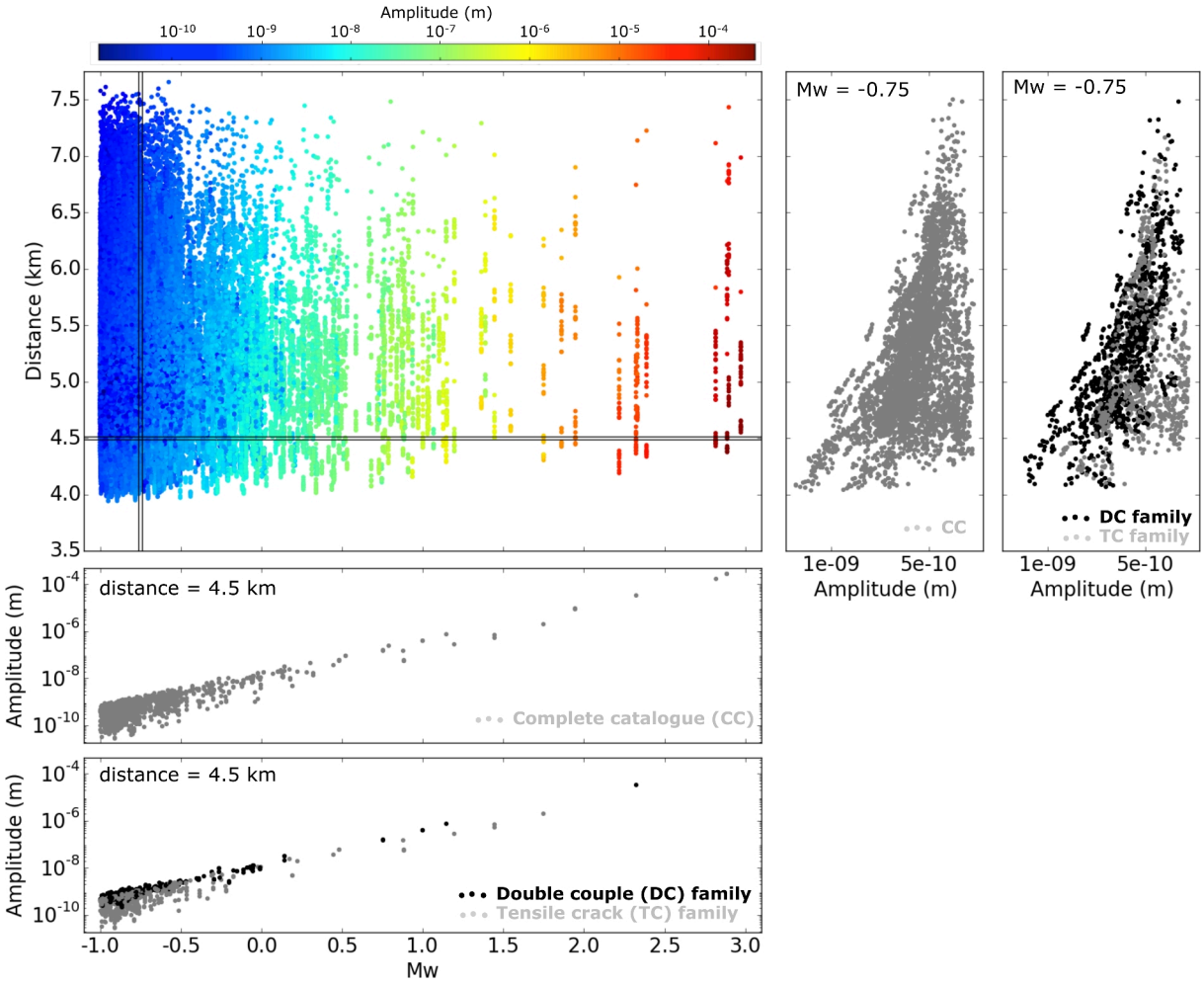

Figure 3.6: Maximum amplitudes according to the hypocentral distance for each station and the moment magnitude for each source are plotted for the complete synthetic microseismic catalogue. Amplitude profiles are plotted for a fixed hypocentral distance (4.5 km) and a fixed moment magnitude (M_w = -0.75) using grey dots. Additionally, we also show these same amplitude profiles considering those events belonging to the double-couple (black dots) and tensile crack (grey dots) families.

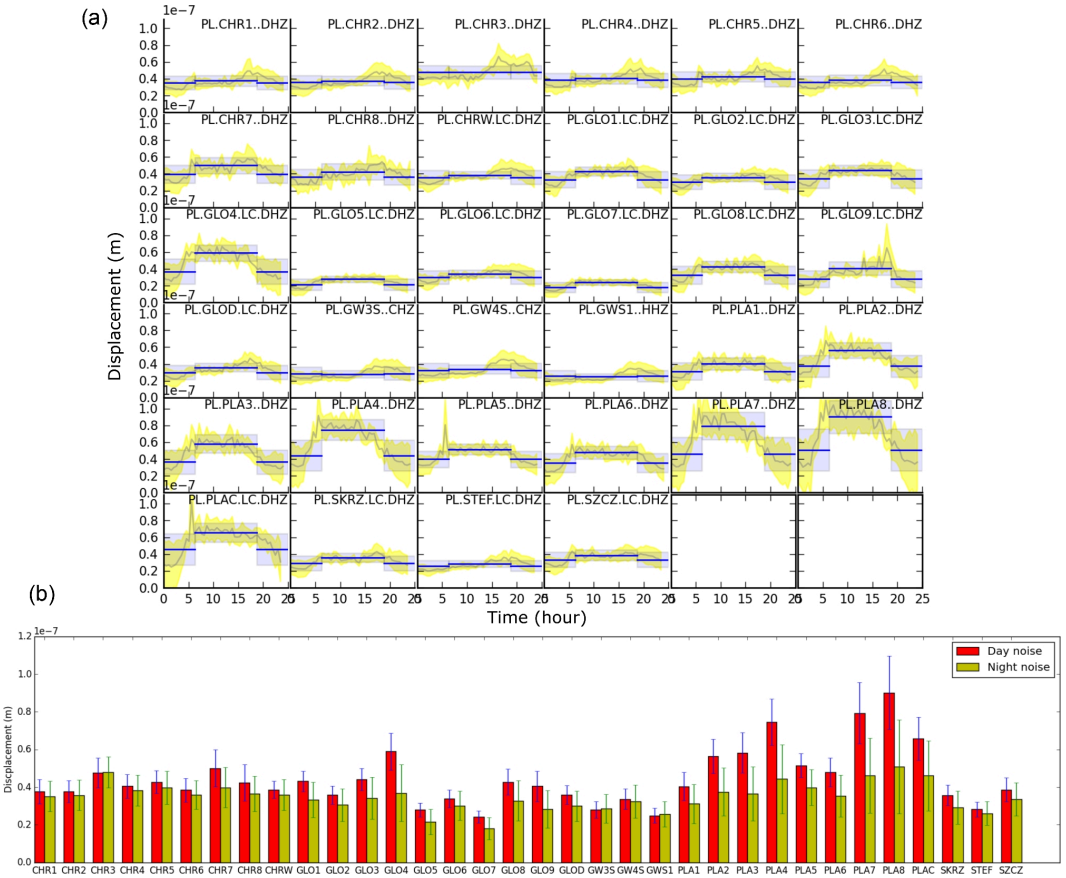

Figure 3.7: Noise analysis in each seismic station using one-month data between 2 and 80 Hz (vertical component) before fracking operations. (a) Mean (grey line) and standard deviation (yellow area) values in displacement are obtained from the random noise sampling taking into account the different hours of the day. Average amplitude threshold for day and night (blue line) and the standard deviation (light blue area) are estimated according the diurnal variation between 6:00 and 18:00 h. (b) Bars diagram with the amplitude thresholds and its uncertainties during day (red bar) and night (yellow bar) for each station.

all synthetic events are robustly detected (i.e. detected by at least four stations), taking into account both day and night amplitude thresholds (Fig. 8). The increase of M_c with required SNR reflects the fact that imposing a larger SNR for detection will decrease the number of detected events and increase the M_c. A potential empirical law can adjust this relation with fit parameters d1 and d2:

$$M_c = d_1 SNR^{d_1} + d_0 \tag{3.1}$$

In this equation, since the noise level is fixed, a low SNR means that events which have low amplitude waveforms (i.e. small magnitude) can be detected; in the extreme case of SNR equal to 0, we should detect all synthetic events, so that d0 can be defined by the minimum magnitude of our synthetic catalogue, in our case, d0 = -1. The variation of M_c quantifies the monitoring performance of our network for different values of the SNR detection threshold. We estimate $M_c \sim 0.60$ during day hours and $M_c \sim 0.55$ during night hours, when considering a realistic SNR = 2. Another interesting issue concerns the evaluation of the contribution to M_c for each family of source mechanisms. The tensile crack families constrain the M_c for the complete synthetic catalogue, as these events are more difficult to be detected. Conversely, for the DC family alone, the M_c is reduced to ∼0.1, for example, considering SNR larger than 1 (Fig. 8). The different detection performance arises from the fact that DC sources produce larger amplitudes than tensile cracks with the same magnitude, as previously discussed in Fig. 6. It should be noted, however, that this also implies some challenges in the correct estimation of the magnitude for both DC and tensile sources. An amplitude-based magnitude definition, ignoring the radiation pattern of different type of sources, may lead to underestimate the magnitude of tensile sources (or overestimate the magnitude of DC sources). Fit parameters in eq. (1) vary slightly for day, night and the selected family: d1 [1.35-1.22]; d2 [0.23-0.21]. Another important aim concerns the application of array techniques to improve the detection performance of our network. In general, the SNR improves with the square root of the number of stations belonging to an array (e.g. Rost & Thomas 2002, 2009). Applying such approximation to the three arrays, we can add fictitious stations located in the centre of each array (Fig. 1), with smaller amplitude thresholds. In this case, the fit parameter d1 takes values between 1.29 and 1.17, and M_c is slightly decreased by about 0.05, with respect to the distributed network setup (Fig. 8). Our next purpose aims to extend spatially the previous values of M_c around the fracking area for a realistic case of SNR = 2. We can obtain a map to assess our spatial performance combining the probability of detection (Pd) and empirical relations from Bayesian statistics. Taking into account each station and its corresponding amplitude threshold, we can divide the catalogue into detected (N+) or not detected (N-) events (Fig. 9a). The Pd at a single station for different magnitudes (M) and source–receiver distances (r) from the complete synthetic catalogue is estimated according to (Schorlemmer & Woessner 2008):

$$P_d(M, r) = \frac{N_+}{N_+ + N_-} \tag{3.2}$$

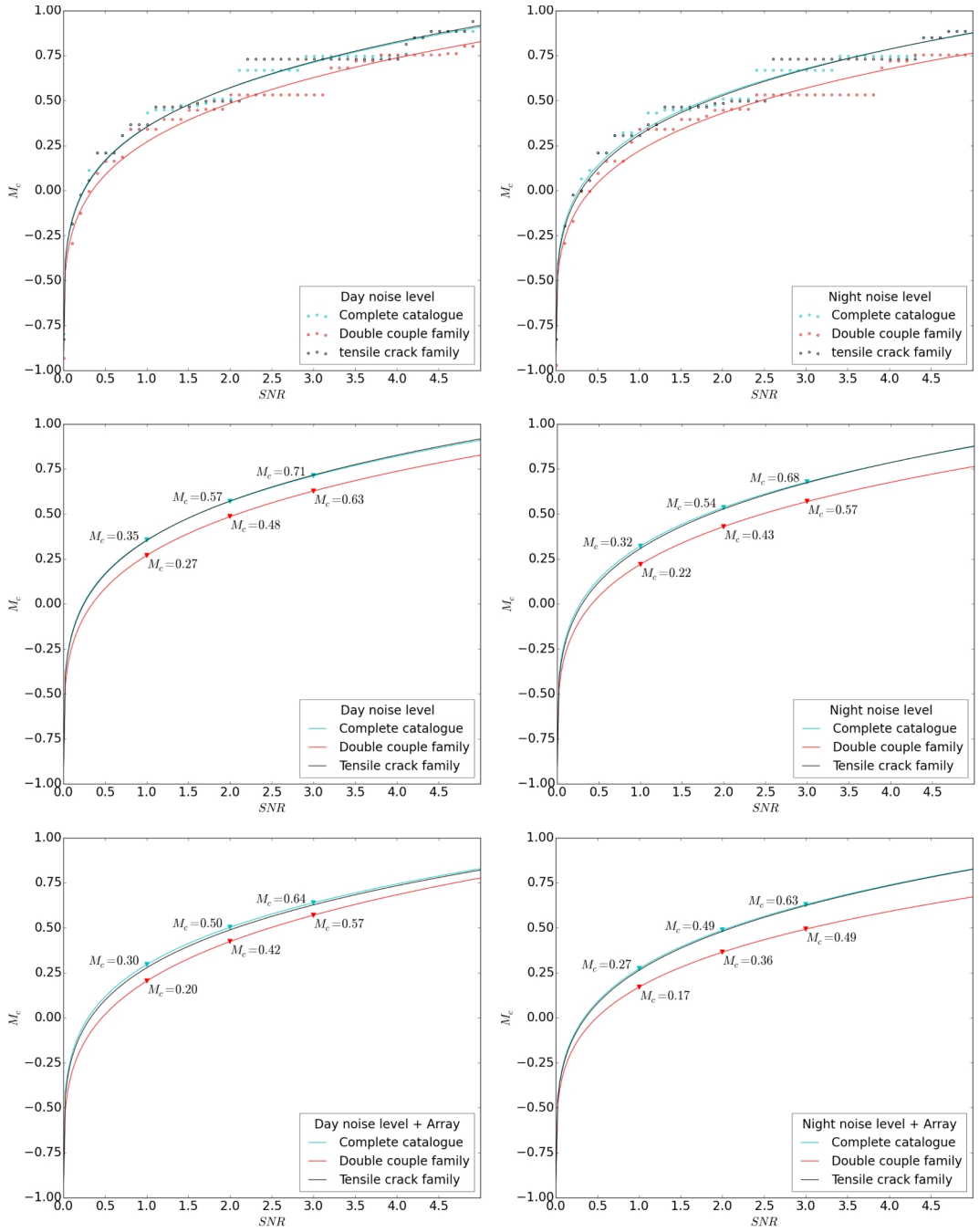

Figure 3.8: M_c versus SNR relation according to the noise levels during day (first column) and night hours (second column). Potential empirical laws can adjust the stepwise increase observed for our synthetic catalogue (first row). The monitoring performance is assessed for the Wysin network in terms of M_c for the SNR values of 1, 2 and 3 (second row). Note that we show the same empirical laws in first and second rows. The monitoring performance is improved using array techniques (third row). Cyan lines identify the curve using the complete synthetic catalogue, red lines those for the events included in the double-couple family and black lines those for the tensile crack family only.

As a result, we obtain estimates of each single-station detection probability as a function of magnitude and hypocentral distance (Fig. 9a). However, this information is not complete for a broader domain of magnitudes and hypocentres, because of the limited spatial and magnitude distribution of the synthetic catalogue. In general, detection probabilities should not decrease with increasing magnitude or with decreasing source–receiver distance. The single-station detection performance can be extrapolate through empirical relationship such as in Mignan et al. (2011):

$$M_c(r, k) = C_1 r^{C_2} + C_3 \tag{3.3}$$

where M_c is dependent on the distance r to the kth nearest station with fit parameters C1, C2 and C3. We scan the configurations of these coefficients, which are allowed to span within reasonable intervals (C1 in [4, 12], C2 in [0.04, 0.10] and C3 in [-3, -10], Mignan et al. 2011; Mignan & Chouliaras 2014; Schultz et al. 2015b). These curves divide the magnitude–distance space in a region of large magnitude and small distances, where the detection is more likely, and a region of small magnitude and large distances, where the event detection is more difficult. The best configuration of C1, C2 and C3 to define the completeness magnitude is here chosen only looking at the first region (below the curve) by (1) imposing that the number of detected events in this region by at least 95 per cent and (2) by maximizing the number of events in this region (Fig. 9). A shift is observed in this empirical relation towards larger magnitudes for the noisiest stations and, conversely, for quiet stations. The same analysis is performed for each array, which has the best detection performance (Fig. 9). A regular grid at an averaged depth for the horizontal fracking drillings of 3.91 km is fixed to map spatially the M_c, based on the previous empirical relations and imposing again the simultaneous detection by at least four stations (Fig. 10). Ignoring the noise heterogeneity on the surface, then the minimum values of the M_c would be found at the array locations, because of the larger station density. Considering real station-dependent noise conditions alter significant the spatial distribution of the detection performance, with a decrease in the M_c around the fracking area to match similar values such as those in Fig. 8.

3.5 Detection Performance using Coherence

Automatic event detection and location procedures for monitoring local and regional seismicity are widely used by the seismological community. Coherence techniques have improved the traditional automatic detectors [e.g. short-term average (STA)/long-term average (LTA) techniques] and have been employed in microseismicity case for hydrofracking (López-Comino et al. 2017). Our next approach proposes to apply a recently developed automated full waveform detection and location algorithms (Lassie, https://gitext.gfz-potsdam.de/heimann/lassie, Matos et al. 2016; Heimann et al., in preparation), using real noise contaminated continuous seismograms. We simulate a continuous synthetic data set by convolving synthetic seismograms from the complete catalogue with the instru-

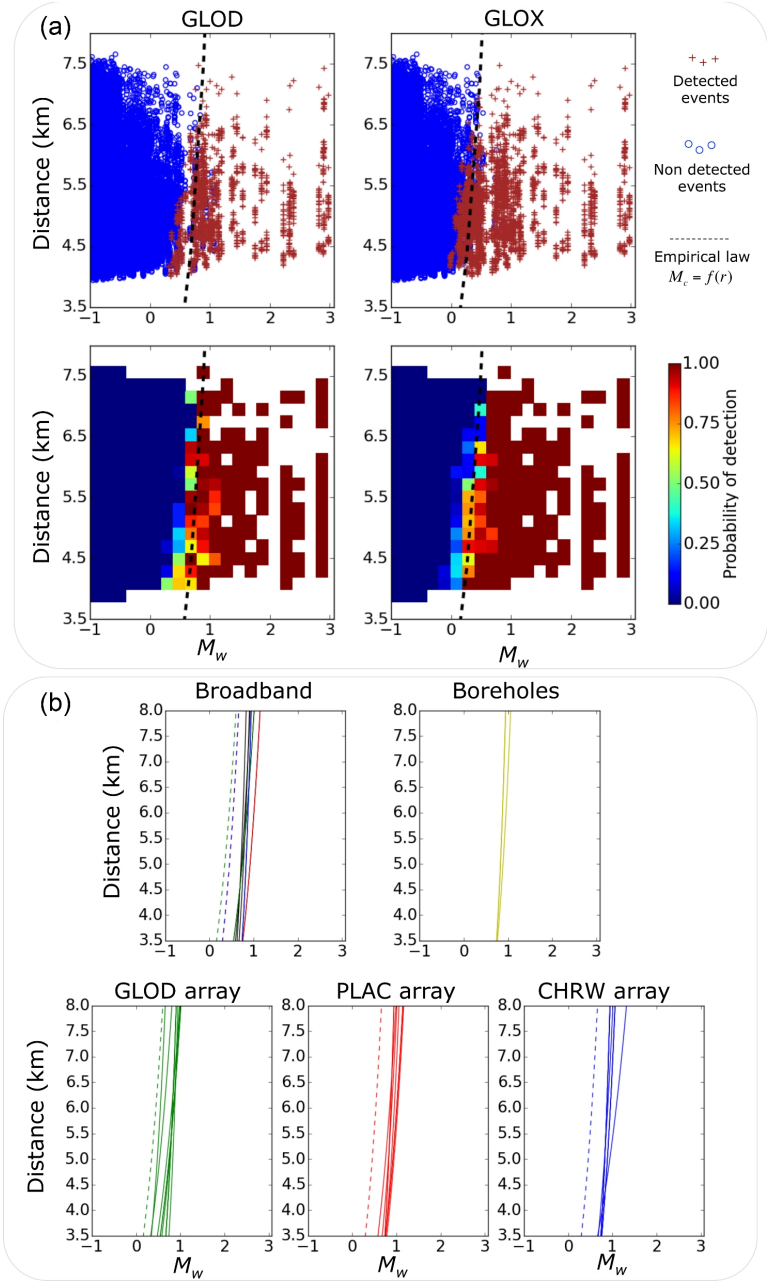

Figure 3.9: (a) Plot of all detected (brown crosses) and not detected events (blue circles) for the synthetic catalogue using an amplitude threshold previously calculated with real noise and SNR = 2 in the seismic station GLOD and the fictional stations for the array GLOX (first row). Probability of detections in the previous two stations (second row). Black dashed lines show the empirical relationship obtained by eq. (3). (b) Empirical relationship for all stations (solid lines) and fictional stations for the array (dashed lines). Stations in array GLOD are shown in green, array PLAC in red, array CHRW in blue and borehole stations in yellow. The inbox for the broad-band stations show in black colour the stations SZCZ, STEF and SKRZ; GLOD in green; PLAC in red and CHRW in blue.

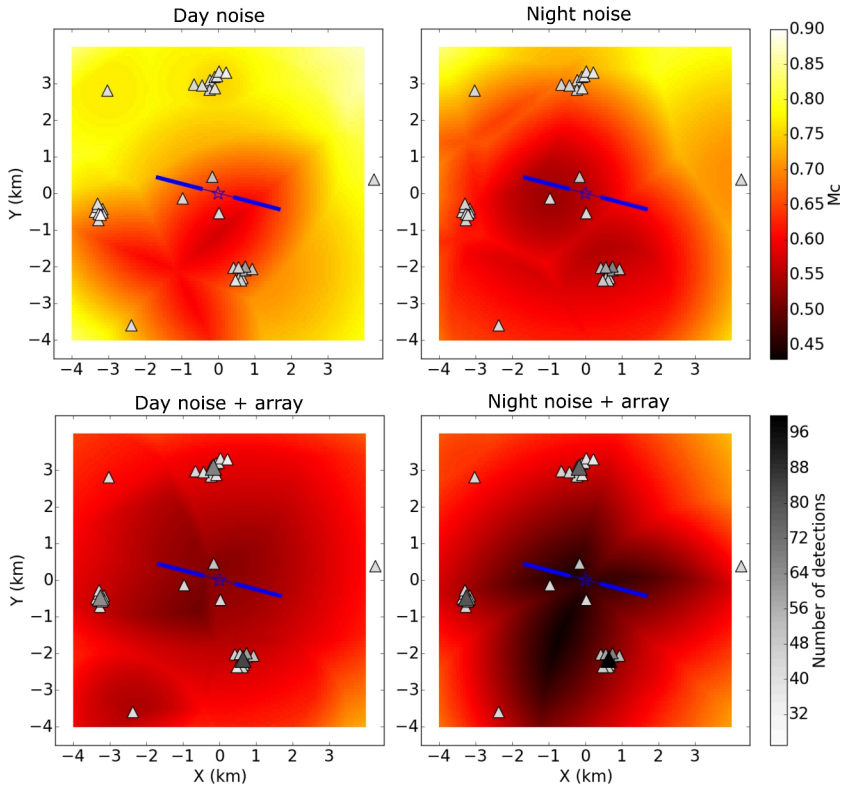

Figure 3.10: Spatial monitoring performance at Wysin site in terms of magnitude of completeness using an amplitude threshold estimated from real noise during day hours (first column) and during night hours (second columns) with SNR = 2 (first row). Improved spatial monitoring performance using array techniques (second row). Grey colour scale identifies the number of synthetic events detected for each station.

mental response and adding real noise, which is chosen randomly from the 2016 May data set but constrained around the average timing of the signal, so to preserve the daily variation of seismic noise. This python-tool earthquake detector is based on the stacking of characteristic functions of P and S waves according to the energy variations calculated from the square amplitudes of each trace. It follows a delay-and-stack approach, where the likelihood of the hypocentral location in a chosen seismogenic volume is mapped by assessing the coherence of arrival times at different stations (see Cesca & Grigoli 2015 for an overview). However, in the Lassie implementation, the adoption of smooth characteristic function calculated from normalized amplitude envelopes allows to reduce the spatial and temporal sampling (Heimann et al., in preparation). Data are first bandpass filtered between 2 and 80, Hz including an additional notch filter at 50 Hz (see Fig. 5b). The characteristic P- and S-wave functions for each station are then calculated, shifted and stacked according to P and S average velocities in our study region. These operations results in a spatiotemporal matrix of coherences values. The detection is performed searching the maximal spatial coherence at each time step, defining a detection every time this value trespasses a chosen threshold (Fig. 11).

The performance of this tool strongly depends on the selection of the coherence threshold. Consequently, we need to define an optimal detector level, able to detect weak events while not increasing excessively the number of false detections (Fig. 12). First tests indicate that events with M_w lower than -0.6 are entirely hidden in the real noise requiring too low detector levels, which would produce a great number of false detections. We show here the results using thresholds larger than 700 to remove these inconsistencies. A conservative choice would correspond to values able to minimize the number of false detections generated for random coherences in our data set. A better alternative is to require a threshold, for which the number of real detections is larger than the number of false detections. Our synthetic catalogue suggests appropriate thresholds could be chosen between 800 and 1000, with better performance during night hours, where the false detections disappear at threshold of $\sim$950. The detection performance depends on the chosen detector threshold in a similar way as in the previous case, using amplitude threshold with different SNR values (Figs 8 and 12). M_c shows again a stepwise increase with the detection threshold, but the monitoring performance is significantly improved thanks to the application of this waveform-based technique. If we consider a reasonable threshold (e.g. 950), where only 1 per cent of false detections are accepted, the M_c reaches values around 0.4 and 0.1 during day and night hours, respectively.

3.6 Discussion and Conclusions

The monitoring performance of a microseismic monitoring network is addressed through a robust parameter, such as M_c. However, this measure is usually esti-

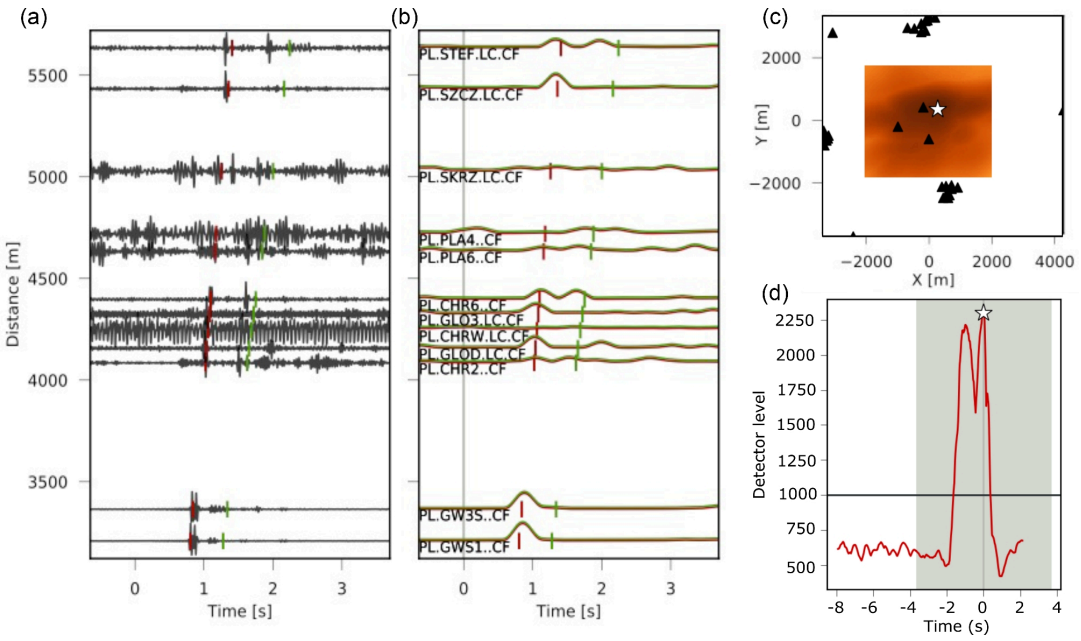

Figure 3.11: Example of synthetic event with $M_w = 0.8$. (a) Waveforms sorted by hypocentral distance for some example stations. (b) Characteristic function (normalized amplitude envelopes) for each trace. These are used for traveltime stacking corrected with P-wave speed (red lines) and S-wave speed (green lines). The markers indicate the (best-fit) synthetic arrival time of the respective phases at each sensor. (c) Coherence (stack) map for the search region. Dark colours denote high coherence values. A white star marks the location of the detected event. Sensor locations are shown with black triangles. (d) Global detector level function in a processing time window from -8 to +4 s around the origin time of the detected event. The cut-out time window used for the coherence map is shown in grey colour. White stars indicate this detection within the same processing time window, exceeding a detector level threshold of 1000.

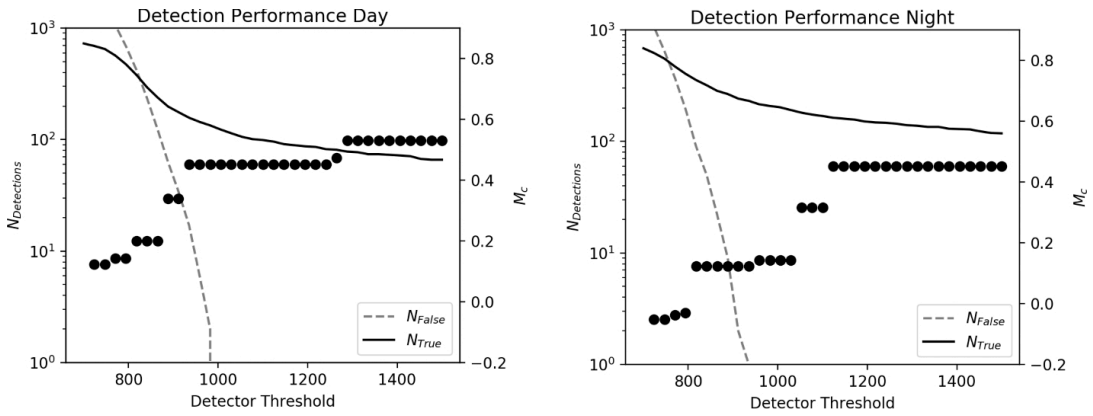

Figure 3.12: Detection performance using coherence techniques (Heimann et al., in preparation) for the synthetic catalogue with different detector thresholds. Continuous synthetic data set is generated adding real noise randomly distributed during day (left) and night (right) hours. The number of real detections corresponding with the synthetic catalogue (black line) and the number of false detections (grey dashed line) are shown. Black dots represent the values of magnitude of completeness for different detector threshold.

mated retroprospective, once we know the detected and located seismicity from a defined catalogue in a given region. In addition, the effects of changes in the number and type of instruments, as well as the available locations for installation, cannot be tested retroprospectively. Our approach aims to evaluate a prospective testing process that could generate induced seismicity taking as a starting point a seismic network previously designed and installed. The particular case of hydrofracking at the Wysin site is a good real example involving a combination of shallow and shallow depth monitoring. A realistic microseismic synthetic catalogue allows quantifying in terms of M_c our particular monitoring performance using noise recording before the fracking operations. Synthetic waveforms analysis could reveal important aspects about the seismicity we may record during and after fracking. Moreover, an adequate noise analysis is essential to know the current situation of our monitoring before the fracking operations starts.

An average amplitude threshold is estimated for each station from real noise recording reflecting diurnal variations that affects the detection performance. Although the lowest noise level are expected a priori in the shallow borehole stations, some surface stations are able to reach between 2 and 80 Hz similar or event better noise conditions. We used the raw synthetic seismogram to compare the maximum amplitudes of synthetic waveforms and average noise levels. The resolved detection performance can be adjusted by empirical relationships for different SNR values. This helps to extrapolate our estimations of completeness magnitude to a broader study region. We found that the detection performance is strongly varying for different day hours, with a better performance during quiet night hours. At the same time, M_c also differs for different source processes, so that tensile cracks are more difficult to detect than DC sources with the

same magnitude. This may have important consequences when coming to the interpretation of detected seismicity, since the DC background seismicity may be better detected than induced seismicity. Assuming an SNR = 2, we estimate an $M_c \sim 0.55$ around the fracking area, with an increase of 0.05 during day hours. Combining the distributed network with the application of three small-scale arrays in about 3 km distance to the boreholes, M_c can be lowered to $\sim$0.45 at the fracking region.

The application of a novel automated detection algorithm, based on the detection of coherence signals at multiple stations, even in presence of noisy records, is able to improve substantially the detection performance. An essential requirement is to choose a reasonable detector level to avoid greater number of false detections and maximize the real detections at the same time. Again, these procedures are usually applied during and after the fracking operations. However, combining synthetic events and real noise, we have been able to create realistic noise contaminated continuous seismograms, which allow to define a suitable threshold for the detector and to quantify the expected M_c. We estimate for the Lassie detector (Heimann et al., in preparation) an efficient threshold around 950 for which 1 per cent of false detections are accepted. The M_c is improved using this methodology, so that we could detect all synthetic events with M_w larger than 0.1 during night hours.

This study proposes a valuable approach to combine synthetic catalogue, synthetic waveform generation and noise recordings during a pre-operational phase, to properly prepare detection tools and to estimate their performance, prior to the beginning of geomechanical operations which may trigger or induced seismicity. The generation of realisitc synthetic data requires an accurate investigation of source parameters and local structural models. If these conditions are met, the synthetic data can be a useful tool to assess the detection performance, but can also be used to assess the performance of further seismological analysis, for example, to judge the uncertainty on location procedures, or the evaluate the potential of modeling/inversion techniques for source parameter determination. The approach can be easily adapted to other environments implying the detection and characterization of induced microseismicity.

3.7 Acknowledgments

This work is funded by the EU H2020 SHale gas Exploration and Exploitation induced Risks (SHEER) project (www.sheerproject.eu—grant agreement no. 640896). The synthetic data for this paper are available by contacting the corresponding author at jalopez@gfz-potsdam.de.

Chapter 4

Event couple spectral ratio Q method for earthquake clusters: application to North-West Bohemia

Authors:
Marius Kriegerowski (1) (kriegero@uni-potsdam.de), Simone Cesca (2), Matthias Ohrnberger (1), Torsten Dahm (1,2), Frank Krüger

Journal:
Solid Earth, 10, 317-328, 2019
https://doi.org/10.5194/se-10-317-2019

Status: Published

Affiliations:
(1) University of Potsdam, Germany
(2) Helmholtz Centre Potsdam GFZ German Research Centre for Geosciences, Germany

4.1 Abstract

We develop an amplitude spectral ratio method for event couples from clustered earthquakes to estimate seismic wave attenuation (Q^{-1}) in the source volume. The method allows to study attenuation within the source region of earthquake swarms or aftershocks at depth, independent of wave path and attenuation between source region and surface station. We exploit the high frequency slope of phase spectra using multitaper spectral estimates. The method is tested using simulated full wavefield seismograms affected by recorded noise and finite source rupture. The synthetic tests verify the approach and show that solutions are independent of focal mechanisms, but also show that seismic noise may broaden the scatter of results. We apply the event couple spectral ratio method to North-West Bohemia, Czech Republic, a region characterized by the persistent occurrence of earthquake swarms in a confined source region at mid-crustal depth. Our method indicates a strong anomaly of high attenuation in the source region of the swarm with an averaged attenuation factor of $Q_p < 100$. The application to S phases fails due to scattered P phase energy interfering with S phases. The Q_p anomaly supports the common hypothesis of highly fractured and fluid saturated rocks in the source region of the swarms in North-West Bohemia. However, high temperatures in a small volume around the swarms cannot be excluded to explain our observations.

4.2 Introduction

The intrinsic and scattering attenuation of the amplitudes of seismic waves is described by the dimensionless factor Q. The mapping of spatio-temporal changes of Q is an important step in seismology, since Q is controlled by temperature, rock porosity, fluid saturation and rock composition (Toksöz et al., 1981). Hence, this factor may help to unravel the possible causes of fluid-induced earthquakes, or thermal anomalies in crustal regions affected by magmatic intrusions. For instance, North-West Bohemia is regularly affected by earthquake swarms lasting several days or weeks with thousands of recorded events with largest magnitudes up to Ml 4.4 (Fischer et al., 2014). The causes of the repeated earthquake swarms which occur in narrow focal zones remain under debate. Relative earthquake localizations are very precise because of the high waveform quality recorded with a dense local permanent network (Bouchaala et al., 2013). Different tomography studies revealed consistent figures of the 3D velocity structures (Alexandrakis et al., 2014). The attenuation structure in the source region of the earthquake swarms is scarcely discussed. Some previous studies on whole raypath Q exist and can be used for verification and benchmarking. However, the main aim of this study is to test whether the here developed method can enhance the resolution of near source Q and therefore enable more robust conclusions on source dynamics and the role of fluids in the swarm cycle.

Several studies investigated the regional attenuation of North-West Bohemia by integrating along the full path from sources to receivers. Gaebler et al. (2015) estimated intrinsic and scattering attenuation of S waves (Q_s) by means of 14 selected events. Their frequency dependent results indicate mean $\bar{Q}_s$ of approximately 1000. A study by Michálek and Fischer (2013) investigated source parameters and inferred a station dependent, regional Q_p from P phase spectra. They estimated mean Q_p ranging between 100 and 450. They also discuss effects of directivity on Q concluding that the directivity has little influence due to the position of stations with respect to radiation patterns.
A tomographic study of North-West Bohemia done by Mousavi et al. (2017) indicated a regional average attenuation of approximately $Q_p \approx 100$ to $Q_p \approx 300$ and a pronounced highly attenuative source region where $Q_p < 100$.
Bachura and Fischer (2016) employed two different methods to resolve the regional coda Q_c from the source volume to receivers. They used 13 selected events of the 2011 swarm and found a variation of Q_c between 100 and 2500 within the exploited frequency range of 1-18 Hz.
A recent work by Wcisło et al. (2018) used a newly developed differential attenuation estimation technique focused on the source region. The authors employed the peak frequency method which relates the half-period of P pulses to attenuation. They also used a differential approach to map the inter-event attenuation using a single station (NKC) and found $Q_p \approx 120$ and $Q_s \approx 80$ in the source region.
Most previous Q studies focusing on NW Bohemia were inherently of low spatial resolution. Firstly, either because Q was estimated for the integral ray path between sources and stations (except for the work by Wcisło et al. (2018)) or secondly, because they focused on low frequencies, or both. E.g. Mousavi et al. (2017) used frequencies between 1 to 30 Hz and Gaebler et al. (2015) up to 32 Hz.
In this study, we aim to increase the spatial resolution and to resolve Q for waves traveling only within the small source region of the earthquake swarms. The developed event couple spectral ratio method is based on the assumption of an exponentially decreasing spectral slope at high frequencies ω above the corner frequency of the earthquake, often referred to as the ω^2 model (Aki, 1980). From the ratio of the spectral slopes of two events one can estimate the attenuation of P and S phases for the ray path between the two events, given the differential travel time of both events. Matsumoto et al. (2009) exploit amplitude spectral ratios of direct P phases and normalize the spectra with the coda energy to compensate for source effects. Opposed to their approach we focus on the higher frequency content to achieve a higher resolution needed to map the compact source volume.
The spatially compact seismic clusters in NW Bohemia provide us with a favorable case study scenario due to the high similarity of source characteristics (Michálek and Fischer, 2013). We test our method on data recorded from October 6 until October 13, 2008 and a double-difference relocated event catalog of 3841 events with local magnitudes between -0.9 and 3.5 (Fischer and Michálek,

2008). The high density of events during earthquake swarms clustering within a small and confined region allows to infer the local attenuation from event couples, by applying the spectral ratio method (Aki, 1980) to their high frequency amplitude spectra as we will explain in the following section. One major issue when calculating spectral content of very few data samples is spectral leakage, as a result of the finiteness of the time window under study. In order overcome this problem Thomson (1982) proposed the multitaper method, which we employ using *mtspec* (Prieto et al., 2009; Krischer, 2016).

4.3 Method

A velocity spectrum $A(\omega)$ of a direct body wave phase originating from a source j recorded at a station i can be described as (Sanders, 1993):

$$A_{i,j}(\omega) = S_j(\omega)I_i(\omega)R_i(\omega)G_{i,j} \cdot e^{\frac{-\omega t^*_{i,j}}{2}} \tag{4.1}$$

where ω is the angular frequency. $S_j(\omega)$ describes the source spectrum and $I_i(\omega)$ the instrument response. $R_i(\omega)$ is the receiver site effect. $G_{i,j}$ is the frequency independent geometric loss. The exponential term depends on the angular frequency ω and t^*, the path integrated attenuation from the source to the receiver:

$$t^* = \int Q^{-1}/v ds \tag{4.2}$$

with Q as the dimensionless quality factor, velocity v of the medium and ds a segment along the ray path from the source to the receiver. Attenuation is considered here as a combination of intrinsic and scattering losses. Instead of estimating a total t^* describing the full ray path's attenuation we estimate a local t^* from velocity spectra of two earthquakes sharing the greater part of their ray paths from the seismogenic zone to a receiver. Site effects as well as the receivers response functions cancel out when two spectra recorded at the same site are analyzed by means of amplitude ratios. Let $A_{j,0}$ and $A_{j,1}$ be two velocity amplitude spectra of events E_0 and E_1 (in the following referred to as *first* and *second* event of a couple) recorded at a station j (Figure 4.1). We assume that their source spectra $S_0(\omega)$ and $S_1(\omega)$ resemble each other to a degree where the effect of random perturbations at high frequencies average out when the proposed method is applied to many couples. Taking the natural logarithm of the spectral ratio of $A_{i,0}$ and $A_{i,1}$ yields:

$$ln(A_{i,0}(\omega)/A_{i,1}(\omega)) = ln(\frac{G_{i,0}}{G_{i,1}}) - \omega\delta t^*/2 \tag{4.3}$$

with

$$\delta t^* = t^*_{i,0} - t^*_{i,1} \tag{4.4}$$

This equation describes a linear relation with frequency independent geometrical losses to the left of the negative sign in equation 4.3. The slope k of a line

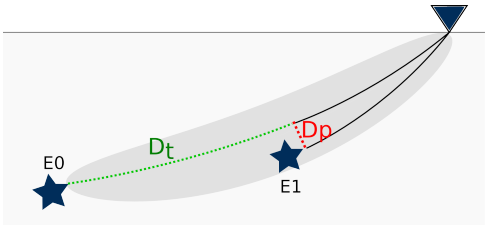

Figure 4.1: Schematic illustration of the geometrical constraints and the employed parameters. The triangle represents a recording station at the surface. Attenuation is estimated for the traversing distance ray path segment (D_t, green dashed line). Geometrical constraints respect the passing distance (D_p). Grey shaded area illustrates the Fresnel volume of the first event.

fitted to equation 4.3 can be used to derive the attenuation time t^* in between the two sources from which Q^{-1} can easily be inferred using equation 4.2.
The far field amplitude spectrum $A(\omega)$ of P and S phases can be parameterized as follows: a seismic moment dependent low frequency plateau, the corner frequency f_c and the high-frequency spectral decay approximately proportional to ω^2 resulting from finiteness of particle rise time and the rupture duration (Aki and Richards, 2002). To remove the dependence on seismic moment we investigate the high-frequency spectral decay, only. Furthermore, exploiting spectral content above the corner frequency also reduces source directivity effects on attenuation estimates (Cormier, 1982).
We infer the corner frequency based on previous studies on NW Bohemia seismic swarms. We use a relation proposed by Michálek and Fischer (2013) to calculate source radii r based on the moment M_0 of an event:

$$r = 0.155 \cdot M_0^{0.206} \tag{4.5}$$

where $M_0 = 1.38M_L + 10.3$. The resulting source radii r are then converted to f_c using

$$f_c = k\beta/r \tag{4.6}$$

with $k = 0.32$ (Madariaga, 1976), and $\beta = 3.5$ km/s, which is a reasonable assumption for the source region (Michálek and Fischer, 2013). We increase the lower frequency limit (f_{min}) used for our spectral analysis by additional 5 Hz with respect to f_c to account for uncertainties in M_0 and to ensure linearity of the high frequency decay. This approach allows frequency bands being wide enough for employing a stable linear regression. The upper frequency limit f_{max} was chosen dependent on the Fresnel volume (see below) of a couple's first event (Figure 4.1) and the upper corner frequency of the anti-alias filter of the recording equipment which is approximately 85 Hz. We calculate the power spectral density using the multitaper spectral analysis method (MTM) (Thomson, 1982; Park et al., 1987). With this method the time series is multiplied with several orthogonal slepian tapers which are resistant to spectral leakage. The power spectral density is then reconstructed after Fourier transformation of the tapered samples and a

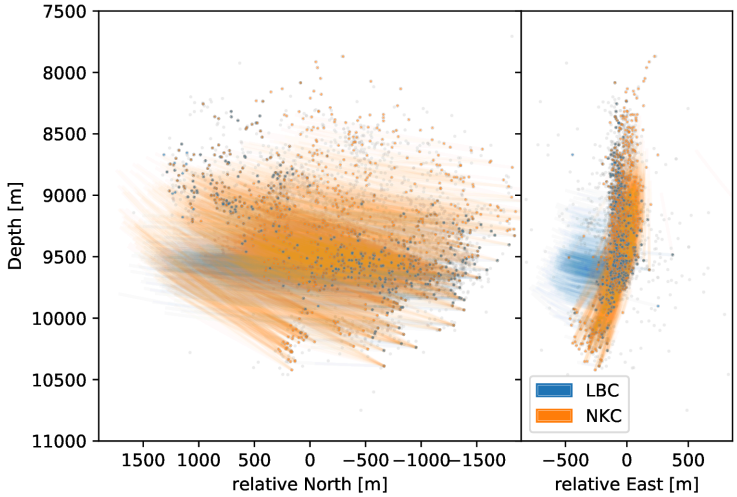

Figure 4.2: Ray segments with respect to stations *LBC* and *NKC*. Source region seen from West (left) and from South (right). The colors indicate the station at which the displayed ray segment arrived as well as the underlying source of the segments. Grey points show hypocenters which occurred during the investigated time interval but were not attributed to an event couple.

weighted summation of the resulting spectra. A more exhaustive explanation can be found in Park et al. (1987). The applied code is a *Python* wrapper to the *Fortran* routine *MTSpec* (Prieto et al., 2009; Krischer, 2016). *MTM* achieves stable spectral estimates also for very short time windows. A critical parameter of the *MTM* is the number of slepian tapers as it balances the smoothness and precision of spectral estimates. We use the implemented default, which is

$$N_{tapers} = int(bw \cdot 2) - 1 \tag{4.7}$$

where bw is the *bandwidth_factor* which we set to $bw = 4$. Lower values prove to increase the number of outliers due to increased spectral leakage. Higher values did not change the results significantly but are more expensive to compute.
We impose strong geometrical constraints to select event couples with respect to a station as sketched in Figure 4.1. Ray tracing is done based on a 1D velocity model suggested by Alexandrakis et al. (2014) for the seismogenic region combined with a regional crustal model proposed by Málek et al. (2000) (Fig. 4.4, left panel). The first geometrical constraint is the traversing distance (D_t, green dashed line, Fig 4.1) between an event E_0 with respect to perpendicular projections of other hypocenters onto that path. The second constraint is the passing distance (D_p, red dashed line in Fig 4.1) of that projection of E_1 onto the ray between E_0 and the station. We defined a minimum traversing distance of $D_t \geq 1500$ m to ensure that the signal of the second event is attenuated sufficiently to be detectable in the couple's spectral ratio.
Subsequent to geometrical preselection upper frequency limits of the analyzed bandwidth are potentially corrected to lower values dependent on the 2nd Fresnel volume in between event E_0 and a station. The wavelength from which this

frequency limit can be deduced is given as (Matsumoto et al., 2009):

$$\lambda = D_p^2 \frac{D_t + x}{D_p x n} \tag{4.8}$$

D_p and D_t are passing distance and the traversing distance as defined above. x is the distance from the passing point with respect to the second event E_1 to the receiver (Figure 4.1). n is the number of the Fresnel volume. The frequency limit can then be deduced from the wavelength and the wave velocity of the underlying medium. This approach provides a physically meaningful limitation to impose on the frequency bandwidth. It ensures that E_1 is located within the Fresnel volume (grey shaded area in Figure 4.1) for the entire analyzed frequency band.
With this approach we get an estimate for the attenuation along the traversing distance (green dashed line in Figure 4.1) and when repeated for a large number of event couples can retrieve a median attenuation for the entire source region. The described method is advantageous over other methods which require handcrafted features like onset duration picking as it can be automatized given that an onset catalog is at hand.

4.4 Synthetic Study

In order to evaluate the expected number of exploitable couples given the geometrical constraints we calculate the relative number of pairs at discrete surface points covering the region of North-West Bohemia. The size of the blue points in Figure 4.3 represents the relative number of arriving shared ray paths from event pairs at possible station sites based on ray tracing through a 1D layered model (Fig. 4.4). Largest numbers of pairs are expected along a North-South striking patch which follows the striking direction of the main fault plane. However, in this case study we use only those stations which provide continuous recordings for the investigated time span. These are stations *KRC*, *LBC*, *NKC*, *SKC* and *VAC*. After geometrical filtering we expect stations *NKC* and *LBC* to produce the highest number of couples since they provide continuous recordings for the entire time period and are in a favorable lateral location. Most other stations are located where no or a negligible number of event pairs are expected. Figure 4.2 shows the rays which penetrate the source volume and fulfill the geometrical requirements described above. It shows that for events recorded at the most significant stations *NKC* and *LBC* the highest ray density and therefore sensitivity is in the lower half of the seismogenic zone. This bias is more pronounced for recordings at station *LBC*. Also, these ray segments sample the volume up to approximately 500 m to the West of the seismic swarm.
We use synthetic waveforms calculated using reflectivity method (Wang, 1999) employing the same 1D velocity model as for ray tracing (Figure 4.4). The model simplifies the true conditions and therefore produces comparably clear phase onsets. However, the recorded data are also dominated by relatively little

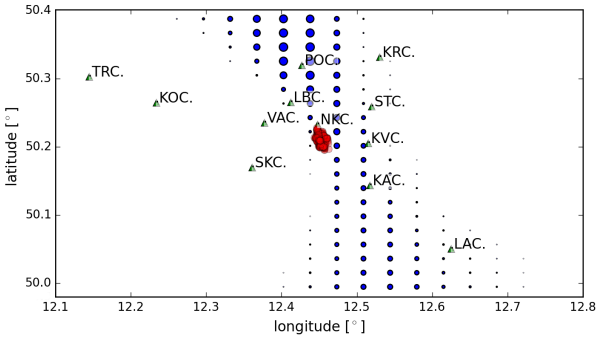

Figure 4.3: Mapping potential locations of future seismic stations favorable to resolve Q using the described method. The size of the blue points for each tested location represents the relative number of arriving shared ray paths from event couples. Red dots show the seismicity of the investigated swarm. Green triangles indicate locations of the WEBNET stations.

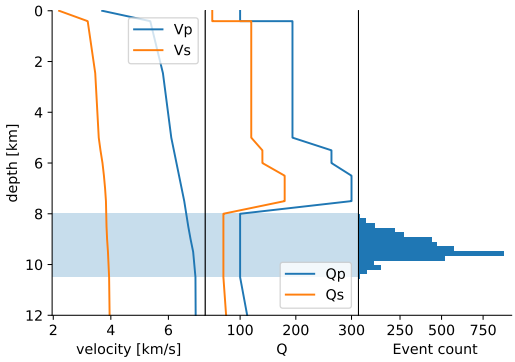

Figure 4.4: Synthetic velocity and attenuation model used for validation of the method. The seismogenic zone is marked by light blue. The attenuation in that zone is expected to be decreased with respect to the regional attenuation model.

scattering and sharp onsets (Fischer et al., 2010). The effects of scattering on the final results will be discussed in greater detail in sections 5.
Hypocentral locations and origin times are taken from the double difference relocated catalog of Fischer and Michálek (2008). All synthetic sources are double couple sources with mean strike, dip and rake set to 170 ± 10, 80 ± 10 and -30 ± 10 degrees, respectively, uniformly distributed in all three domains. The mean strike, dip and rake values are the predominant source types stated by Fischer et al. (2014) which were retrieved based on polarity analysis of P phases. The seismogenic zone (depth 8500 m - 10500 m in Figure 4.4) has a Q_p of 100 and Q_s of 50. It is overlain by a more complex attenuation structure, characterized by higher Q values.
In order to mimic uncertainties in origin times, locations and velocity model travel times are perturbed by 10 ms, uniformly distributed. The uncertainties of

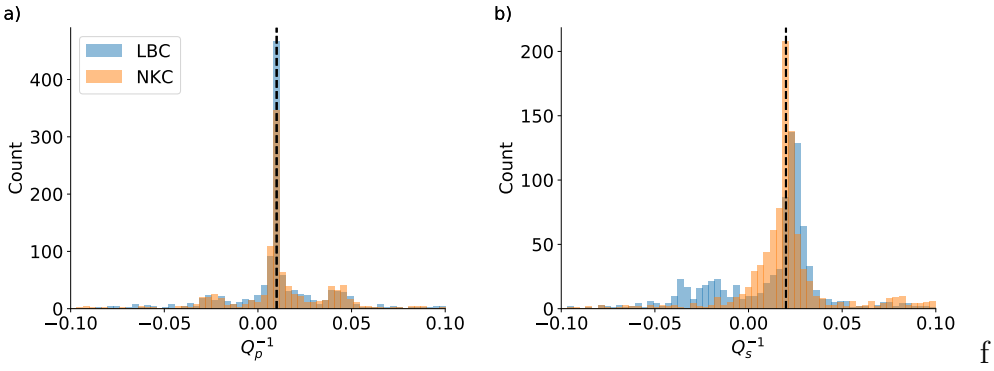

Figure 4.5: Synthetic tests targeting $Q_p = 100$ (a) and $Q_s = 50$ (b) with noise free data. No source time functions have been convolved. The correct values for Q_p and Q_s are indicated by the vertical dashed lines. The station color coding as given in the legend is used consistently throughout all following images.

the velocity model have an effect only in the source region since both rays of a couple traverse through the same overlaying velocity model.
The window length was 0.15 s for P and 0.3 s for S phases. The minimum allowed cross correlation of event couples in synthetic tests and later application to real data was set to 0.75. Signal-to-noise ratio (SNR) of a phase under consideration compared against a noise sample preceding the P phase has to be larger than 5 across the entire selected frequency band (after slight spectral smoothing to reduce effects of spectral notches). These two requirements efficiently reject outliers. The minimum allowed bandwidth is 10 Hz, which excludes all events with magnitudes of less than 0.5, given the magnitude dependent lower frequency limit ($f_{min} = f_c + 5.0Hz$, where f_c is calculated using equation 4.6). The bandwidth threshold stabilizes the linear fit to the spectral ratio as it limits the minimum number of data points. We evaluate Q_p from vertical channels and Q_s on North-South and East-West components and average results for each couple.
Data availability of the recorded dataset has been accounted for. Synthetic traces were only produced for an event if the recorded dataset contains data as well. All synthetic traces where convolved with the transfer functions of the WEBNET stations to generate realistic velocity traces.

Figure 4.5 shows distributions of retrieved Q^{-1} estimates from all event couples of the synthetic test using noise-free traces. In this as well as in the following test depicted in Figure 4.6 traces have not been convolved with a source time function (i.e. they have impulsive source durations). The resulting distributions show some scattering solutions. Peaks in both cases (Q_p and Q_s) resemble the targeted attenuation model (dashed, vertical line).
The next test depicted in Fig. 4.6 includes additive recorded noise. Data windows without seismic events in the field recorded data have been manually extracted and randomly added to synthetic traces to mimic realistic noise conditions. P phase results show a broadening of the distributions at all stations. While the

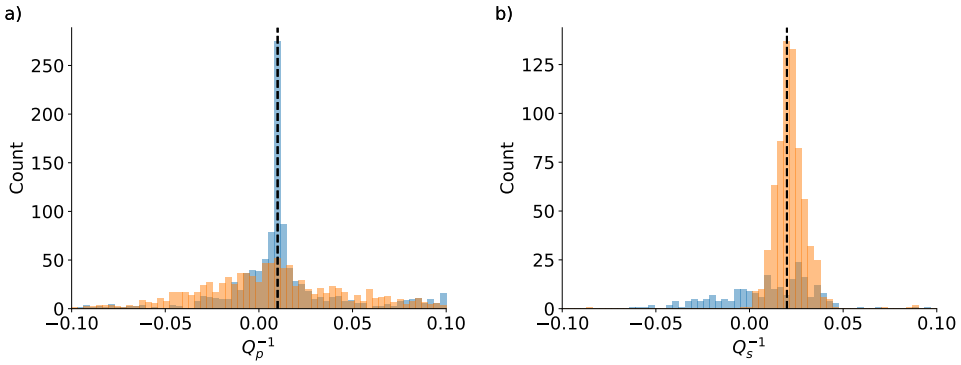

Figure 4.6: Synthetic tests with the same setup as in Figure 4.5 but with additive real recorded noise from analyzed stations. Again, traces have not been convolved with a source time function.

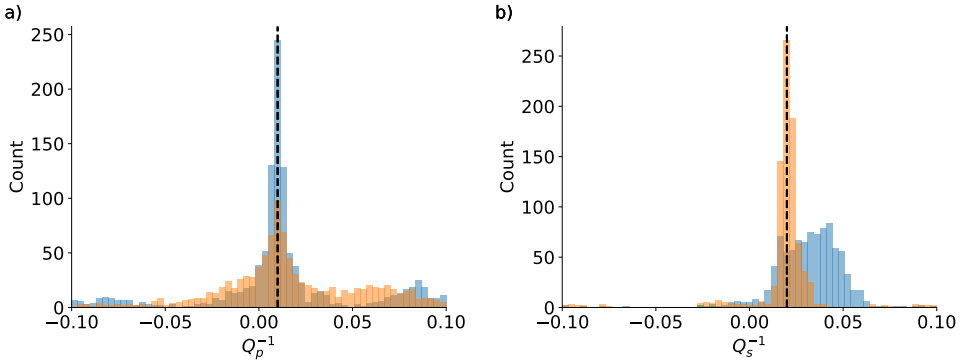

Figure 4.7: Synthetic tests with the same setup as in Figure 4.6. Synthetic traces were convolved with magnitude-dependent synthetic source time functions.

distribution of station *LBC* still centers around the model value, the results of station *NKC* show only weak correlation with the correct model. This is a result of the location of station *NKC* close to the nodal plane of the dominant rupturing plane where smallest signal amplitudes are expected. *S* phase results match the model at *NKC* but show strong scattering at *LBC* as a result of the interference with the added noise as well as the *P* phase coda.
In a next step (Fig. 4.7) we convolve synthetic Greens functions with realistic magnitude dependent source time functions. The applied source time function is half sine shaped where the slope of the high frequency spectral roll off is not dependent on the width of the applied pulse as can be seen in Figure 4.8 where normalized synthetic source spectra are depicted for different relative pulse widths. The vertical position of the spectral envelope changes with changing duration but the slope remains the same for all depicted factorized pulse widths. Other than expected, this stabilizes results. This is a result of the pulse broadening which leads to a stabilization of *MTM* estimates as onsets become less transient. The performed synthetic tests cannot reproduce waveforms in its full natural

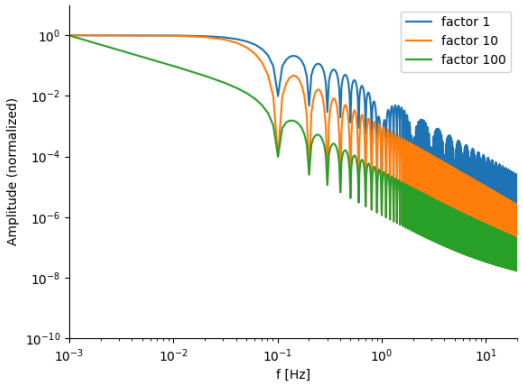

Figure 4.8: Normalized synthetic amplitude spectra of applied source time functions with different durations as a factor relative to the blue one (factor=1). The slope of the high frequency spectral roll-off is identical.

complexity. Nevertheless, they prove that the concept is capable to estimate attenuation of the anticipated region.

4.5 Application to North West Bohemia

North-West Bohemia is a favorable case for testing our approach. Several focal mechanism studies on earthquake swarms in this region indicate dominant principle faults striking at 169° and 304° (Vavryčuk, 2011), which have been active in different seismic sequences. Events occurring during a swarm tend to rupture on the same fault. This observation in combination with compactness of seismic clusters (Figure 4.10) explains the high similarity of waveforms observed for each swarm. We therefore also assume that source characteristics including rupture directivity effects are similar throughout each swarm cycle.
By the time of the 2008 swarm the WEBNET stations were equipped with three component short period seismometers, except for station *NKC* located in the epicentral area which is a broad band station. All waveforms are sampled at 250 Hz. An example of a P phase onset recorded at station *LBC* is shown in Figure 4.9 together with the estimated amplitude spectra. A manual revision of all event waveforms has been done to remove those which show indications of event doublets happening shortly after each other but not being indicated as such in the catalog. Spurious signal leftovers of a preceding event not necessarily cause high distortion of the fundamental P phase waveform and may thus not be removed by setting a cross correlation threshold. However, their effect lead to distortion at high frequencies of phase spectra and significantly increase the number of outliers during the analysis. The catalog of *HypoDD* (Waldhauser and Ellsworth, 2000) relocated events is comprised of 3841 events and their associated P and S phase picks. When applied to station *LBC*, a total of 641 couples were used which fulfill the requirements in terms of SNR, cross-correlation and

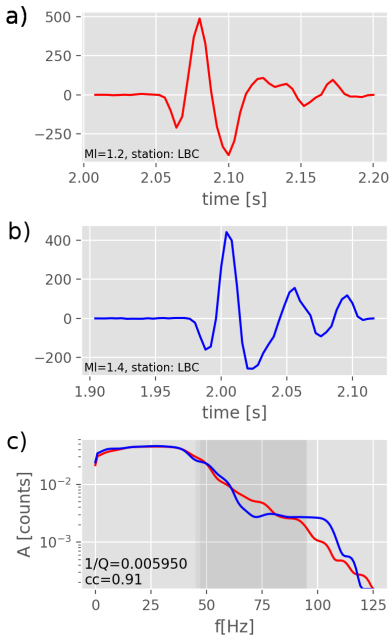

Figure 4.9: Two P phase wavelets recorded at station LBC and their spectra from events with local magnitudes Ml=1.2 and Ml=1.4. First two panels show a) first and b) second event of the analyzed event couple. The grey shaded area in c) indicates the used frequency band. The cross-correlation coefficient is 0.91 and the attenuation was in this case estimated as $Q^{-1} \approx 0.006$

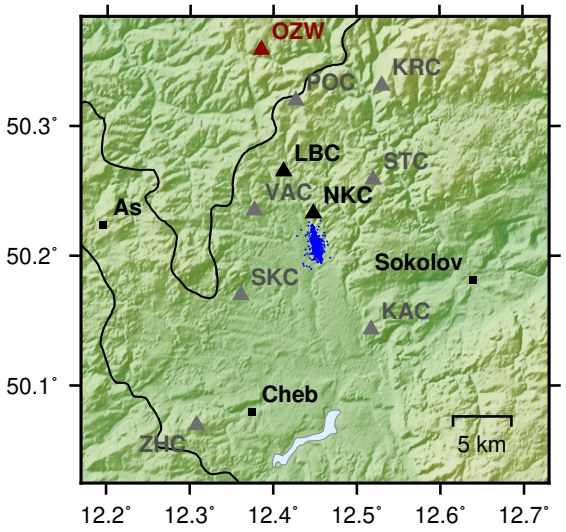

Figure 4.10: WEBNET stations (triangles) and seismicity (blue circles) which occurred in North-West Bohemia during the investigated time period. Red triangle: temporary station installed by University of Potsdam in October, 2017. Stations in Nový Kostel (*NKC*) and Luby (*LBC*) are highlighted. All other stations produce no or insignificant number of data points.

geometrical constraints. Results of P phases evaluated at station *LBC* (Fig. 4.11, left) have a median $\bar{Q}_p^{-1} = 0.019$, equivalent to $\bar{Q}_p = 53$. The distribution shows some negative results which do not have a physical meaning and are related to noise in spectral estimates. Results retrieved based on data from station *NKC* are significantly more unstable, as Figure 4.11 (left) indicates. The distribution shows a large number of negative results. The median attenuation is $\bar{Q}_p^{-1} = 0.001$, equivalent to $\bar{Q}_p = 1000$. 1404 couples where used in this case. Attenuation evaluated for S phases show almost zero centered distributions at both stations *NKC* and *LBC* which in turn means significant number of negative and therefore unphysical measures. Median attenuation values are $\bar{Q}_s{}^{-1} = 0.0023$

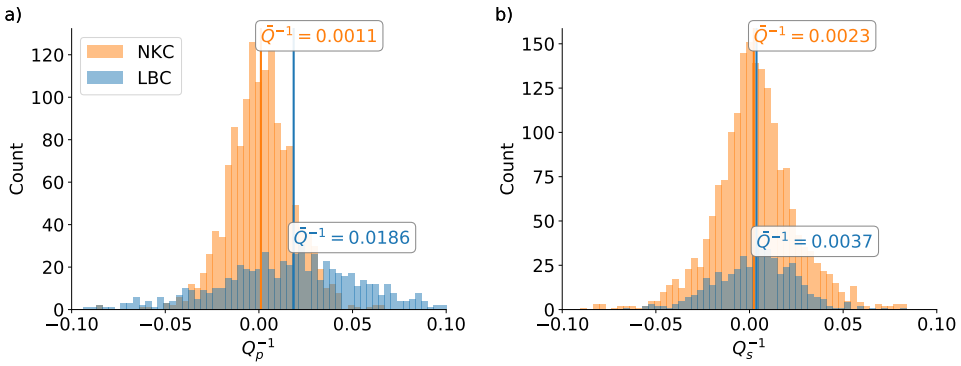

Figure 4.11: Attenuation results at stations *LBC* and *NKC* for Q_p (a) and Q_s (b). Median values are indicated by the overlined Q.

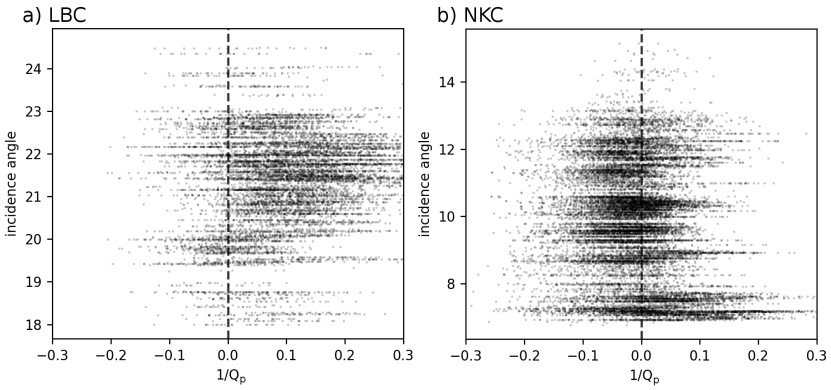

Figure 4.12: Incidence angles plotted against Q_p^{-1} of rays originating from event couples recorded at station *LBC* (left) and *NKC* (right). $Q_p^{-1} = 0$ is highlighted with a dashed line.

($\bar{Q}_s = 435$) at station *NKC* and $Q_s^{-1} = 0.0037$ ($\bar{Q}_s = 270$) at stations *LBC*, respectively. Both values are comparably large compared to Q_p estimates from station *LBC*. A bias of these S phase attenuation measures is introduced by the P phase coda energy interfering with S phases and therefore distorting the anticipated high frequency content.

In order to achieve a better understanding of the method's breakdown for P phase recordings of station *NKC* we disable the cross correlation threshold and scrutinize Q^{-1} against a multitude of parameters for station *NKC* and *LBC*. Figure 4.12 shows incidence angles of rays of event couples on the y- and Q^{-1} on the x-axis. Incidence angles are estimated using a 1D raytracing algorithm (Heimann et al., 2017). By definition the incidence angle is almost identical for both events of a couple. It becomes evident from figure 4.12, b) that larger incidence angles (> 8 degrees) show a tendency at station *NKC* to produce negative Q^{-1} while results from events with steep incidence angles produce positive Q^{-1} values. When compared to the same kind of plots for station *LBC* no such trend is evident.

Station *NKC* is located at the northern edge of the swarm's epicentral region. Hence, incidence angle approximately correlates with latitude, indicating a location dependent problem. The depth sections of results from stations *LBC* and *NKC* (Figure 4.13) show again that the attenuation is mostly positive (red) at station *LBC* (Fig. 4.13, a) and c)) in accordance with Figure 4.11. The distribution of attenuation at station *NKC* (Fig. 4.13, b) and d)) indicates a trend of decreasing Q^{-1} values from North to South. This supports the hypothesis of a location dependent issue. Figure 4.13 d) shows accumulated positive results related to first events at 1.4 to 2.0 km North (x-axis) which coincides with the position of a small sub-cluster seen in Figure 4.13 b) below a depth of 9.8 km. From 1.2 to 1.4 km North the event couple distribution becomes more sparse. The separation of positive attenuation in the North and mostly negative attenuation in the South of that gap implies a systematic change in frequency content from two separated segments of the swarm occurring along raypaths from the

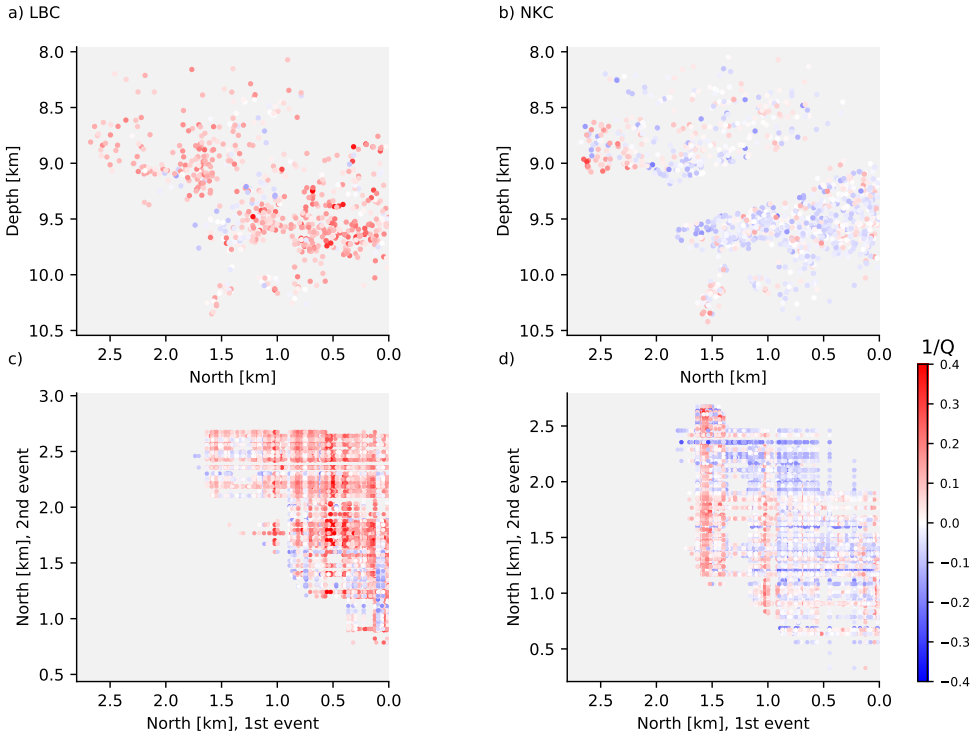

Figure 4.13: Spatial distributions of attenuation at station *LBC* (left) and *NKC* (right). The source region is depicted as seen from the West. The origin of the coordinate system corresponds to the southernmost event. Panels a) and b) show average color coded attenuation results of each used event. Panels c) and d) show the attenuation for each single event pair. First (deeper) events of each couple are represented by the x-axes whereas second events of each couple are represented by the y-axis. Attenuation at station *LBC* is mostly positive. Sub-horizontal seismicity gaps in panels a) and b) are caused by the set minimum distance (D_t) between two events.

source region to station *NKC*.

Figure 4.14 shows *P* phase waveforms of first events of couples recorded at station *NKC* and *LBC*, filtered between 1 and 30 Hz for events northern (Fig. 4.14, left panels) and southern (Fig. 4.14, right panels) of the aforementioned gap. While the used filter frequencies are actually below the exploited frequency band used in the analysis these waveforms demonstrate that the waveform complexity is significantly higher for events recorded at station *NKC* than for those recorded at station *LBC* indicating that scattering plays a major role along the ray paths to station *NKC*. The average shape of the waveforms following the first onset pulse differ in the northern and the southern sections. Furthermore, there are *P* phases with flipped polarities which indicates that station NKC was situated closer to the nodal plane than station *LBC*. This aspect is in accordance with

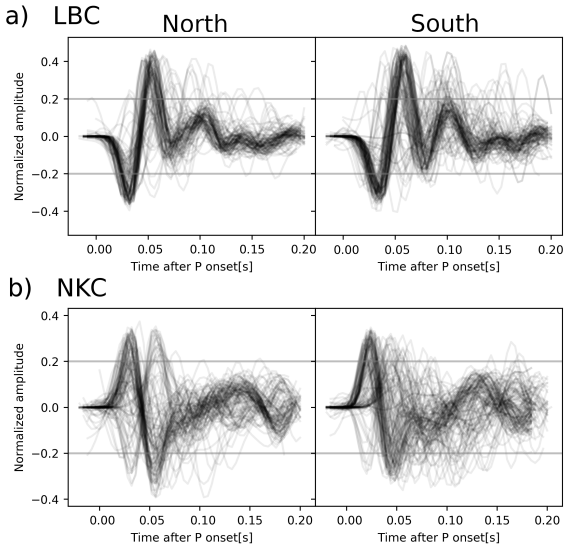

Figure 4.14: P phase onsets of couples' first events in the northern and the southern part of the swarm area. Panel a) shows recordings at station LBC, b) recordings at station NKC.

synthetic tests in chapter III which show worse performance of station NKC then station LBC for P phase measures.

4.6 Interpretation and Discussion

We present a newly developed method to estimate attenuation from spectral ratios of event couples. The short analyzed time windows are prone to spectral leakage which we mitigate by applying the multitaper approach. However, this method can only suppress leakage caused by windowing effects. Leakage from source effects such as finiteness of the slip and the rupture are not smoothed as they are expected source characteristics and not filter artifacts.
The given geometry and available data limit the perceptive field of the applied method mostly to the lower half of the seismic swarm (Fig. 4.2). Rays arriving at station LBC show a worse penetration of the focal zone compared to those arriving at station NKC (Fig. 4.2) where the takeoff angle is almost perpendicular to the normal orientation of the main rupturing fault. Therefore, the setting of sources with respect to station NKC is favorable from a geometrical point of view as it can be considered to have a higher sensitivity for attenuation in the source volume.
Synthetic tests show that the method is capable to reproduce average source volume attenuation of $Q_p = 100$ and $Q_s = 50$ given the 2008 earthquake swarm hypocentral locations. In noise free condition a precise result can be achieved for both, P and S phases at both significant stations NKC and LBC. With additive recorded noise, the distribution of Q_P results broadens but still resembles the true attenuation with high precision at station LBC. Synthetic waveforms at sta-

tion *NKC* suffer from weaker *SNR* at high frequencies indicating that the applied *SNR*-threshold of 5 is too optimistic. However, reducing this value would also reduce the number of data points and therefore have a negative impact on the statistical significance of results. Q_s results at station *NKC* are more robust then at station *LBC*. Both measures, Q_s and Q_p, improve when convolving synthetic waveforms with synthetic source time functions as this stabilizes the multitaper spectral estimates.
The application to recorded P phase onsets shows fewer negative Q_p results at station *LBC* and than at station *NKC* which results in a distribution with a clearer offset with respect to $Q_p = 0$. Waveforms recorded at station *LBC* are significantly higher correlated than those at station *NKC* where changing waveform polarities and high waveform complexity can be observed. We hypothesize that rays arriving at *NKC* experienced relatively stronger scattering or that a nearby reflector creates multiples which interfere with signals recorded at *NKC*. In the latter case, the reflector would have to be situated in a location where interactions with signals arriving at *LBC* are weaker. Mousavi et al. (2017) assume a highly fractured medium in combination with accumulated free gas or fluids which would cause a high attenuation in the source region and could therefore explain our observations on low Q_p. A 3D V_p/V_s tomography by Alexandrakis et al. (2014) identified a low V_P/V_S ratio body directly overlaying the focal zone. The increased waveform complexity seen at station *NKC* can be a result of waveform interaction with that body. The effects do not necessarily have an influence on results at station *LBC* where rays have different paths and take off angles.
Another influence may be rooted in the different families of focal mechanisms. Vavryčuk et al. (2013) reported three different families of focal mechanisms for the 2008 swarm. While the slope of high frequency spectra should not directly be affected by the radiation pattern, there can be higher order effects like rupture propagation and rupture complexity. Dependent on the take off angle these rupture dynamics can affect the high frequency spectral roll off and therefore map into attenuation estimates (Kaneko and Shearer, 2015). P phase polarity changes at station *NKC* indicate that the station is located close to the nodal plane of the main rupturing fault. This circumstance can increase the effect of the aforementioned effects seen at station *NKC*. If they differ systematically in the lower and upper source region, this can lead to biases in attenuation analysis due to the heterogeneous sensitivity across the fault plane. Still, we do not see such effects at station *LBC* and therefore speculate, that the dominating effect is the differing raypaths or a combination of both, raypath scattering and rupture dynamics.
Our findings in terms of P wave attenuation based on data from station *LBC* show similarly low values compared to results by Wcisło et al. (2018) who obtained $Q_p \approx 120$ for the source regions. Previous studies by Michálek and Fischer (2013) investigated source characteristics in NW Bohemia and suggested station dependent whole path integrated mean Q_P values ranging between 100 and 450. We find lower values which can be a result of hydration of the seismogenic zone. Haberland and Rietbrock (2001) also report highly increased attenuation

($Q < 100$) within earthquake cluster regions and postulated that this could be related to hydration or partial melting. For instance, melt migration has been postulated from the size and migration pattern of earthquakes of the 2000 earthquake swarm (Dahm et al., 2009). On the other hand, Alexandrakis et al. (2014) interpret their results on velocity variations by dehydration processes. Our results deduced from station *LBC* for average attenuation are in line with previous findings pointing to high attenuation in the source volume.
Frequency bandwidth is a critical parameter which is limited mostly by the corner frequency of the recording setup and signal to noise ratio at high frequencies. Future plans of the Intercontinental Drilling Project (ICDP) include the installation of up to 4 borehole seismometers in NW Bohemia. It can be expected that our method will benefit from these measurements. Improved signal to noise ratios allow to sample and exploit information at higher frequencies which will stabilize the spectral estimate. Furthermore, higher sampling rates allow a better temporal (and therefore spectral) resolution of P and S phases. This will, in turn, also allow to use even shorter time windows. For the method discussed here, it would be favorable if at least one of these borehole stations will be situated in a location where a high number of ray path sharing couples can be found. The most sensitive region follows the NNE - SSW striking of the fault and concentrates in the North of the earthquake swarm (Fig. 4.3).
In late September 2017 the University of Potsdam installed a short period seismometer close to the Czech-German border in Oberzwota (red triangle, map 4.10) which is a favorable location. The station recorded 1000 samples per seconds for 62 days during a period of relative quiescence. Nevertheless, approximately 30 events were recorded in the swarm area with local magnitudes down to Ml=0. Despite the installation directly on top of the weathering layer the recordings showed signal to noise ratios larger than 5 at 120 Hz and above for smallest magnitudes. It becomes evident that even a surface mounted station would allow to harness spectral information above the corner frequency of the WEBNET stations also for smallest magnitudes and which indicates that this will improve the resolution and robustness of our method once the ICDP borehole installations are operating.

4.7 Conclusion

Applying the source couple amplitude spectral ratio method to differential phase measures is an alternative to methods which commonly exploit the lower frequency ranges. Theoretically, it is therefore able to achieve better resolution. Our synthetic study validates this. The geometrical constraints of this method require a high density of events as it is the case for natural earthquake swarms or seismic nests but also for hydrofracturing experiments.
The application to data from the 2008 North West Bohemia earthquake swarm indicates source region $Q_p < 100$ based on data recorded at station *LBC*. The sensitive region measures only approximately $2000 * 500 * 500$ meters in North,

East and West direction (Fig. 4.2). Results can therefore be considered of high spatial resolution. Nevertheless, the distribution of solutions significantly scatter and we see room for improvement e.g. through high frequency borehole recordings. We are not able to retrieve stable estimates at station *NKC* but instead see negative attenuation in southern and positive attenuation in the northern section of the swarm. *P* phase waveforms of the two sections show systematic differences at both significant stations which indicates a North-South structural difference. Furthermore, this effect does not inflict on measures at station *LBC*. Given the fact that ray segments at *NKC* and *LBC* probe two different but directly neighboring media leads us to the conclusion that the fractured medium is highly concentrated along the source patch and that the surrounding medium can be considered much more dense or intact.

acknowledgements

This work is part of the HISS project which is funded by the DFG ICDP. Project no.: CE 223/2-2. We would like to thank Tomas Fischer and one anonymous reviewer as well as the editors for their valuable comments.

Chapter 5

Conclusions

The intent of this thesis was to develop efficient fully or semi automated full waveform methods that enhance our understanding of earthquake swarm dynamics which are found in a natural form e.g. in NW Bohemia.
Seismicity rates of swarm areas can be very high resulting in large catalogs of tens of thousands and more events. Since manual phase picking and event-by-event analysis is not feasible in these situations automated routines are required to extract the maximum possible amount of information from large data sets in reasonable time. In Chapter 2 I developed and evaluated a novel deep learning based approach to detect and locate events. It allows to locate approximately 1000 events in less than 1 second using full waveforms. For comparison let us assume that picking of S and P phases on 12 stations may take approximately one minute per event assuming an experienced operator and neglecting the fact that picking and locating can be an iterative procedure. The total time would therefore sum up to 1000 minutes to pick 1000 events, corresponding to 60000 seconds or 16.7 hours in addition to setting up the location algorithm. Hence, it can be concluded that the novel approach is approximately 60000 times faster than a standard, pick based location approach and offers a high potential for automation. 88 % and 69 % of predicted locations deviate by less then 200 and 100 meters from the double difference relocated evaluation catalog, respectively. The high efficiency of this technique when predicting hypocenter locations based on full waveforms addresses the demand for modern techniques that are capable of processing current large and future largest seismological datasets. The applied method is suitable to locate earthquakes not only as a standard analysis tool on large databases but can also be applied on real time data. Thanks to the rapid pace of processing the method could be applied (after some modification as described in the following Chapter) e.g. also in the field of earthquake early warning where fast real time analysis of large numbers of full waveform data streams is necessary. Despite the good performance opposed to full waveform localization methods based on handcrafted features (e.g Grigoli et al., 2016) the current implementation of deep learning event localization is failing as soon as two events interfere – a drawback given that swarm activity is defined by a high occurrence rate of events in a short period of time which implies that events can

also overlap. Furthermore, a disadvantage of the deep learning based event localization as implemented in Chapter 2 is that the station geometry is not flexible as the network is trained to data for that specific geometrical setting.
A further novelty presented in Chapter 2 is the ability to detect earthquakes based on the first layer's activation functions. Conceptually this feature can be described as a pattern matching technique as the data is convolved with the trained filters of the first layer - the patterns. The advantage of the developed approach over classic pattern matching techniques is that the patterns are learned from the information inherent to the data. This makes subjective feature handcrafting obsolete and enables a better generalization to other datasets.
In Chapter 3 I developed a tool to generate highly realistic synthetic and therefore fully controllable earthquake swarm data including full waveforms. This allows efficient exploration and benchmarking of new methodologies dedicated to clustered seismicity with comparably little effort. The flexibility of the proposed toolbox makes it applicable to different situations and setups: Earthquakes nucleating along two dimensional rupture planes and with a specific migration pattern as in NW Bohemia or in a more volumetric setting such as hydraulic fracturing experiments where sources are expected to be nucleating in a three-dimensional volume as in the case of Chapter 3. The derived approach allows to generate highly realistic synthetic full waveform records affected by recorded noise. These hybrid traces were used to asses the event detection capabilities in terms of magnitude of completeness M_c for different simulated station configurations. This approach can be used to plan seismological campaigns targeting clustered earthquake analysis more efficiently. Also it allows to assess installed station configurations in the absence of events which can be important information when discussing a reconfiguration or extension of the underlying station setup.
Another key methodological question of this thesis is if it is possible to increase the spatio-temporal resolution of attenuation within the source region and therefore allow a better analysis of the triggering mechanisms of the earthquakes such as uprising magmatic fluids or gases. Synthetic tests of Chapter 4 demonstrate that the developed amplitude spectral ratio method is able to infer source volume attenuation. The method employs high frequencies and therefore allows to map attenuation of the source volume in a highly focused way given a suitable station geometry with respect to the cluster. Synthetic tests also demonstrate that both, compressional (Q_p) and shear wave attenuation (Q_s) can theoretically be estimated, separately. The precision of Q_s estimates is lower than that of Q_p due to the interference with P phase coda. Applications to real data shows that signals undergo significant distortion and are therefore prone to yield unrealistic and non-physical results if the rays from a given event couple take off from the focal sphere close to the nodal plane of the rupturing slab. This effect was dominant in the case of station *NKC*. The second station candidate *LBC* yields stable results for P phase onsets but fails for S phases due to interference with the P phase coda. Therefore, an increase in resolution is only partly achieved. Nevertheless, the results at station *LBC* indicate an attenuation of $Q_p < 100$ in

the focal zone which is relatively decreased given the regional background attenuation of compressional waves ranging between $Q_p = 100$ and $Q_p = 400$.
Differing levels of waveform complexity at station *NKC* and station *LBC* in combination with the geometrical constraints further lead to the conclusion that the medium is likely more fractured in the closest vicinity of the sub-vertical source plane than in the surrounding material. Therefore, it can serve as pathways for magmatic fluids as well or gases which in turn can trigger earthquakes and also contribute to the relatively high attenuation within the source volume.

Chapter 6

Future Work

Software and tools presented in this work are under continuous development and maintenance. The core features of the toolbox described in Chapter 3 are currently being migrated into the scenario generator *Colosseo* of the python seismological framework *pyrocko*. There are some redundant features and migrating to *pyrocko* will make these tools available to a greater community and user base. *Colosseo* is not designed with a specific focus on earthquake swarms and therefore will benefit from the software design of the proposed tools such as the geometrical representations of source volumes and synthetic migration of hypocenters.

Deep learning is a relatively new field in seismology and the full spectrum of applications is still under investigation. The demonstrated proof of concept applied to North West Bohemian earthquake swarm localizations shows that the method is capable to process large amounts of data in unprecedented efficiency. It can therefore enable a much more complete analysis not only of earthquake swarm data. This technique will also foster the analysis of the surging amounts of seismological data being stored in global data centers with higher precision and in a more holistic fashion. Despite the initial success of our method it will have to be modified to become more flexible. Currently, the rigid station ordering prohibits a broad application as the deep neural network has to be retrained for other scenarios. A next step to overcome this issue is to use relative locations of stations with respect to an event over global (normalized) Euclidean locations of earthquakes and receivers. This way of expressing geometrical circumstances would allow to learn the relative locations from which the true absolute locations can be inferred using the correct station location. This approach will need further methodological testing and verification by synthetic and real data. Synthetic testing data can be quickly be generated using the tools described in Chapter 3.

At the time of writing this thesis the international continental drilling project (*ICDP*) drills 4 holes in NW Bohemia and plans to equip these with downhole seismometers (among other research equipment). The expected significant improvement of signal to noise ratio as well as the anticipated higher sampling rates motivate to revisit the proposed amplitude spectral ratio method of event couples as soon as data is available. Extending the spectral evaluation at higher frequencies will allow to fit more data points in the frequency domain which

will reduce the variance of the fitted lines and therefore stabilize the inversion. Furthermore, these recordings will allow to exploit higher and broader frequency ranges than in the presented work of Chapter 4. This is equivalent to decreasing the Fresnel volume which means an even more focused insight into the properties of the seismogenic zone and less influence of the surrounding material.

Combining the deep learning event detection / location approach and the amplitude spectral ratio method applied to event couples will provide a tool chain that enables a fully automated rapid assessment of rock properties. The current implementation requires hand picked phase onsets. This task can be substituded by the deep CNN when training on data segments where the onset locations vary. This requires an additional feature column comprised of phase picks to train the network to predict the position of these picks. A conceptually similar feasibility study was recently presented by Zhu and Beroza (2018). This combined training will require larger computational power than used for the work in Chapter 2. However, the gained flexibility and performance at event location and phase pick prediction will justify mobilizing additional resources.

Bibliography

Abadi, M., Barham, P., Chen, J., Chen, Z., Davis, A., Dean, J., Devin, M., Ghemawat, S., Irving, G., Isard, M., Kudlur, M., Levenberg, J., Monga, R., Moore, S., Murray, D. G., Steiner, B., Tucker, P., Vasudevan, V., Warden, P., Wicke, M., Yu, Y., and Zheng, X. (2016). TensorFlow: A System for Large-scale Machine Learning. In *Proceedings of the 12th USENIX Conference on Operating Systems Design and Implementation*, OSDI'16, pages 265–283, Berkeley, CA, USA. USENIX Association.

Aki, K. (1980). Attenuation of shear-waves in the lithosphere for frequencies from 0.05 to 25 Hz. *Physics of the Earth and Planetary Interiors*, 21(1):50–60.

Aki, K. and Richards, P. G. (2002). *Quantitative seismology*. University Science Books, Sausalito, California, 2 edition.

Alexandrakis, C., Calò, M., Bouchaala, F., and Vavryčuk, V. (2014). Velocity structure and the role of fluids in the West Bohemia Seismic Zone. *Solid Earth Discussions*, 6(1):511–534.

Amorèse, D. (2007). Applying a Change-Point Detection Method on Frequency-Magnitude Distributions. *Bulletin of the Seismological Society of America*, 97(5):1742–1749.

Bachura, M. and Fischer, T. (2016). Coda Attenuation Analysis in the West Bohemia/Vogtland Earthquake Swarm Area. *Pure and Applied Geophysics*, 173(2):425–437.

Baer, M. and Kradolfer, U. (1987). An automatic phase picker for local and teleseismic events. *Bull Seismol Soc Am*, 77(4):1437–1445.

Baig, A. and Urbancic, T. (2010). Microseismic moment tensors: A path to understanding frac growth. *The Leading Edge*, 29(3):320–324.

Baranova, V., Mustaqeem, A., and Bell, S. (1999). A model for induced seismicity caused by hydrocarbon production in the Western Canada Sedimentary Basin. *Canadian Journal of Earth Sciences*, 36:47–64.

BC Oil and Gas Commision (BCOGC) (2012). Investigation of Observed Seismicity in the Horn River Basin : British Columbia Oil and Gas Commission open report.

Becker, T. W. and Boschi, L. (2002). A comparison of tomographic and geodynamic mantle models. *Geochemistry, Geophysics, Geosystems*, 3(1):n/a–n/a.

Bengio, Y., Simard, P., and Frasconi, P. (1994). Learning long-term dependencies with gradient descent is difficult. *IEEE transactions on neural networks*, 5(2):157–166.

Böse, M., Wenzel, F., and Erdik, M. (2008). PreSEIS: A neural network-based approach to earthquake early warning for finite faults. *Bull Seismol Soc Am*, 98(1):366–382.

Bouchaala, F., Vavryčuk, V., and Fischer, T. (2013). Accuracy of the master-event and double-difference locations: Synthetic tests and application to seismicity in West Bohemia, Czech Republic. *Journal of Seismology*, 17(3):841–859.

Bräuer, K., Kämpf, H., Koch, U., and Strauch, G. (2011). Monthly monitoring of gas and isotope compositions in the free gas phase at degassing locations close to the Nový Kostel focal zone in the western Eger Rift¸ Czech Republic. *Chemical Geology*, 290(3-4):163–176.

Bräuer, K., Kämpf, H., Niedermann, S., Strauch, G., and Weise, S. M. (2004). Evidence for a nitrogen flux directly derived from the European subcontinental mantle in the Western Eger Rift, Central Europe. *Geochimica et Cosmochimica Acta*, 68(23):4935–4947.

Bräuer, K., Kämpf, H., and Strauch, G. (2009). Earthquake swarms in non-volcanic regions: What fluids have to say. *Geophysical Research Letters*, 36(17).

Bronstein, M. M., Bruna, J., LeCun, Y., Szlam, A., and Vandergheynst, P. (2016). Geometric deep learning: going beyond Euclidean data. *CoRR*, abs/1611.0.

Cao, A. and Gao, S. S. (2002). Temporal variation of seismic b-values beneath northeastern Japan island arc. *Geophysical Research Letters*, 29(9):43–48.

Cesca, S. and Grigoli, F. (2015). Full Waveform Seismological Advances for Microseismic Monitoring. In *Advances in Geophysics*, chapter 2, pages 169–228.

Cheng, P. and Margrave, G. F. (2009). Q analysis using synthetic viscoacoustic seismic data. *CREWES Research Report*, 21(1):1–11.

Cheng, P. and Margrave, G. F. (2013). Estimation of Q : a comparison of different computational methods. *CSPG/CSEG/CWLS GeoConvention*, 12(May):2–5.

Chun, K.-Y., Henderson, G. A., and Liu, J. (2004). Temporal changes in P wave attenuation in the Loma Prieta rupture zone. *J. Geophys. Res.*, 109(B2):B02317.

Clarke, H., Eisner, L., Styles, P., and Turner, P. (2014). Felt seismicity associated with shale gas hydraulic fracturing: The first documented example in Europe. *Geophysical Research Letters*, 41(23):8308–8314.

Colombi, A., Nissen-Meyer, T., Boschi, L., and Giardini, D. (2014). Seismic waveform inversion for core–mantle boundary topography. *Geophysical Journal International*, 198(1):55–71.

Console, R., Carluccio, R., Papadimitriou, E., and Karakostas, V. (2015). Synthetic earthquake catalogs simulating seismic activity in the Corinth Gulf, Greece, fault system. *Journal of Geophysical Research: Solid Earth*, 120(1):326–343.

Cormier, V. F. (1982). the Effect of Attenuation on Seismic Body Waves. *Bulletin*

of the Seismological Society of America, 72(6):169–200.

Corporation, R. (2008). Bandwidth in Octaves Versus Q in Bandpass Filters. *Library*, pages 3–5.

Dahm, T. and Fischer, T. (2013). Velocity ratio variations in the source region of earthquake swarms in NW Bohemia obtained from arrival time double-differences. *Geophysical Journal International*, 196(2):957–970.

Dahm, T., Fischer, T., and Hainzl, S. (2009). Mechanical intrusion models and their implications for the possibility of magma-driven swarms in NW Bohemia Region. *Studia Geophysica et Geodaetica*, 52(4):529.

Dai, H. and MacBeth, C. (1995). Automatic picking of seismic arrivals in local earthquake data using an artificial neural network. *Geophys J Int*, 120(3):758–774.

Dai, H. and MacBeth, C. (1997). The application of back-propagation neural network to automatic picking seismic arrivals from single-component recordings. *J Geophys Res: Solid Earth*, 102(B7):15105–15113.

D'Alessandro, A., Luzio, D., Mangano, G., and D'Anna, G. (2011a). Seismic Network Evaluation through Simulation: An Application to the Italian National Seismic NetworkSeismic Network Evaluation through Simulation. *Bulletin of the Seismological Society of America*, 101(3):1213–1232.

D'Alessandro, A., Papanastassiou, D., and Baskoutas, I. (2011b). Hellenic Unified Seismological Network: an evaluation of its performance through SNES method. *Geophysical Journal International*, 185(3):1417–1430.

D'Alessandro, A. and Stickney, M. (2012). Montana Seismic Network Performance: An Evaluation through the SNES MethodMontana Seismic Network Performance: An Evaluation through the SNES Method. *Bulletin of the Seismological Society of America*, 102(1):73–87.

Daub, E. G., Trugman, D. T., and Johnson, P. A. (2015). Statistical tests on clustered global earthquake synthetic data sets. *Journal of Geophysical Research: Solid Earth*, 120(8):5693–5716.

Davies, R., Foulger, G., Bindley, A., and Styles, P. (2013). Induced seismicity and hydraulic fracturing for the recovery of hydrocarbons. *Marine and Petroleum Geology*, 45:171–185.

Davies, R. J., Mathias, S. A., Moss, J., Hustoft, S., and Newport, L. (2012). Hydraulic fractures: How far can they go? *Marine and Petroleum Geology*, 37(1):1–6.

Davis, S. and Frohlich, C. (2007). Single-Link Cluster Analysis, Synthetic Earthquake Catalogues, and Aftershock Identification. *Geophysical Journal International*, 104:289–306.

Del Pezzo, E., Esposito, A., Giudicepietro, F., Marinaro, M., Martini, M., and Scarpetta, S. (2003). Discrimination of earthquakes and underwater explosions using neural networks. *Bull Seismol Soc Am*, 93(1):215–223.

Doubravová, J., Wiszniowski, J., and Horálek, J. (2016). Single Layer Recurrent Neural Network for detection of swarm-like earthquakes in W-Bohemia/Vogtland—the method. *Computers & Geosciences*, 93:138–149.

Dowla, F. U., Taylor, S. R., and Anderson, R. W. (1990). Seismic discrimination with artificial neural networks: preliminary results with regional spectral data. *Bull Seismol Soc Am*, 80(5):1346–1373.

Economides, M. J. and Nolte, K. G. (2003). *Reservoir Stimulation*. John Wiley.

Eisner, L., Gei, D., Hallo, M., Opršal, I., and Ali, M. Y. (2013). The peak frequency of direct waves for microseismic events. *GEOPHYSICS*, 78(6):A45–A49.

Ellsworth, W. L. (2013). Injection-Induced Earthquakes. *Science*, 341(6142):1225942.

Farahbod, A. M., Kao, H., Walker, D. M., and Cassidy, J. F. (2015). Investigation of regional seismicity before and after hydraulic fracturing in the Horn River Basin, northeast British Columbia. *Canadian Journal of Earth Sciences*, 52(2):112–122.

Farr, T. G., Rosen, P. A., Caro, E., Crippen, R., Duren, R., Hensley, S., Kobrick, M., Paller, M., Rodriguez, E., Roth, L., Seal, D., Shaffer, S., Shimada, J., Umland, J., Werner, M., Oskin, M., Burbank, D., and Alsdorf, D. (2007). The shuttle radar topography mission. *Rev. Geophys.*, 45(2005):1–33.

Fischer, T. (2003). The August-December 2000 earthquake swarm in NW Bohemia: The first results based on automatic processing of seismograms. *Journal of Geodynamics*, 35(1-2):59–81.

Fischer, T., Horálek, J., Hrubcová, P., Vavryčuk, V., Bräuer, K., and Kämpf, H. (2014). Intra-continental earthquake swarms in West-Bohemia and Vogtland: A review. *Tectonophysics*, 611:1–27.

Fischer, T., Horálek, J., Michálek, J., and Boušková, A. (2010). The 2008 West Bohemia earthquake swarm in the light of the WEBNET network. *Journal of Seismology*, 14(4):665–682.

Fischer, T. and Michálek, J. (2008). Post 2000-swarm microearthquake activity in the principal focal zone of West Bohemia/Vogtland: Space-time distribution and waveform similarity analysis. *Studia Geophysica et Geodaetica*, 52(4):493–511.

Fisher, M. K. and Warpinski, N. R. (2012). Hydraulic-Fracture-Height Growth: Real Data. *SPE Production & Operations*, 27(01):8–19.

Gaebler, P. J., Eulenfeld, T., and Wegler, U. (2015). Seismic scattering and absorption parameters in the W-Bohemia/Vogtland region from elastic and acoustic radiative transfer theory. *Geophysical Journal International*, 203(3):1471–1481.

Gaite, B., Ugalde, A., Villaseñor, A., and Blanch, E. (2016). Improving the location of induced earthquakes associated with an underground gas storage in the Gulf of Valencia (Spain). *Physics of the Earth and Planetary Interiors*, 254:46–59.

Gajewski, D. and Tessmer, E. (2005). Reverse modelling for seismic event characterization. *Geophysical Journal International*, 163(1):276–284.

Geiger, L. (1910). *Herdbestimmung bei Erdbeben aus den Ankunftszeiten.* [publisher not identified], [Place of publication not identified].

Gentili, S. and Michelini, A. (2006). Automatic picking of P and S phases using a neural tree. *Journal of Seismology*, 10(1):39–63.

Gibbons, S. J. and Ringdal, F. (2006). The detection of low magnitude seismic events using array-based waveform correlation. *Geophysical Journal International*, 165(1):149–166.

Gomberg, J. (1991). Seismicity and detection/location threshold in the southern Great Basin seismic network. *Journal of Geophysical Research*, 96(B10).

Goodfellow, I., Bengio, Y., and Courville, A. (2016). *Deep Learning*. MIT Press.

Got, J.-L., Fréchet, J., and Klein, F. W. (1994). Deep fault plane geometry inferred from multiplet relative relocation beneath the south flank of Kilauea. *Journal of Geophysical Research: Solid Earth*, 99(B8):15375–15386.

Grabowska, T., Bojdys, G., and Dolnicki, J. (1998). Three-dimensional density model of the Earth's crust and the upper mantle for the area of Poland. *Journal of Geodynamics*, 25(1-2):5–34.

Grad, M., Polkowski, M., and Ostaficzuk, S. R. (2016). High-resolution 3D seismic model of the crustal and uppermost mantle structure in Poland. *Tectonophysics*, 666:188–210.

Grigoli, F., Cesca, S., Krieger, L., Kriegerowski, M., Gammaldi, S., Horalek, J., Priolo, E., and Dahm, T. (2016). Automated microseismic event location using Master-Event Waveform Stacking. *Scientific Reports*, 6:25744.

Grigoli, F., Cesca, S., Vassallo, M., and Dahm, T. (2013). Automated seismic event location by travel-time stacking: An application to mining induced seismicity. *Seismol Res Lett*, 84(4):666–677.

Grigoli, F., Scarabello, L., Böse, M., Weber, B., Wiemer, S., and Clinton, J. F. (2018). Pick- and waveform-based techniques for real-time detection of induced seismicity. *Geophysical Journal International*, 213(2):868–884.

Group, J. R., Dresen, G., Kwiatek, G., and Plenkers, K. (2011a). Source Parameters of Picoseismicity Recorded at Mponeng Deep Gold Mine, South Africa: Implications for Scaling RelationsSource Parameters of Picoseismicity at Mponeng Mine, South Africa: Implications for Scaling Relations. *Bulletin of the Seismological Society of America*, 101(6):2592–2608.

Group, J. R., Plenkers, K., Schorlemmer, D., and Kwiatek, G. (2011b). On the Probability of Detecting PicoseismicityOn the Probability of Detecting Picoseismicity. *Bulletin of the Seismological Society of America*, 101(6):2579–2591.

Haberland, C. and Rietbrock, A. (2001). Attenuation tomography in the western central Andes: A detailed insight into the structure of a magmatic arc. *Journal of Geophysical Research*, 106(B6):11151.

Häge, M. and Joswig, M. (2009). Spatiotemporal characterization of interswarm period seismicity in the focal area Nový Kostel (West Bohemia/Vogtland) by a short-term microseismic study. *Geophysical Journal International*, 179(2):1071–1079.

Hainzl, S., Fischer, T., and Dahm, T. (2012). Seismicity-based estimation of the driving fluid pressure in the case of swarm activity in Western Bohemia.

Geophysical Journal International, 191(1):271–281.

Havskov, J., Bormann, P., and Schweitzer, J. (2012). Information Sheet IS 11.1: Seismic source location. Version 2. *In: Bormann, P. (Ed.) (2012). New Manual of Seismological Observatory Practice (NMSOP-2), IASPEI, GFZ German Research Centre for Geosciences, Potsdam.*

Healy, J. H., Rubey, W. W., Griggs, D. T., and Raleigh, C. B. (1968). The Denver EarthquakeS. *Science*, 161(3848):1301 LP – 1310.

Heidbach, O., Tingay, M., Barth, A., Reinecker, J., Kurfeß, D., and Müller, B. (2009). The World Stress Map Based on the Database Release 2008.

Heimann, S. (2011). *A Robust Method To Estimate Kinematic Earthquake Source Parameters*. Dissertation, University of Hamburg.

Heimann, S. (2012). Fomosto - forward model storage tool. http://emolch.github.io/pyrocko/current/fomosto.html.

Heimann, S., Cesca, S., Dahm, T., González, Á., Grigoli, F., Maghsoudi, S., Buforn, E., and Blanch, E. (2014a). The 2013 September–October seismic sequence offshore Spain: a case of seismicity triggered by gas injection? *Geophysical Journal International*, 198(2):941–953.

Heimann, S., Cesca, S., Kriegerowski, M., and Dahm, T. (2014b). Synthetic seismogram web service and Python tools. In *EGU General Assembly Conference Abstracts*, volume 16, page 10466.

Heimann, S., Kriegerowski, M., Isken, M., Cesca, S., Daout, S., Grigoli, F., Juretzek, C., Megies, T., Nooshiri, N., Steinberg, A., Sudhaus, H., Vasyura-Bathke, H., Willey, T., and Dahm, T. (2017). Pyrocko - An open-source seismology toolbox and library.

Heimann, S., Vasyura-Bathke, H., Sudhaus, H., Isken, M. P., Kriegerowski, M., Steinberg, A., and Dahm, T. (2019). A Python framework for efficient use of pre-computed Green's functions in seismological and other physical forward and inverse source problems. *Solid Earth Discussions*, pages 1–22.

Heinicke, J., Fischer, T., Gaupp, R., Götze, J., Koch, U., Konietzky, H., and Stanek, K.-P. (2009). Hydrothermal alteration as a trigger mechanism for earthquake swarms: the Vogtland/NW Bohemia region as a case study. *Geophysical Journal International*, 178(1):1–13.

Hiemer, S., Roessler, D., and Scherbaum, F. (2012). Monitoring the West Bohemian earthquake swarm in 2008/2009 by a temporary small-aperture seismic array. *Journal of Seismology*, 16(2):169–182.

Holland, A. A. (2013). Earthquakes Triggered by Hydraulic Fracturing in South-Central OklahomaEarthquakes Triggered by Hydraulic Fracturing in South-Central Oklahoma. *Bulletin of the Seismological Society of America*, 103(3):1784–1792.

Horálek, J. and Fischer, T. (2008). Role of crustal fluids in triggering the West Bohemia/Vogtland earthquake swarms: Just what we know (a review). *Studia Geophysica et Geodaetica*, 52(4):455–478.

Horálek, J., Fischer, T., Boušková, A., and Jedlička, P. (2000a). The Western Bohemia/Vogtland Region in the Light of the Webnet Network. *Studia*

Geophysica et Geodaetica, 44(2):107–125.

Horálek, J., Fischer, T., Bouškova, A., Michálek, J., and Hrubcová, P. (2009). The West Bohemian 2008-earthquake swarm: When, where, what size and data. *Studia Geophysica et Geodaetica*, 53(3):351–358.

Horálek, J., Šílený, J., Fischer, T., Slancová, A., and Bouškova, A. (2000b). Scenario of the January 1997 West Bohemia earthquake swarm. *Studia Geophysica et Geodaetica*, 44(4):491–521.

Horálek, J., Šílený, J., Fischer, T., Slancová, A., Bouškova, A., Š\'ilený, J., Fischer, T., Slancová, A., and Bouškova, A. (2000c). Scenario of the January 1997 West Bohemia Earthquake Swarm. *Stud. Geophys. Geod.*, 44(January 1997):491–521.

Horner, R., Barclay, J., and MacRae, J. (1994). Earthquakes and Hydrocarbon Production Near Fort St. John, B.C. *Canadian Journal of Exploration Geophysics*, 19(3).

Hudson, J. A., Pearce, R. G., and Rogers, R. M. (1989). Source type plot for inversion of the moment tensor. *Journal of Geophysical Research: Solid Earth*, 94(B1):765–774.

Institute of Geophysics, Academy of Sciences of the Czech Republic (1991). West Bohemia Local Seismic Network. International Federation of Digital Seismograph Networks. Other/Seismic Network.

Ito, A. (1985). HIGH RESOLUTION RELATIVE HYPOCENTERS OF SIMILAR EARTHQUAKES BY CROSS-SPECTRAL ANALYSIS METHOD. *Journal of Physics of the Earth*, 33(4):279–294.

Jakoubková, H., Horálek, J., and Fischer, T. (2018). 2014 Mainshock-Aftershock Activity Versus Earthquake Swarms in West Bohemia, Czech Republic. *Pure and Applied Geophysics*, 175(1):109–131.

Joswig, M. (1990). Pattern recognition for earthquake detection. *Bulletin of the Seismological Society of America*, 80(1):170–186.

Joswig, M. (1994). Knowledge-based seismogram processing by mental images. *IEEE TRANSACTIONS ON SYSTEMS, MAN, AND CYBERNETICS*, 24(3):429–439.

Kaneko, Y. and Shearer, P. M. (2015). Variability of seismic source spectra, estimated stress drop, and radiated energy, derived from cohesive-zone models of symmetrical and asymmetrical circular and elliptical ruptures. *Journal of Geophysical Research: Solid Earth*, 120(2):1053–1079.

Kennett, B. L. N. and Gudmundsson, O. (1996). Ellipticity corrections for seismic phases. *Geophysical Journal International*, 127(1):40–48.

Keranen, K. M., Abers, G. A., Savage, H. M., and Cochran, E. S. (2013). Potentially induced earthquakes in Oklahoma, USA: Links between wastewater injection and the 2011 Mw 5.7 earthquake sequence. *Geology*, 41(6):699–702.

Keskar, N. S., Mudigere, D., Nocedal, J., Smelyanskiy, M., and Tang, P. T. P. (2016). On large-batch training for deep learning: Generalization gap and sharp minima. *arXiv preprint arXiv:1609.04836*.

Kingma, D. P. and Ba, J. (2014). Adam: A method for stochastic optimization.

arXiv preprint arXiv:1412.6980.

Ko, Y.-T., Kuo, B.-Y., and Hung, S.-H. (2012). Robust determination of earthquake source parameters and mantle attenuation. *Journal of Geophysical Research: Solid Earth*, 117(B4).

Koch, U. and Heinicke, J. (2011). Seismohydrological effects related to the NW Bohemia earthquake swarms of 2000 and 2008: Similarities and distinctions. *Journal of Geodynamics*, 51(1):44–52.

Köhler, A., Ohrnberger, M., and Scherbaum, F. (2010). Unsupervised pattern recognition in continuous seismic wavefield records using Self-Organizing Maps. *Geophys J Int*, 182(3):1619–1630.

Kriegerowski, M., Cesca, S., Krüger, F., and Dahm, T. (2015). Approaching moment tensor inversion and Q factor tomography of Western Bohemia earthquake swarms. In *IUGG, Prague, Czech Republic (Conference Poster)*, Prague.

Kriegerowski, M., Cesca, S., Ohrnberger, M., Dahm, T., and Krüger, F. (2019). Event couple spectral ratio Q method for earthquake clusters: application to northwest Bohemia. *Solid Earth*, 10(1):317–328.

Kriegerowski, M., Petersen, G. M., Vasyura-Bathke, H., and Ohrnberger, M. (2018). A Deep Convolutional Neural Network for Localization of Clustered Earthquakes Based on Multistation Full Waveforms. *Seismological Research Letters*, 90(2A):510–516.

Krischer, L. (2016). mtspec Python wrappers 0.3.2.

Król, M., Cichostępski, K., Dec, J., and Pietsch, K. (2013). Application of inverse Q filtering for improvement of seismic resolution in the Zechstein formation (SW Poland). *Geology, Geophysics and Environment*, 39(1):33.

Kværna, T., Ringdal, F., Schweitzer, J., and Taylor, L. (2002). Optimized Seismic Threshold Monitoring – Part 1: Regional Processing. *pure and applied geophysics*, 159(5):969–987.

Lathuilière, S., Mesejo, P., Alameda-Pineda, X., and Horaud, R. (2018). A Comprehensive Analysis of Deep Regression.

Lawrence, J. F., Shearer, P. M., and Masters, G. (2006). Mapping attenuation beneath North America using waveform cross-correlation and cluster analysis. *Geophysical Research Letters*, 33(7):2–5.

LeCun, Y., Bengio, Y., and Hinton, G. (2015). Deep learning. *nature*, 521(7553):436.

Li, X.-P. and Richwalski, S. (1996). Seismic attenuation and velocities of P- and S-waves in the German KTB area. *Journal of Applied Geophysics*, 36(2-3):67–76.

Lienert, B. R., Berg, E., and Frazer, L. N. (1986). Hypocenter: an Earthquake Location Method Using Centered, Scaled, and Adaptively Damped Least Squares. *Bulletin of the Seismological Society of America*, 76(3):771–783.

López-Comino, J., Cesca, S., Kriegerowski, M., Heimann, S., Dahm, T., Mirek, J., and Lasocki, S. (2017a). Monitoring performance using synthetic data for induced microseismicity by hydrofracking at the Wysin site (Poland). *Geo-*

physical Journal International, 210:42–55.

López-Comino, J. A., Cesca, S., Heimann, S., Grigoli, F., Milkereit, C., Dahm, T., and Zang, A. (2017b). Characterization of Hydraulic Fractures Growth During the Äspö Hard Rock Laboratory Experiment (Sweden). *Rock Mechanics and Rock Engineering*, 50(11):2985–3001.

Madariaga, R. (1976). Dynamics of an expanding circular fault. *Bulletin of the Seismological Society of America*, 66(3):639–666.

Maghsoudi, S., Cesca, S., Hainzl, S., Dahm, T., Kaiser, D., and Becker, D. (2013). Improving the estimation of detection probability and magnitude of completeness in strongly heterogeneous media, an application to acoustic emission (AE). *Geophysical Journal International*, 193(3):1556–1569.

Maghsoudi, S., Hainzl, S., Cesca, S., Dahm, T., Zöller, G., and Kaiser, D. (2015). Maximum Magnitude of Completeness in a Salt MineMaximum Magnitude of Completeness in a Salt Mine. *Bulletin of the Seismological Society of America*, 105(3):1491–1501.

Málek, J., Janský, J., and Horálek, J. (2000). Layered Velocity Models of the Western Bohemia Region. *Studia Geophysica et Geodaetica*, 44(4):475–490.

Marsan, D. (2003). Triggering of seismicity at short timescales following Californian earthquakes. *Journal of Geophysical Research: Solid Earth*, 108(B5).

Masson, Y., Cupillard, P., Capdeville, Y., and Romanowicz, B. (2014). On the numerical implementation of time-reversal mirrors for tomographic imaging. *Geophysical Journal International*, 196(3):1580–1599.

Matos, C., Heimann, S., Grigoli, F., Cesca, S., and Custódio, S. (2016). Seismicity of a slow deforming environment: Alentejo, south Portugal. In *EGU General Assembly Conference Abstracts*, volume 18 of *EGU General Assembly Conference Abstracts*, pages EPSC2016–278.

Matsumoto, S., Uehira, K., Watanabe, A., Goto, K., Iio, Y., Hirata, N., Okada, T., Takahashi, H., Shimizu, H., Shinohara, M., and Kanazawa, T. (2009). High resolution Q-1 estimation based on extension of coda normalization method and its application to P-wave attenuation structure in the aftershock area of the 2005 West Off Fukuoka Prefecture Earthquake (M7.0). *Geophysical Journal International*, 179(2):1039–1054.

McGarr, A. F., Simpson, D., and Seeber, L. (2002). Case histories of induced and triggered seismicity: Chapter 40. In Lee, W. H. K., Kanamori, H., Jennings, P. C., and Kisslinger, C., editors, *International Handbook of Earthquake and Engineering Seismology, Part A*, volume 81, pages 647–661. Elsevier.

McMechan, G. A. (1982). Determination of source parameters by wavefield extrapolation. *Geophysical Journal of the Royal Astronomical Society*, 71(3):613–628.

Michálek, J. and Fischer, T. (2013). Source parameters of the swarm earthquakes in West Bohemia/Vogtland. *Geophysical Journal International*, 195(2):1196–1210.

Mignan, A. and Chouliaras, G. (2014). Fifty Years of Seismic Network Performance in Greece (1964–2013): Spatiotemporal Evolution of the Completeness

Magnitude. *Seismological Research Letters*, 85(3):657–667.

Mignan, A., Kraft, T., and Giardini, D. (2013). Optimization of a large-scale microseismic monitoring network in northern Switzerland. *Geophysical Journal International*, 195(1):474–490.

Mignan, A., Werner, M. J., Wiemer, S., Chen, C.-C., and Wu, Y.-M. (2011). Bayesian Estimation of the Spatially Varying Completeness Magnitude of Earthquake CatalogsBayesian Estimation of the Spatially Varying Completeness Magnitude of Earthquake Catalogs. *Bulletin of the Seismological Society of America*, 101(3):1371–1385.

Mignan, A. and Woessner, J. (2012). Estimating the magnitude of completeness for earthquake catalogs. *Community Online Resource for Statistical Seismicity Analysis*.

Minar, M. R. and Naher, J. (2018). Recent Advances in Deep Learning: An Overview.

Monteiller, V., Chevrot, S., Komatitsch, D., and Fuji, N. (2013). A hybrid method to compute short-period synthetic seismograms of teleseismic body waves in a 3-D regional model. *Geophysical Journal International*, 192(1):230–247.

Mousavi, S., Haberland, C., Bauer, K., Hejrani, B., and Korn, M. (2017). Attenuation tomography in West Bohemia/Vogtland. *Tectonophysics*, 695:64–75.

Murat, M. E. and Rudman, A. J. (1992). AUTOMATED FIRST ARRIVAL PICKING: A NEURAL NETWORK APPROACH 1. *Geophysical Prospecting*, 40(6):587–604.

Musil, M. and Plešinger, A. (1996). Discrimination between local microearthquakes and quarry blasts by multi-layer perceptrons and Kohonen maps. *Bull Seismol Soc Am*, 86(4):1077–1090.

Nanjo, K. Z., Giardini, D., Woessner, J., Wiemer, S., and Schorlemmer, D. (2010). Earthquake detection capability of the Swiss Seismic Network. *Geophysical Journal International*, 181(3):1713–1724.

Nicholson, C. and Wesson, R. L. (1990). Earthquake hazard associated with deep well injection: a report to the U.S. Environmental Protection Agency. Technical report, Washington, D.C.

Nicholson, C. and Wesson, R. L. (1992). Triggered earthquakes and deep well activities. *pure and applied geophysics*, 139(3):561–578.

Nissen-Meyer, T., Van Driel, M., Stähler, S. C., Hosseini, K., Hempel, S., Auer, L., Colombi, A., and Fournier, A. (2014). AxiSEM: Broadband 3-D seismic wavefields in axisymmetric media. *Solid Earth*, 5(1):425–445.

Nolen-Hoeksema, R. C. and Ruff, L. J. (2001). Moment tensor inversion of microseisms from the B-sand propped hydrofracture, M-site, Colorado. *Tectonophysics*, 336(1-4):163–181.

Park, J., Craig, R. L., and Vernon III, F. L. (1987). Multitaper spectral analysis of high-frequency seismograms. *J. Geophys. Res.*, 92(B12):12675–12684.

Pascanu, R., Mikolov, T., and Bengio, Y. (2012). Understanding the exploding gradient problem. *CoRR, abs/1211.5063*.

Perol, T., Gharbi, M., and Denolle, M. (2018). Convolutional neural network for earthquake detection and location. *Science Advances*, 4(2):e1700578.

Prieto, G., Parker, R., and Vernon III, F. (2009). A Fortran 90 library for multitaper spectrum analysis. *Computers & Geosciences*, 35(8):1701–1710.

Ringdal, F. and Kværna, T. (1999). Seismic threshold monitoring for continuous assessment of global detection capability. *Bulletin of the Seismological Society of America*, 89(4):946–959.

Rosenblatt, F. (1958). The perceptron: a probabilistic model for information storage and organization in the brain. *Psychological review*, 65(6):386.

Ross, Z. E., Meier, M.-A., and Hauksson, E. (2018a). P-wave arrival picking and first-motion polarity determination with deep learning. *J Geophys Res: Solid Earth*.

Ross, Z. E., Meier, M.-A., Hauksson, E., and Heaton, T. H. (2018b). Generalized Seismic Phase Detection with Deep Learning. *arXiv preprint arXiv:1805.01075*.

Rost, S. and Thomas, C. (2002). Array seismology: Methods and applications. *Reviews of Geophysics*, 40(3):1008.

Rost, S. and Thomas, C. (2009). Improving Seismic Resolution Through Array Processing Techniques. *Surveys in Geophysics*, 30(4):271–299.

Röth, G. and Tarantola, A. (1994). Neural networks and inversion of seismic data. *J Geophys Res: Solid Earth*, 99(B4):6753–6768.

Růzek, B. and Horálek, J. (2013). Three-dimensional seismic velocity model of the west Bohemia/Vogtland seismoactive region. *Geophysical Journal International*, 195(2):1251–1266.

Rydelek, P. A. and Sacks, I. S. (1989). Testing the completeness of earthquake catalogues and the hypothesis of self-similarity. *Nature*, 337(6204):251–253.

Sanders, C. O. (1993). Local earthquake tomography: attenuation—theory and results. *Seismic Tomography: Theory and Practice*, pages 676–694.

Scherbaum, F., Krüger, F., and Weber, M. (1997). Double beam imaging: Mapping lower mantle heterogeneities using combinations of source and receiver arrays. *Journal of Geophysical Research: Solid Earth*, 102(B1):507–522.

Schorlemmer, D. and Woessner, J. (2008). Probability of Detecting an EarthquakeProbability of Detecting an Earthquake. *Bulletin of the Seismological Society of America*, 98(5):2103–2117.

Schultz, R., Stern, V., and Gu, Y. J. (2014). An investigation of seismicity clustered near the Cordel Field, west central Alberta, and its relation to a nearby disposal well. *Journal of Geophysical Research: Solid Earth*, 119(4):3410–3423.

Schultz, R., Stern, V., Gu, Y. J., and Eaton, D. (2015a). Detection Threshold and Location Resolution of the Alberta Geological Survey Earthquake Catalogue. *Seismological Research Letters*, 86(2A):385–397.

Schultz, R., Stern, V., Novakovic, M., Atkinson, G., and Gu, Y. J. (2015b). Hydraulic fracturing and the Crooked Lake Sequences: Insights gleaned from regional seismic networks. *Geophysical Research Letters*, 42(8):2750–2758.

Schurr, B., Asch, G., Rietbrock, A., Trumbull, R., and Haberland, C. (2003).

Complex patterns of fluid and melt transport in the central Andean subduction zone revealed by attenuation tomography. *Earth and Planetary Science Letters*, 215(1-2):105–119.

Sereno Jr., T. J. and Bratt, S. R. (1989). Seismic detection capability at NORESS and implications for the detection threshold of a hypothetical network in the Soviet Union. *Journal of Geophysical Research: Solid Earth*, 94(B8):10397–10414.

Sermanet, P., Eigen, D., Zhang, X., Mathieu, M., Fergus, R., and LeCun, Y. (2013). Overfeat: Integrated recognition, localization and detection using convolutional networks. *arXiv preprint arXiv:1312.6229*.

Sharma, B. K., Kumar, A., and Murthy, V. M. (2010). Evaluation of seismic events detection algorithms. *Journal of the Geological Society of India*, 75(3):533–538.

Slunga, R., Bödvarsson, R., and Rögnvaldsson, S. T. (1995). Absolute and relative locations of similar events with application to microearthquakes in southern Iceland. *Geophysical Journal International*, 123(2):409–419.

Springenberg, J. T., Dosovitskiy, A., Brox, T., and Riedmiller, M. (2014). Striving for simplicity: The all convolutional net. *arXiv preprint arXiv:1412.6806*.

Spudich, P. and Bostwick, T. (1987). Studies of the seismic coda using an earthquake cluster as a deeply buried seismograph array. *Journal of Geophysical Research: Solid Earth*, 92(B10):10526–10546.

Srivastava, N., Hinton, G., Krizhevsky, A., Sutskever, I., and Salakhutdinov, R. (2014). Dropout: a simple way to prevent neural networks from overfitting. *The Journal of Machine Learning Research*, 15(1):1929–1958.

Stähler, S. C. and Sigloch, K. (2013). Fully probabilistic seismic source inversion – Part 1: Efficient parameterisation. *Solid Earth Discussions*, 5(2):1125–1162.

Stähler, S. C., Sigloch, K., and Nissen-Meyer, T. (2012). Triplicated P-wave measurements for waveform tomography of the mantle transition zone. *Solid Earth*, 3(2):339–354.

Stevens, J. L., Xu, H., and Baker, G. E. (2003). 28th Seismic Research Review : Ground-Based Nuclear Explosion Monitoring Technologies 28th Seismic Research Review : Ground-Based Nuclear Explosion Monitoring Technologies. *(Clvd)*, pages 693–703.

Thomson, D. J. (1982). Spectrum estimation and harmonic analysis. *Proceedings of the IEEE*, 70(9):1055–1096.

Tiira, T. (1999). Detecting teleseismic events using artificial neural networks. *Computers & Geosciences*, 25(8):929–938.

Toksöz, M. N., Johnston, D. H., and of Exploration Geophysicists, S. (1981). *Seismic wave attenuation*. Geophysics reprint series. Society of Exploration Geophysicists.

Vavryčuk, V. (2011). Principal earthquakes: Theory and observations from the 2008 West Bohemia swarm. *Earth and Planetary Science Letters*, 305(3):290–296.

Vavryčuk, V., Bouchaala, F., and Fischer, T. (2013). High-resolution fault image from accurate locations and focal mechanisms of the 2008 swarm earthquakes in West Bohemia, Czech Republic. *Tectonophysics*, 590:189–195.

Velasco, A. A. and Zeiler, C. (2009). Seismogram Picking Error from Analyst Review (SPEAR): Single-Analyst and Institution AnalysisSeismogram Picking Error from Analyst Review (SPEAR): Single-Analyst and Institution Analysis. *Bulletin of the Seismological Society of America*, 99(5):2759–2770.

Waldhauser, F. and Ellsworth, W. L. (2000). A Double-difference Earthquake location algorithm: Method and application to the Northern Hayward Fault, California. *Bulletin of the Seismological Society of America*, 90(6):1353–1368.

Wang, J. and Teng, T.-L. (1995). Artificial neural network-based seismic detector. *Bull Seismol Soc Am*, 85(1):308–319.

Wang, J. and Teng, T.-l. (1997). Identification and picking of S phase using an artificial neural network. *Bull Seismol Soc Am*, 87(5):1140–1149.

Wang, L.-X. (1992). A neural detector for seismic reflectivity sequences. *IEEE transactions on neural networks*, 3(2):338–340.

Wang, R. (1999). A simple orthonormalization method for stable and efficient computation of Green's functions. *Bulletin of the Seismological Society of America*, 89(3):733–741.

Wcisło, M., Eisner, L., Málek, J., Fischer, T., Vlček, J., and Kletetschka, G. (2018). Attenuation in west bohemia: Evidence of high attenuation in the Nový Kostel focal zone and temporal change consistent with Co2degassing. *Bulletin of the Seismological Society of America*.

Wessel, P., Smith, W. H. F., Scharroo, R., Luis, J. F., and Wobbe, F. (2013). Generic Mapping Tools: Improved version released. *EOS Trans. AGU*, 94:409–410.

Wiemer, S. and Wyss, M. (2000). Minimum Magnitude of Completeness in Earthquake Catalogs: Examples from Alaska, the Western United States, and Japan. *Bulletin of the Seismological Society of America*, 90(4):859–869.

Wulff, A.-M. and Burkhardt, H. (1997). Dependence of seismic wave attenuations and velocities in rock on pore fluid properties. *Physics and Chemistry of the Earth*, 22(1-2):69–73.

Yoon, C. E., O'Reilly, O., Bergen, K. J., and Beroza, G. C. (2015). Earthquake detection through computationally efficient similarity search. *Science Advances*, 1(11):e1501057.

Zang, A. and Stephansson, O. (2010). *Stress field of the Earth's Crust*.

Zhang, X., Zhang, J., Yuan, C., Liu, S., Chen, Z., and Li, W. (2018). Locating earthquakes with a network of seismic stations via a deep learning method.

Zhao, Y. and Takano, K. (1999). An artificial neural network approach for broadband seismic phase picking. *Bull Seismol Soc Am*, 89(3):670–680.

Zhu, W. and Beroza, G. C. (2018). PhaseNet: A Deep-Neural-Network-Based Seismic Arrival Time Picking Method. *Geophysical Journal International*, 216(1):261–273.

Acknowledgements

First of all I would like to thank my supervisors Frank Krüger and Simone Cesca for their support, guidance and fruitful discussions.
I further want to thank all of my colleagues and friends who guided me through these last few years by providing help, feedback and sharing their experience and knowledge: Torsten Dahm, Matthias Ohrnberger, Sebastian Heimann, Marius Paul Isken, Frank Scherbaum, Sebastian Stober, Nima, Djamil, Peter, Gesa, Toño, Sreeram, Jose. I would like to thank Tomas Fischer and Josef Horalek for providing the data upon which this thesis is based.
Further, I would like to thank the DFG for providing the funding of my thesis.

Ich möchte die Gelegenheit nutzen und an dieser Stelle insbesondere denjenigen Danken, die mir die Möglichkeit gegeben haben alles zu tun was mich erfüllt: Meinen Eltern und meiner Schwester. Auch danke ich Susanne, dass sie mich in allen Lagen unterstützt hat.